TECHNISCHE UNIVERSITÄT MÜNCHEN

Fakultät Wissenschaftszentrum Weihenstephan für Ernährung, Landnutzung und Umwelt
Lehrstuhl für Experimentelle Genetik

Physiology and molecular characterization of metabolism related mouse models for bone disease

Shen Chi

Vollständiger Abdruck der von der Fakultät Wissenschaftszentrum Weihenstephan für Ernährung, Landnutzung und Umwelt der Technischen Universität München zur Erlangung des akademischen Grades eines

Doktors der Naturwissenschaften

genehmigten Dissertation.

Vorsitzender: Univ.-Prof. Dr. W. Wurst
Prüfer der Dissertation:
1. Univ.-Prof. Dr. M. Hrabé de Angelis
2. apl. Prof. Dr. J. Adamski

Die Dissertation wurde am 16.03.2015 bei der Technischen Universität München eingereicht und durch die Fakultät Wissenschaftszentrum Weihenstephan für Ernährung, Landnutzung und Umwelt am 29.07.2015 angenommen.

I. Table of contents

II. Figures and tables

III. Abbreviations

µCT	Micro computed tomography
A	Alanine
AI	Amelogenesis imperfecta
ALP	Alkaline phosphatase
ANOVA	Analysis of variance
ATP	Adenosine tri phosphate
AUC	Areas under the curve
BAT	Brown adipose tissues
BMC	Bone mineral content
BMD	Bone mineral density
BMP	Bone morphogenetic protein
BMU	Bone multicellular units
cDNA	Complementary deoxyribonucleic acid
CNS	Central nervous system
CO_2	Carbon dioxide
Cp	Cross point
cRNA	Complementary ribonucleic acid
CT	Computed tomography
CTX-1	C-telopeptide of type I collagen
DANN	Deoxyribonucleic acid
ddH_2O	Double-distilled water
DEXA	Dual-energy X-ray absorptiometry
DHEA	Dehydroepiandrosterone
DICD	DLL1 intracellular domain
DLL1	Delta-like 1

dNTP	Dinucleotide triphosphate
DTT	Dithiothreitol
e.g.	For example (exempli gratia)
ECM	Extracellular matrix
EDTA	Ethylene diamine tetraacetic acid
ELISA	Enzyme-linked immunosorbant assay
ENU	*N*-ethyl-*N*-nitrosourea
EtOH	Ethanol
eWAT	Epididymal white adipose tissues
FDR	False discovery rate
FFA	Free fatty acid
Gb	Gigabyte
GMC	German Mouse Clinic
GO	Gene ontology
GOT	Glutamic oxaloacetic transaminase
GPT	Glutamic pyruvic transaminase
H&E	Hematoxylin and Eosin
HCTC	Hematocrit
HGB	Hemoglobin
HKG	Housekeeping gene
HP	Heat production
IC	Indirect calorimetric
ipGTT	Intraperitoneal glucose tolerance test
L	Leucine
MAPK	Mitogen-activated protein kinase
MAR	Matrix attachment regions

MCH	Mean corpuscular hemoglobin
MCHC	Mean corpuscular hemoglobin concentrations
MCV	Mean corpuscular volume
MEP	Munich ENU mutagenesis project
MPV	Mean platelet volume
MSC	Mesenchymal stem cells
NGS	Next generation sequencing
NMR	Nuclear magnetic resonance
O_2	Oxygen
OC	Osteocalcin
PAGE	Polyacrylamide gel electrophoresis
PBS	Phosphate buffered saline
PBST	Phosphate buffered saline with 0.05% Tween-20
PCA	Principal component analysis
PCR	Polymerase chain reaction
PLT	Platelet
pQCT	Peripheral quantitative computed tomography
PTH	Parathyroid hormone
PVDF	Polyvinylidene fluoride
qRT-PCR	Quantitative real-time PCR
RANKL	Receptor activator of nuclear factor kappa-B ligand
RBC	Red blood cell
RDW	Red blood cell distribution width
RER	Respiratory exchange ratio
RIN	RNA integrity number

RIPA	Radioimmunoprecipitation assay buffer
RM	Room temperature
RNA	Ribonucleic acid
Satb2	Special AT-rich sequence-binding protein 2
SD	Standard deviations
SDS	Sodium dodecyl sulfate
SEM	Standard error of the mean
SNV	Single nucleotide variants
SPF	Specific-pathogen-free
SUMO	Small ubiquitin-related modifier
T	Threonine
T4	Thyroxine
TEMED	N,N,N',N'-tetramethylethylenediamine
TMB	3,3',5,5'-Tetramethylbenzidine
TRAP	Tartrate-resistant acidic phosphatase
V	Valine
WAT	White adipose tissues
WBC	White blood cell

1. Summary/Zusammenfassung

As an important part of the vertebrate endoskeleton, bone consistently remodels itself to maintain mineral homeostasis and physiological function. Bone homeostasis can be influenced by the imbalance between resorption and formation. Disorders of bone are commonly associated with various metabolic diseases such as obesity, diabetes and cardiovascular disease. In this study, two mutant mouse lines were analyzed to discover the underlying patho-mechanisms leading to abnormal metabolic phenotypes.

According to the German Mouse Clinic (GMC) primary screen, two ENU-induced mutant mouse lines (BAP002, Dll1T720A) exhibited pronounced bone alterations and abnormal metabolic parameters. In this thesis, the two mouse lines were further analyzed to confirm and explore the relationship between bone and metabolic phenotypes.

The dominant BAP002 mouse line derived from an phenotypic ENU-mutagenesis screen for new mouse models of impaired bone metabolism (*OSTEOPATH* project). A dominant point mutation in the *Satb2* gene on chromosome 1 was identified as causative. Heterozygous mice displayed high total ALP blood activities, abnormal tooth enamel and a dysgnathia phenotype. Apart from confirming already known bone phenotypes, bone cells, adipocytes as well as energy expenditure were investigated in an *in vivo* murine context. *Satb2*$^{V234L/+}$ mice showed bone turnover abnormality, characterized by imbalanced osteoblast and osteoclast numbers. In addition, activated beige adipocytes in *Satb2*$^{V234L/+}$ mice may lead to reduced white adiposity and increased insulin sensitivity. Therefore, the results presented in this thesis demonstrate that SATB2 not only regulates bone development, but also plays a novel role in energy metabolism.

The mouse line Dll1T720 originally derived from screening the in-house F1 DNA archive for new mutations of the *Dll1*. Homozygous *Dll1*$^{T720A/-}$ mice, which were analyzed in the primary screen of the German Mouse Clinic, expressed alterations in body weight, body size, body composition and several bone parameters when compared to C3HeB/FeJ wild-type mice. However, only transient differences were observed between *Dll1*$^{T720A/-}$ mutants and real wild-type littermates. This suggests that the disappearing phenotypes in the secondary screenings might be due to genomic differences between the two wild-type cohorts or due to different environmental conditions in the animal facilities.

In summary, the systemic analyses identified novel phenotypes in the two mutant mouse lines and provided a better understanding of the gene’s function in the regulation of bone and metabolic diseases.

Als ein wichtiger Bestandteil des Wirbeltierskeletts unterliegt der Knochen einer ständigen Erneuerung, um das Gelichgewicht im Mineralhaushalt und physiologische Funktionen aufrecht zu erhalten. Durch ein Ungleichgewicht in der Resorption und Neubildung kann die Knochenhomöostase beeinflusst werden. Knochenerkrankungen stehen häufig im Zusammenhang mit verschiedenen Stoffwechselerkrankungen wie Übergewicht, Diabetes und Herz-Kreislauf-Erkrankungen. In der vorliegenden Arbeit wurden zwei mutante Mauslinien mit abnormen metabolischen Phänotypen analysiert, um die zugrunde liegenden pathophysiologischen Mechanismen zu identifizieren.

Im Primärscreen der Deutschen Mausklinik (GMC) zeigten zwei ENU-induzierte mutante Mauslinien (BAP002, Dll1T720A) ausgeprägte Knochenveränderungen und abnorme Stoffwechselparameter. Im Rahmen dieser Doktorarbeit wurden beide Mauslinien weiter analysiert, um einen Zusammenhang zwischen den Knochen- und Stoffwechselphänotypen zu bestätigen und eingehend zu untersuchen.

Die dominante Mauslinie BAP002 entstammt einem phänotypischen ENU-Mutagenese-Screen für neue Mausmodelle mit gestörtem Knochenstoffwechsel (*OSTEOPATH* Projekt). Als Ursache konnte eine dominante Punktmutation im *Satb2* Gen auf Chromosom 1 identifiziert werden. Heterozygote Mäuse zeigten eine hohe ALP Aktivität im Blut, abnormen Zahnschmelz sowie einen Dysgnathie-Phänotyp. Abgesehen von einer Bestätigung der bereits bekannten Knochenphänotypen, wurden am Mausmodel Knochenzellen und Adipozyten untersucht sowie der Energieverbrauch *in vivo* bestimmt. $\mathit{Satb2}^{V234L/+}$ Mäuse zeigten einen veränderten Knochenumsatz, der durch ein Ungleichgewicht in der Anzahl der Osteoblasten und Osteoklasten charakterisiert war. Darüber hinaus könnte das Auftreten aktivierter beiger Adipozyten in $\mathit{Satb2}^{V234L/+}$ Mäusen das verminderte weiße Fettgewebe und eine erhöhte Insulinsensitivität erklären. Zusammengenommen zeigen die Ergebnisse dieser Arbeit, dass SATB2 nicht nur die Knochenentwicklung reguliert, sondern auch eine neue Rolle im Energiestoffwechsel spielt.

Die Mauslinie Dll1T720 entstammt ursprünglich einem Screening der hausinternen F1-DNA-Probenbank für neue Mutationen des *Dll1* Gens. Homozygote $\mathit{Dll1}^{T720A/-}$ Mäuse, die im Primärscreen der Deutschen Mausklinik analysiert wurden, zeigten Veränderungen im Körpergewicht, in der Größe, in der Körperzusammensetzung und im Skelett im Vergleich zu C3HeB/FeJ Wildtypmäusen. Jedoch wurden nur flüchtige Unterschiede beobachtet, wenn

Dll1$^{T720A/-}$ Mutanten mit echten Wildtypwurfgeschwistern verglichen wurden. Möglicherweise sind die nicht mehr zu beobachteten Phänotypen in den sekundären Screenings auf genomische Unterschiede der beiden Wildtyp-Kohorten oder auf verschiedene Umweltbedingungen der Tierstallungen zurückzuführen.

Zusammenfassend lässt sich sagen, dass durch die systemischen Analysen der beiden mutanten Mauslinien neue Phänotypen identifiziert wurden, die zu einem besseren Verständnis der zugrundeliegenden Genfunktion bei der Regulation von Knochen- und Stoffwechselkrankheiten führen.

2. Introduction

2.1 Skeletal development

2.1.1 Skeletal system and bone

The skeletal system is the body part, that plays an important role on supporting and protecting the organism during development, and the word “bone” is generally used to describe this system. As a rigid organ, bone is composed of around 35% organic matrix and 65% inorganic part[1,2]. The structure of bone is divided into cortical (compact) bone and trabecular (cancellous or spongy) bone. Cortical bone is dense and forms the surface of bones, trabecular bone makes up the interior of most bones. According to the shape, bones can be classified in 5 types (Figure 1A): long bones structurally divided as diaphysis, metaphysis and epiphysis (Figure 1B), short bones, sesamoid bones, flat bones as well as irregular bones. Notably, teeth are considered as a part of the skeletal system but they are not counted as bones[3]. Even though, most chemical compositions of teeth, especially dentin and bone, are very similar[4].

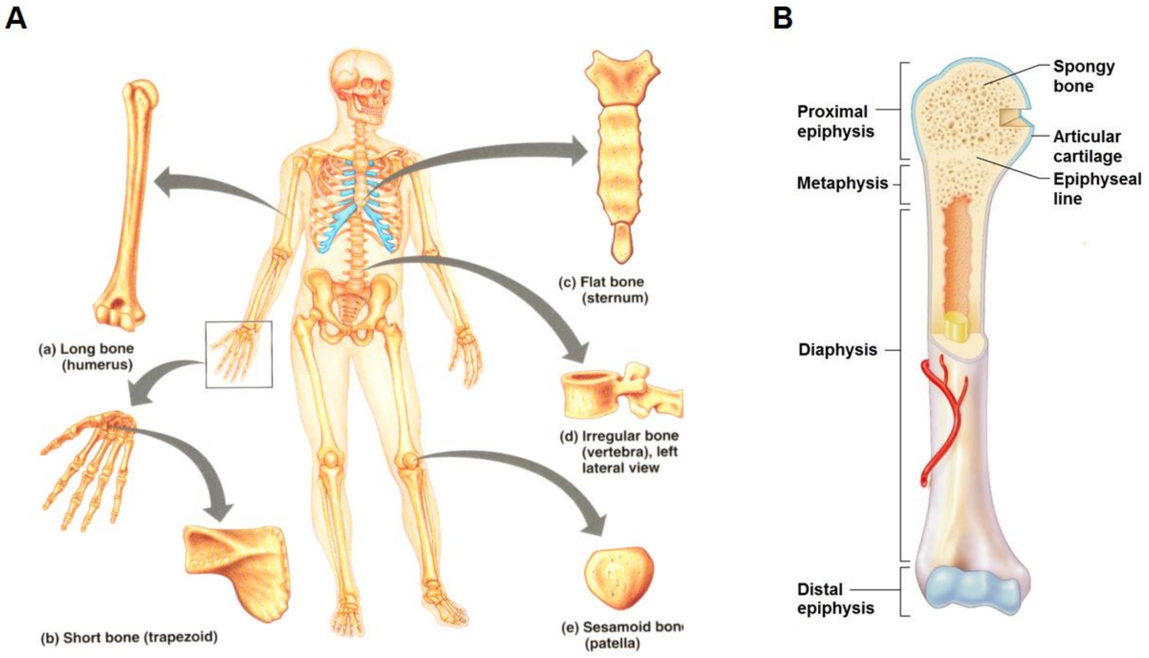

Figure 1. Schematic diagrams of bone classification (A) and long bone (B).

Copyright © 2001 Benjamin Cummings, an imprint of Addison Wesley Longman, Inc.

2.1.2 Bone function

Bones exhibit distinct structure-function relations based on their stiffness[5]. Cortical bone is stiff and typically provides structural support for the body and protects various internal organs. Much more than support and protection, cortical bone acts as insertions for muscles, ligaments and tendons providing movement of the body. The red bone marrow in cancellous bone is the major source for blood cell formation known as hematopoiesis[6]. Furthermore, as the large storehouse of calcium and phosphorus, cancellous bone provides an important reserve supply of mineral homeostasis[7]. Recently, bone was reported to function also as an endocrine organ regulating glucose tolerance and energy expenditure[8].

2.1.3 Bone development

Bone development is divided into two major modes, intramembranous and endochondral ossification, which are both initiated from preexisting mesenchymal cells. Intramembranous or desmal ossification is a direct bone generation in which osteoblasts differentiate from mesenchymal stem cells. This process primarily occurs in the skull, the clavicle and the scapula[9]. During endochondral, ossification, mesenchymal stem cells first differentiate into chondrocytes that secrete a specific extracellular matrix (ECM), which build up the cartilage. The cartilage model grows in length by continuous divisions of the chondrocytes and is then invaded by blood vessels, osteoclasts, bone marrow cells and osteoblasts[9]. The osteoblasts deposit the bone on remnants of the cartilage matrix[10].

Bone development is highly regulated and involves coordinated participation of specific signal transduction and transcription factors. Bone morphogenetic protein (BMP), Wnt/β-catenin and Indian hedgehog (Ihh) signaling all have been reported to stimulate chondrocyte and osteoblast differentiation[11]. Specifically, BMP is indicated to be one of the most important cytokines that regulates the initiation of skeletal formation and induces chondrocyte development both *in vitro* and *in vivo*[12-14]. Smad signaling is involved in BMP signaling and the BMP-Smad signaling pathway plays central roles in the regulation of osteoblastogenesis and chondrogenesis. Sox9 (SYR-Box9), a key transcription factor activated by the BMP pathway, induces runt-related transcription factor 2 (Runx2) and Osterix (Osx), which both regulates the differentiation of osteoblast[15].

2.1.4 Bone cells

Bone is composed of four types of cells, which are classified into two categories. The first category is the osteoblast family, which consists of osteoblasts, osteocytes and lining cells (osteogenic cells). They originate from mesenchymal stem cells (MSC) via osteoprogenitor and preosteoblast stages from which mature osteoblasts, osteocytes and lining cells differentiate. The other category are the osteoclasts, which develop from hematopoietic stem cells[16]. Furthermore, a crosstalk between osteoblasts and osteoclasts was reported[17,18].

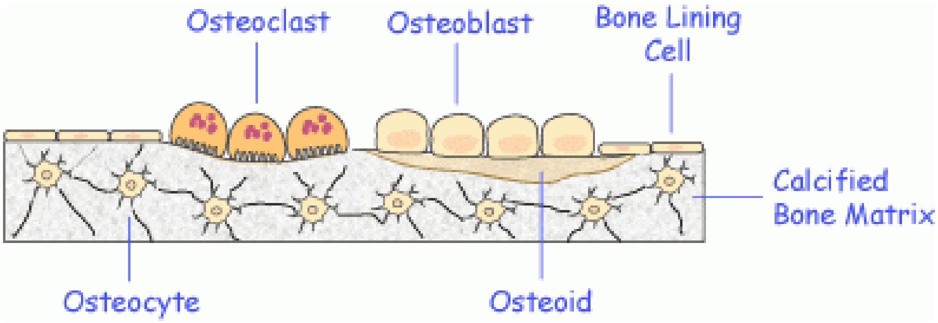

Figure 2. Schematic diagrams of bone-cells classification.

Illustration adopted from http://www.iofbonehealth.org/introduction-bone-biology-all-about-our-bones.

Osteoblasts are the bone forming cells. They are arranged in a single layer on the bone surface and secrete the organic components of the bone matrix. After migrating to the endosteal cortical surface and trabecular bone, the fully matured osteoblasts *e.g.* are producing osteoid, a composition of different types of collagen (mainly type I) and a series of non-collagenous matrix proteins[19]. Osteocalcin (OC) is an important non-collagenous product. As a key marker of osteoblasts, OC is important for modulating bone mass, promoting osteogenic maturation as well as regulation of energy balance[20,21]. Moreover, mature osteoblasts are considered essential for mineralization by regulating local concentrations of calcium and phosphate[22]. Alkaline phosphate (ALP) is a glycosylated protein found primarily in the liver, bone and intestine[23]. Since in bone ALP is synthesized by osteoblasts, it is described as a potential early marker of matrix maturation as well as mineralization, and is positively increased with bone formation and metabolism[24,25].

Osteocytes are star-shaped cells, deriving from osteoblasts when osteoblasts are trapped within the bone matrix. Osteocytes exert their functions in matrix maintenance and the control of mineral homeostasis[26]. Bone lining cells are derived from osteoblasts covering inactive sites (not remodeling) of the bone surface. As inactive forms of osteoblasts, bone-lining cells play essential roles in modulating osteoclasts formation and function as a barrier to protect the bone from harmful chemicals[27].

Osteoclasts are large and multinucleated cells located at the bone surface. After induction by macrophage colony-stimulating factor (M-CSF) and receptor activator of nuclear factor kappa-B ligand (RANKL)[28], multinucleated mutual osteoclasts are attached to the bone surface and develop a sealing zone that encases the so-called ”ruffled border” , a specialized in folded membrane domain where bone resorption takes place[29]. Resorption of bone mineral components is achieved in an acidic environment, which is created by the action of H^+-ATPase[30]. Protein components of the matrix are degraded by TNF-receptor associated protein (TRAP) and Cathepsin K secreted by osteoclasts[31]. Degradation of protein and osteoclast activities are reflected by levels of C-terminal telopeptides of type 1 collagen (CTX-1)[32,33].

2.1.5 Bone modeling and homeostasis

Bone modeling continues throughout the growth period until peak bone mass is achieved. Afterwards, the process of bone maintenance changes to remodeling during adulthood. Bone homeostasis, which is characterized by a close collaboration between osteoblasts and osteoclasts, is a dynamic process that allows maintaining the shape, quality and size of the skeleton. Various bone cells are linked in a complex network of bone multicellular units (BMU). The remodeling cycle begins with osteoclastic resorption. Pre-osteoclasts migrate to the bone surface where they form multinucleated osteoclasts and start to resorb bone matrix. After the completion of resorption, there is a reversal step when mononuclear cells move to the resorbed pits for osteoblast differentiation and osteoid synthesis. This step continues until the trenched bone surface is replaced by osteoid. Finally, the osteoid becomes mineralized, thus ending the bone remodeling cycle[34].

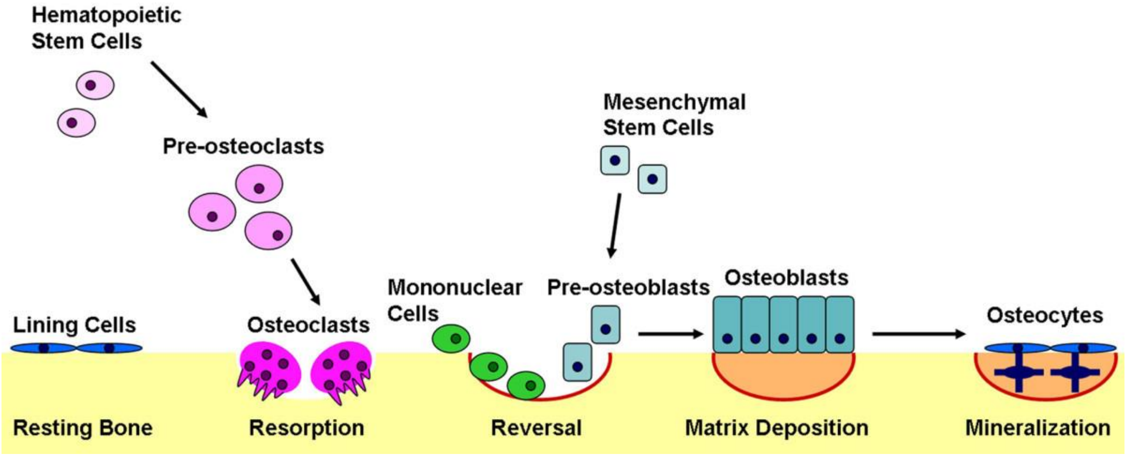

Figure 3. Bone remodeling.

Bone remodeling begins when osteoclasts resorb bone mineral and matrix. Mononuclear cells prepare the resorbed surface for osteoblasts, which generate newly synthesized matrix as they differentiate. Matrix mineralization and the differentiation of some osteoblasts into osteocytes completes the remodeling cycle[35].

The overall integrity of bone remodeling is controlled by several both systemic and local regulation factors[36]. Systemic regulation influences the movement of mineral from bone to the extracellular fluid. Besides the three major calcium regulating hormones parathyroid hormone (PTH), vitamin D and calcitonin[37], estrogen is considered as the most important systemic hormone in maintaining normal bone homeostasis[38]. Bone cells and adjacent hematopoietic cells synthesize several local regulators, including interleukin-1 (IL-1), tumor necrosis factor (TNF) and prostaglandin E2 (PGE-2)[39]. These and other factors can interact with each other and play an important role in the repair of skeletal damage and response to mechanical forces. For example, the receptor activator of nuclear factor kappa-B ligand (RANKL)/RANK/osteoprotegerin (OPG) system is a critical system generally controlling osteoclastogenesis and bone remodeling[40-42].

2.1.6 Tooth enamel and amelogenesis imperfecta (AI)

Enamel is one of the primary tissues building the tooth. The other two hard tissues are dentin and cementum, whereas the dental pulp is the soft tissue (Figure 4). Enamel is highly mineralized and considered as the hardest substance of the human body. The major mineral in enamel is hydroxyapatite, which is a crystalline calcium phosphate. Enamel develops from ameloblasts, which are broken down after enamel maturation[43]. Consequently, there is no possibility of further growth or repair once enamel is completely formed. Although arising from different stem cells, the same signals are shared during dental and bone development including several BMPs, Wnts as well as fibroblast growth factors (FGFs)[44]. Moreover, a number of regulating genes are reported to be expressed in dental maturation such as Sox9[45], and Runx2[46].

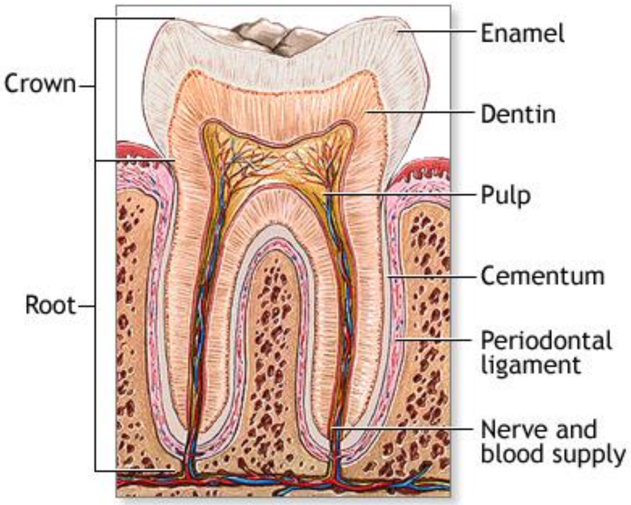

Figure 4. Schematic diagrams of tooth structure.

The components of tooth include dentin, pulp and other tissues, blood vessels and nerves embedded in the bony jaw. The hard enamel covering, located above the gum line, is performed for tooth protection. Illustration adopted from http://www.nlm.nih.gov/medlineplus/ency/imagepages/1121.htm

Amelogenesis imperfecta (AI) is the general term for various inherited conditions with isolated or disturbed enamel layer, and is also used to indicate the presence of an enamel phenotype in syndromes[47]. Currently, mutations in the *AMELX*[48], *ENAM*[49], *MMP20*[50], *KLK4*[51], *SLC24A4*[52] and *LAMB3*[53] genes have been reported to induce AI. However, there is a need for more additional AI candidate genes to be identified in further researches[54].

2.2 Adipose tissue and energy metabolism

2.2.1 Adipose tissue

Adipose tissue is the main storage site for energy excess in the form of triglycerides. These triglycerides are broken down into fatty acids and metabolized to produce adenosine tri phosphate (ATP), which is considered as the energy unit. Except obvious storage function, adipose tissue plays important roles as a thermal insulator from cold and a physical defender against mechanical forces. Furthermore, recent researches revealed that adipose tissues function as an endocrine organ[55]. Rather, functional gain of adipose tissue is in general associated with metabolic diseases such as obesity, type 2 diabetes, cardiovascular diseases as well as cancer.

2.2.2 Classification of adipose tissue

There are two types of adipose tissues: the white and the brown adipose tissue. These two types are identified both in terms of histology and function[56]. White adipose tissue (WAT), which is composed of white adipocytes containing unilocular large lipid droplet, is considered to be an energy storage depot regulating endocrinal activities[57]. By contrast, brown adipocytes of brown adipose tissue (BAT) appear to be multilocular and contain lots of mitochondrial organelles, and participate mainly in inducing energy expenditure in thermogenesis[58].

Apart from WAT and classic BAT, recent studies discovered that a second type of brown adipocyte, which is named beige or brite (brown in white), appears in WAT depots induced upon stimuli such as exposure to cold, specific hormones, or pharmacological treatments with agonists of β-adrenergic receptors or PPARγ[59-61]. Despite distinguishing originations and some potential marker genes[62,63], brown and beige adipocytes are all characterized by their multilocular lipid droplet, high mitochondrial content and BAT-specific gene expression (such as *Ucp1*, *Cidea* and *Pgc1α/Ppargc1a*)[64]. A striking feature of beige adipocytes is that the adipocytes express high levels of thermogenic genes only in response to inducers such as agonists of β-adrenergic receptors or Pparγ[65,66]. However, until now there are no reliable data to determine whether brown and beige adipocytes have different functions.

2.2.3 Development of adipocytes

White and brown adipocytes share a common developmental process - adipogenesis, which is mainly divided into two phases[67]. The first phase, known as determination, involves the generation of the adipogenic cell lineage by differentiation of mesenchymal stem cells (MSCs) into preadipocytes. Preadipocytes are morphologically indistinguishable from their precursors, but have lost the potential to differentiate into other cell types[68]. In the second phase, preadipocytes enter terminal differentiation and take on the characteristics of functional adipocytes.

Aside from similar features, white and brown adipocytes show many functional and developmental differences. WAT compartment starts developing in late gestation. Rapid adipogenesis is stimulated by the increased nutrient availability and induces a marked expansion of adipose tissue. It was demonstrated that the number of white adipocytes increase steadily in the mature fat pad, keeping an approximately rate of 10% annual turnover in humans[67,69]. Moreover, adipogenesis of white adipocytes was considered to play a role in weight changes. Adipocyte cell size notably increased when animals were given a high-fat diet[70].

Different from WAT, subscapular BAT expands primarily *in utero*, possibly to maintain body temperature after birth[58]. Brown adipocytes develop earlier than other fat depots and organize from precursor cells in the embryonic mesoderm. Meanwhile, these early muscle marker myogenic factor 5 (*Myf5*) and paired-box 7 (*Pax7*) expressing precursors were found to give rise to skeletal muscle cells. So BAT was revealed to perform functions which are more closely related to skeletal muscle than WAT[71] and further evidence indicated that there is a diversity between white and brown precursor cells in early development.

It is already known that beige and brown adipocytes derive from distinct cell lineages, but the debate as to where beige adipocytes originate from is still ongoing. Several reports state that the embryonic origination of beige adipocytes arises from pre-existing white adipocytes[65,72]. Therefore, beige adipocytes are considered as a result of "transdifferentiation" of WAT to BAT[73]. However, one recent study suggested that the majority of beige adipocytes develop from a subgroup of the precursor population in place of pre-existing adipocytes[63].

2.2.4 Transcriptional regulation of adipocyte differentiation

Transcriptional regulation of adipocyte differentiation is a widely-stretched network involving gene regulations. Two cell types are primarilly used for differentiation studies: preadipocyte cell lines and mature adipose tissue-derived stromal-vascular precursor cells[74-76]. Over the past decades, peroxisome proliferator-activated receptor γ (PPARγ) and CCAAT-enhancer binding proteins (C/EBPs) were considered to play important roles in adipogenesis and the maintenance of adipocytes[77,78]. PPARγ's action is mediated through two protein isoforms: PPARγ1 and PPARγ2[68], which are generated by alternative splicing and promoter usage. C/EBPs perform biological functions through their family members, such as C/EBPα, C/EBPβ and C/EBPδ, after activation by glycogen synthase kinase-3β and mitogen-activated protein kinase (MAPK)[79]. In both WAT and BAT, cooperation of PPARγ and C/EBPα positively regulates their own expression and initiates activation of downstream metabolic genes, whose expressions are induced to subsequently regulate terminal adipocyte differentiation.

Apart from having important roles in WAT and BAT differentiation, PPAR-γ and C/EBPβ also act as key regulators in the beige adipogenic program. Treatment with PPAR-γ agonists or C/EBPβ potentially drive BAT gene marker expression and beige adipogenesis in murine WAT adipocyte[66,80]. Several factors are activated to regulate beige adipocyte recruitment, such as the PPAR-γ co-activators PGC1α, PRDM16 and SRC1, as well as transcription factors PPAR- α and FOXC2. Furthermore, miRNAs have merged as contributors to regulate adipogenesis in multiple adipose tissues, including miR-27[81], miR-133[82] and miR-155[83].

2.2.5 Adipose tissue and energy metabolism

Energy homeostasis is a balance between food intake (energy input) and energy expenditure by the body for organism's health and to perform physical work[84]. Energy balance is accomplished through a highly integrated control system by increasing energy expenditure during energy excess, and to decrease energy expenditure during energy deficit. Additionally, adipose tissue plays a crucial role in regulation of energy balance[85-87] by alternating their own metabolism[88]. Adipose tissue is revealed to be regulated by some hormones.

Leptin

Leptin is a 16-kilodalton hormone produced predominantly by WAT[89] The expression of leptin positively increase with the gain of adipose tissue[90]. Leptin plays important roles in suppressing appetite and elevating energy expenditure[91]. Leptin performs these functions by binding to its receptor[92], which is highly expressed in the hypothalamus. *Ob/ob* mice, which cannot produce leptin, become extremely obese in *ad libitum* feeding regimens. This weight gain can be reversed by administration of leptin, indicating that leptin has a high capacity to increase energy expenditure.

Adiponectin

Adiponectin is a 30-kilodalton protein secreted primarily from mature adipocytes. Unlike leptin, adiponectin levels are negatively associated with obesity and insulin resistance. Conclusions drawn from several studies suggest that adiponectin is playing an important role in energy metabolism, which is mediated through two adiponectin receptors (AdipoR): AdipoR1 and AdipoR2. Expression of both receptors results in the activation of adenosine monophosphate (AMP)-activated protein kinase and PPARα ligand, leading to fatty acid oxidation, glucose-lowering effects and ameliorates insulin resistance in mice[93-95]. It was concluded that adiponectin is an abundantly expressed hormone that performs a potent insulin-sensitizing effect by binding to its receptors AdipoR1 and AdipoR2.

Insulin

Insulin is a peptide hormone, produced by β cells in the pancreas. As a core hormone of energy metabolism, insulin mainly maintains the concentration of blood glucose through regulating glucose homeostasis[96]. Insulin stimulates the signaling network by binding to the insulin receptor (IR). Insulin resistance is defined as an inadequate response to the physiological effects of circulating insulin, which is processed in insulin target organs (skeletal muscle, liver and adipose tissue). Elevated insulin resistance in the first instance leads to increased secretion of insulin to maintain its normal metabolic function. By contrast, high insulin sensitivity indicates that insulin receptors become more sensitive and less insulin has to be secreted by the pancreas to normalize glucose levels.

Apart from the function performed in the control of glucose concentration, insulin is also required for proper energy regulation through associations between leptin and adiponectin[97]. Many studies have proved that insulin directly stimulates leptin expression both *in vitro* and *in vivo*[98,99]. The chronic administration of leptin to lipodystrophic patients was able to improve the unbalanced glucose metabolism, which suggested leptin itself as a signal contributor to regulate insulin sensitivity[100]. Additionally, adiponectin was revealed to improve insulin sensitivity[101] and energy metabolism via the PPARα and AMPK pathways[102].

2.2.6 Adipose tissue and metabolic diseases

Despite as an endocrine organ, adipose tissue plays a primary role in energy storage in the form of fat. Obesity is the result of an imbalance between energy intake and energy expenditure and is identified through abnormal and excessive fat gathering in the body[103]. Establishment of obesity is not merely associated with pathological changes in adipocytes, but also associated with dysfunctions in adipocytes and macrophages, which are capable of collecting lipid and secreting cytokines[104]. Many factors, including a high-fat diet, hormone abnormalities as well as a lack of physical activities, are able to promote fat accumulation in adipose tissue and obesity development[105-107].

Obesity is thought to be the primary cause of type-2 diabetes, a metabolic disease typically characterized by insulin resistance. Enlarged adipocytes in obese subjects increased the secretion of free fatty acids (FFAs) and tumor necrosis factor-α (TNF-α), which further drives insulin resistance[108]. Moreover, adipose tissues are able to affect the progress of diabetes process by adipose-derived hormones such as leptin and adiponection[109,110].

Several studies have shown an interrelationship between adipose tissue and bone tissue, and described its contribution to the maintenance of energy balance and the development of the of metabolic syndrome[111]. Adipocytokines are considered to play a major role during the development of bone diseases. For example. leptin negative influences bone formation by binding to its receptor in the hypothalamus[112], while adiponectin has been shown to possess a suppressing effect on bone resorption activity[113]. Abnormal leptin and adiponectin levels in dysfunctional adipose tissue lead to an imbalance between bone formation and resorption as manifested in several osteodystrophies[114,115]. In addition, osteocalcin (OC), a secreted bone tissue factor, modulates bone and energy homeostasis[116] and has been recognized as an endocrine factor affecting adipocytes and pancreatic β cells[117,118]. A recent study described that in primary cultured adipocytes the transport of glucose as well as insulin sensitivity could be directly modulated by OC[119].

Therefore, studying adipose-tissue dysfunction provides a framework for understanding adipocyte expansion, hormone secretion as well as insulin resistance may help to identify new strategies for prevention and treatment of metabolic diseases.

2.3 The *Satb2*^{V234LMdha} mouse model

The BAP002 (**b**one **a**lkaline **p**hosphatase #2) mouse line has been identified from the large scale genome-wide Munich *N*-ethyl-*N*-nitrosourea (ENU) mutagenesis screen, exhibiting high total alkaline phosphatase (ALP) blood activities, abnormal tooth enamel and dysgnathia as phenotypes. General dysmorphological analysis of mutant mice revealed abnormal brittle teeth, decreased bone mineral content and reduced bone density compared with wild-type mice. Furthermore, decreased body weight and fat mass were exhibited in mutant, but not in wild-type mice. Next generation sequencing identified a point mutation in exon 6 of special AT-rich sequence-binding protein 2 gene (*Satb2*) on chromosome 1, which leads to a valine to leucine exchange at amino acid position 234 (V234L). The mouse line was given the official name *Satb2*^{V234LMhda}.

SATB2 protein, composed of 733 amino acids, specifically binds to nuclear matrix attachment regions (MAR). Similar to its homologous protein SATB1, SATB2 is composed of three motifs including two CUT domains (aa352-aa437 and aa482-aa560) and a classic homeodomain (aa614-aa677). SATB2 is extraordinarily high conserved between human and mice with only two predicted amino-acid substitutions among all residues[120].

Encoding a transcriptional factor, *Satb2* is widely expressed during embryonic development. In zebrafish, *Satb2* shows stage-specific expression and regulates cell migration, yolk formation and neural-crest cell development[121,122]. In mouse, *Satb2* expression was first detected at E10.5 in the maxillary component of the first pharyngeal arch and the lateral aspect of the frontonasal process that form the primary palate. The strongest expression has been observed at E13.5 in the mesenchyme underlying the medial edge epithelia of the palatal shelf. The expression was markedly down-regulated after E14.5 by the time of palatal shelf fusion[123]. Interestingly, data from the Craniofacial and Oral Gene Expression Network (COGENE) project suggest that human *SATB2* is present in the embryonic face at low levels[123]. Furthermore, *Satb2* is also expressed in the cortex of the developing brain and in osteoblasts during bone development[124].

During adulthood, expression of *Satb2* has been detected in the spinal cord, kidneys, leukocytes, osteoblasts and the central nervous system (CNS)[124,125]. Besides the strong expressions in the CNS and the growth plate area, human SATB2 was found to be strongly expressed in the majority of glandular cells lining the lower gastrointestinal tract, including the rectum, colon and the appendix[126]. In contrast, *Satb2* was weakly expressed in lymphoid cells and in testis[120]. Since expression of SATB2 was found in all analyzed colorectal cancer tissues, *Satb2* expression levels are used as a marker for colorectal tumors in clinical differential diagnostics[127,128].

Taken together, SATB2 is playing key roles in craniofacial patterning, osteoblast differentiation, tumor metastasis prognosis and neuron identification[125,129,130]. The diverse functions of SATB2 are mediated through regulations of several transcription factors (such as Runx2 and Osterix)[124,131] and miRNAs (such as miR23a-27a-24-2 and miR-34s)[131,132]. In addition, SATB2 can contribute directly to the regulation of osteoblast differentiation by binding to osteoblast associated genes or indirectly by binding to enhancers/inhibitors of transcription thus modulating osteoblast differentiation[133]. The important role of *Satb2* in skeletal development has been proved in *Satb2*$^{-/-}$ and *Satb2*$^{+/-}$ knockout mice[124,134]. Many cases of human *SATB2* haploinsufficiency or mutation have been described presenting teeth, palate and craniofacial dysmorphisms[123,135,136].

Satb2$^{V234L/+}$ mice displayed a strong teeth phenotype and altered blood and bone parameters related to impaired bone turnover. Moreover, *Satb2*$^{V234L/+}$ mice displayed some metabolism-related phenotypes (decreased body weight, decreased fat mass and increased glucose tolerance), which haven’t been reported yet. The results obtained in the *Satb2*^{V234LMhda} mouse line described within this thesis, give new hypotheses regarding bone and energy metabolism on pathological and molecular levels.

2.4 The *Dll1*^{T720A} mouse model

The *Dll1*^{T720A} mutation was isolated by screening of the F1 DNA archive of the Munich ENU mutagenesis project for certain alleles of the *Dll1* gene in the C3HeB/FeJ genetic background[137]. The *Dll1*^{T720A} mouse line was generated by *in vitro* fertilization and embryo transfer using frozen sperm of the respective F1 animal. *Dll1*^{T720A} mice contain an amino acid exchange in the conserved C-terminal PDZ-binding motif from threonine to alanine at position 720 (T720A). *Dll1* (Delta-like 1) belongs to the Notch ligand family, that was identified to activate corresponding Notch receptors in mammals[138]. Notch signaling is known to regulate differentiation processes in early embryonic stage[139], and several studies have revealed that mutations of Notch receptors or their ligands associate with developmental anomalies, neurodegenerative diseases and cancer[140,141,142]. PDZ domain containing proteins are often involved in the regulation of cell adhesion and intercellular communication[143]. Therefore, the amino-acid exchange in *Dll1*^{T720A} mice was considered to impair the intracellular binding of DLL1 to PDZ-domain containing proteins and thus, influencing the Delta-Notch signaling pathway (Gerhard Przemeck, personal communication).

Previous primary screening in the German Mouse Clinic (GMC) had shown that homozygous *Dll1*$^{T720A/-}$ mice present reduced bone parameters (bone mineral density and bone mineral content), reduced body weight and fat content as well as some decreased clinical parameters, involving cholesterol, ferritin and transferrin. In contrast, the locomotor activity was increased in *Dll1*$^{T720A/-}$ mice compared to C3HeB/FeJ wild-type mice, which were not littermates. Therefore, within this thesis parts of these GMC measurements were repeated with an age-matched wild-type littermate cohort (out of heterozygous *Dll1*$^{T720A/+}$ intercrosses) to verify the phenotypes expressed in the primary screen.

2.5 Thesis outline

Satb2^{V234LMdha} and *Dll1*^{T720A} are two ENU mutagenesis induced mouse lines, both identified with distinct bone and body weight related phenotypes. The two lines were systemically analyzed to verify and follow up these alterations and to give further understanding of the underlying mutations not only in bone but also in other metabolic tissues. Possible mechanisms leading to multifactorial diseases were investigated.

Dll1$^{T720A/-}$ mice expressed alterations of bone and body-weight related parameters as well as increased locomotor activity in the primary screen of the GMC. Since no real wild-type littermates have been available in preliminary screening, new *Dll1*$^{\mathrm{T720A}}$ cohorts were bred as a first step and parts of the measurements were then repeated with age-matched *Dll1*$^{T720A/-}$ and wild-type littermate cohorts.

The *Satb2*^{V234LMdha} (BAP002) mouse line is a dominant murine model characterized by low bone density and high total ALP activities in plasma. In addition, mutant mice showed brittle teeth and jaw malformations, similar to other osteoporotic animal models[144,145]. Interestingly, *Satb2*$^{V234L/+}$ mice exhibited decreased body weight and fat mass and increased lean mass. To investigate the hitherto new and so far not described effect of *Satb2* on energy metabolism, pathological and molecular analyses were performed in *Satb2*^{V234LMdha} mice to confirm these observations.

3. Materials and Methods

3.1 Materials

3.1.1 Chemicals and buffers

All chemicals were purchased from Sigma-Aldrich, Merck, Invitrogen, AppliChem, Biozym, Qiagen and Roche, if not otherwise mentioned in the text.

PBS (10×)

80 g	NaCl
2 g	KCl
17.8 g	$Na_2HPC*2H_2O$
2.72 g	KH_2PO_4

Dissolved in ddH_2O and adjusted to pH 7.3

ddH_2O was added to receive 1 L

PBST

100 mL	10× PBS
500 µL	Tween20 (f.c. 0.05%)
900 mL	ddH_2O

RIPA buffer

15 mL	5M NaCl
5 mL	NP40
25 mL	10% Natriumdeoxycholate
2.5 mL	10% SDS
25 mL	1 M Tris-HCl (pH 8.0)

pH was adjusted to 8.0 and added to 500 ml with ddH_2O

0.5 M Tris-HCl buffer (for Western Blot stacking gels)

6.05 g	Trizma base

adjust to pH 6.8

add to 100 mL with ddH_2O

add 0.4 g SDS

store at 4°C

Upper 1.5 M Tris-HCl buffer (for Western Blot resolving gels)

91 g	Trizma base

adjust to pH 8.8

add to 500 mL with ddH_2O

add 2 g SDS

store at 4°C

6× SDS loading buffer

3 mL	Glycerol
7 mL	Lower Tris buffer
3 mg	Bromphenol blue
375 µL	β-mercaptoethanol
1 g	SDS

5× SDS running buffer

15.1 g	Trizma Base
72.0 g	Glycine
5.0 g	SDS

add to 1L with ddH_2O

store at 4°C

10× Transfer buffer

30.03 g	Trizma Base
144.1 g	Glycine

add to 1L with ddH$_2$O

store at 4°C

1× Transfer buffer

100 mL	10× Transfer buffer
200 mL	Methanol
700 mL	ddH$_2$O

Stripping buffer

15 g	Glycine
1 g	SDS
10 mL	Tween20

adjust to pH 2.2

add to 1L with ddH$_2$O

0.1% Sodiumbicarbonate buffer

1 g	Sodium bicarbonate

adjust to pH 8.0

add to 1 L with ddH$_2$O

TRAP buffer

0.328 g	Sodium acetate
0.461 g	Sodiumtartrate-dihydrate

adjust to pH 5.0

add to 100 mL with ddH$_2$O

TRAP staining solution

4 mg	Naphtol AS-MX Phosphate
24 mg	Fast red violet LB salt
400 mL	Dimethylformamide
200 mL	Triton-X

add to 20 mL with TRAP buffer

spin down just before use

Toluidine blue buffer

0.68 g	Sodium acetate
0.9 mL	Glacial acetic acid

add to 100 mL with ddH$_2$O

Toluidine blue staining solution

0.5 g	Toluidine blue o

add to 100 mL with Toluidine blue buffer

add to 900 mL with ddH$_2$O

3.1.2 Primers and antibodies

Primary antibody	Host	Customer	Reference number
Satb2	rabbit	Abcam	ab34735
Satb2	rabbit	Abcam	ab69995
GAPDH	rabbit	Cell Signaling	2118
UCP1	rabbit	Abcam	ab10983

Primer name		Sequence (5'-->3')
Genotyping primer		
Satb2 Genotyping	F	TGAACTCCAGTCACCCTGTTT
	R	CCCTTCCTAAATTAAGGGTTGAA
Dll1T720A Genotyping	F	CACACAGCAAACGTGACACCAAGTGCCAGTC
	R	CAAGATAGACGTGTGGGCAGTGCGTGCTTC

qRT-PCR housekeeping gene primer

YWHAZ	F	TGCAAAAACAGCTTTCGATG
	R	TCCGATGTCCACAATGTTAAGT
Rpbl13a	F	TGAAGCCTACCAGAAAGTTTGC
	R	GCCTGTTTCCGTAACCTCAA
SDHA	F	GCAATTTCTACTCAATACCCAGTG
	R	CTCCCTGTGCTGCAACAGTA
B2M	F	GCTATCCAGAAAACCCCTCA
	R	GGGGTGAATTCAGTGTGAGC
UBC	F	AGCCCAGTGTTACCACCAAG
	R	ACCCAAGAACAAGCACAAGG
HMBS	F	GCTGAAAGGGCTTTTCTGAG
	R	TGCCCATCTTTCATCACTGT
Tbp	F	CCCCACAACTCTTCCATTCT
	R	GCAGGAGTGATAGGGGTCAT
Fbxw2	F	ATGGGTCACCAAGGTGGTT
	R	TCCCAATTGGCCAAATCTT
HPRT	F	CCTAAGATGAGCGCAAGTTGAA
	R	CCACAGGACTAGAACACCTGCTAA
Tuba1a	F	AAGGAGGATGCTGCCAATAA
	R	GCTGTGGAAAACCAAGAAGC
Zfp91	F	TTGCAGCACCACATTAAATAC
	R	ATCCCTCTGGTCTGTATGATG
Cyc1	F	GTTCGAGCTAGGCATGGTG
	R	CGGGAAAGTAAGGGTTGAAATAG
ATP5B	F	GGTTTGACCGTTGCTGAATAC
	R	TAAGGCAGACACCTCTGAGC
B2M	F	GCTATCCAGAAAACCCCTCA
	R	GGGGTGAATTCAGTGTGAGC
Actin beta	F	GCCACCAGTTCGCCAT
	R	CATCACACCCTGGTGCCTA
Pgk1	F	GAGCCCATAGCTCCATGGT
	R	ACTTTAGCGCCTCCCAAGA

GAPDH	F	TGGAGAAACCTGCCAAGTATG
	R	CATTGTCATACCAGGAAATGAGC

qRT-PCR candidate gene primer

Cidea	F	CAGTGATTTAAGAGACGCGG
	R	TCTGCAATCCCATGAATGTC
Ucp1	F	TCTCTGCCAGGACAGTACCC
	R	AGAAGCCACAAACCCTTTGA
Isr2	F	GAGTGTGTGGGGGTCCAG
	R	GTAGCGCTTCACTCTTTCACG
Akt2	F	CAGAATGCCAGCTGATGAAG
	R	GCATCCACTCTTCCCTCTCA
Slc2a4	F	CAGCGCCTGAGTCTTTTCTT
	R	CAGTGTTCCAGTCACTCGCT
Mapk8	F	GTTCTCCGCTACGGGCTT
	R	GTCACGTTTGCTTCTGCTCA
Mapk9	F	TGGCGGACTCAACTTTCACT
	R	TGACAGCCACATTTATCCCA
Ptpn1	F	GAGACGGGAGGAACATGACA
	R	CCAGGGTTACTCTTACTGGGC
Pgc1α/Ppargc1a	F	TGCCATTGTTAAGACCGA
	R	CCAGAGTCACCAAATGACC
Satb2	F	ACAGGCCAAAACCTCGAC
	R	AGCCCTGACTTTTGTTTGC
Satb2 long version	F	CGTGGGAGGTTTGATGATTC
	R	ACTCTGGGAGAGAGGGCATT
Satb2 short version	F	GCCGTGGGAGAGTATGATTT
	R	TCTGACAATAATCCCTGTGTGC

3.1.3 C3H inbred mouse strains

The mouse strain used for inbreeding during the studies was C3HeB/FeJ originally purchased from the Jackson Laboratory (Bar Harbour, Maine).

3.2 Methods

3.2.1 Animal housing and caretaking

Both BAP002 and Dll1T720A mutant mice were generated within the large-scale genome wide Munich ENU mutagenesis project (MEP)[146]. The mice were kept in a 12-hour dark-light cycle and fed with standard chow (TPT total pathogen free chow #1314, Altrumin, Lage, Germany) and water *ad libitum*. Health monitoring was performed quarterly following FELASA recommendations[147] by sentinels receiving dirty bedding. Housing and handling of all mice was according to the federal animal welfare guidelines. A conventional cage system under filter tops was used (type-II cages, 370 cm^2 base areas). The cages were enriched with plastic igloos. Mice were grouped as three mice per gender after weaning. All animal studies were approved by the state ethics committee.

3.2.2 Molecular methods

3.2.2.1 Isolation of DNA for sequencing and genotyping

For DNA isolation, tail clips were taken at weaning (2-3 mm). DNA isolation was performed with the QIAamp® DNA Mini Kit (Qiagen, Hilden, Germany) according to the manufacturer's manual. Briefly, tissue was incubated in digest buffer containing 180 µL ATL-buffer and 20 µL Proteinase K at 56°C for longer than 4 hours. 200 µL AL-buffer was added after inactivation and incubated at 70°C for 10 minutes. Following, 200 µL 100% EtOH was added and the lysate transferred to a QIAGEN binding column. The column was centrifuged at 8,000 rpm for 1 minute, the bounded DNA washed with 500 µL AW1 and then AW2-buffer and centrifuged for 1 minute each at 8,000 rpm and 13,000 rpm respectively. Spin columns were centrifuged again for 3 minutes at 13,000 rpm to ensure that all residual ethanol was removed. 50 µL Ampuwa® (pure water for injections) was added to elute DNA by centrifugation at 8,000 rpm for 1 minute.

3.2.2.2 Isolation of RNA for gene expression profiling and qRT-PCR

Total RNA from tissues was isolated with the RNease Mini Kit (Qiagen). Isolated pancreatic tissue was incubated in RNAlater® buffer (Qiagen) at 4°C over night before transfer to -80°C.

Brain, liver and adipose tissues were snap frozen and transferred to -80°C for storage. Frozen tissues were thawed in Trizol (Invitrogen, USA) and homogenized using a Polytron Homogenizer. Isolation of individual samples was performed corresponding to the enclosed manual. The RNA concentration was calculated by OD260/280 with an ND-1000 Spectrophotometer (NanoDrop, Wilmington, USA). RNA integrity was measured using the RNA 6000 Pico Kit (Agilent, Waldbronn, Germany). RNA samples were stored at -80°C in RNA free water (Qiagen) for expression profiling or qRT-PCR experiments.

3.2.2.3 Isolation of protein for Western blot

Ice cold RIPA buffer containing the complete Mini EDTA-free Protease Inhibitor tables (Roche, Penzberg, Germany) was added to the tube with snap frozen tissue. The tissue was homogenized on ice for 1 minute using a DIAX900 Homogenizer (Heidolph, Kelheim, Germany). Samples were centrifuged at 13.000 rpm for 15 minutes at 4°C. Centrifugation was repeated to spin down and afterward stored at -80°C.

3.2.2.4 Sequencing and genotyping

3.2.2.4.1 Next generation sequencing (NGS)

In-solution targeted enrichment was performed for exonic sequences of both mutant and wild-type mice with the SureSelectXT Mouse All Exon kits (Agilent, Santa Ckara, USA). After indexing libraries of both genotypes, ten other mouse exome libraries were collected together and sequenced as 100 bp paired-end runs on four lanes of a flow cell with a HiSeq2000 system (Illumina, San Diego, USA). Read alignment of the mouse genome assembly mm9 was done with BurrowsWheeler Aligner (BWA, version 0.5.9). Some insertions, deletions and single-nucleotide variants were detected with SAMtools (v0.1.7).

3.2.2.4.2 Genotyping

BAP002

Taq polymerase (Qiagen, Germany) was used for PCR reactions:

Component	**Volume**
Q-solution (5×)	5.0 µL
PCR Buffer (10×)	2.5 µL
dNTPs (10 mM)	0.5 µL
Forward primer (10 µM)	1.0 µL
Reverse primer (10 µM)	1.0 µL
Taq Polymerase (5U/µL)	0.3 µL
Ampuwa®	13.7 µL
DNA (10-100 ng/µL)	1.0 µL
	∑25.0 µL

Thermal cycler conditions were used according to the manufacturer’s protocol

94°C	4 min	35×
94°C	30 seconds	
60°C	30 seconds	
72°C	40 seconds	
12°C	until end	

Annealing temperature and elongation time can be adjusted for individual PCR programs. PCR products were checked on a 1% TAE agarose gel.

For sequencing reactions, PCR products were purified using the Agencourt® PCR Purification Kit (Beckman Coulter, USA) according to the manual. The BigDye v3.1 Mastermix (Life Science, UK) was used for fluorescence labeling of DNA. 1 µL forward/reverse primer and 2 µL purified DNA were added to a new plate and dried with air flow. Afterwards 5 µL HPLC graded water (Merck, Germany), 4 µL 5× Sequencing buffer (Life Science, UK) and 1 µL BigDye v3.1 were added to the individual sample.

The thermal cycler condition used for “BigDye PCR”

95°C	1 min	39×
95°C	5 seconds	
50°C	10 seconds	
62°C	4 min	
12°C	until end	

Afterwards, the CleanSEQ Purification Kit (Beckman Coulter, USA) was used to purify the PCR products according to the manufacturer’s manual. Sequence detection was performed with an ABI-3730 (Applied Biosystems, Germany) Sequencing data were analyzed using Sequencer 4.6 (Genecodes, USA).

Dll1T720A

The following thermal cycler conditions were used:

94°C	5 min	34×
94°C	30 seconds	
65°C	1 min	
72°C	30 seconds	
72°C	5 min	
12°C	until end	

Based on a G to A mutation in exon 10 in Dll1T720A mutant mice, Bpu10I was used to digest the PCR amplification product, whose size is 724 bp. After restriction digest with Bpu10I 3 bands (419 + 219 + 86 bp) appeared from Dll1T720A mutants, whereas wild-type DNA gives 2 bands (638 + 86 bp) only.

3.2.2.5 cDNA synthesis and qRT-PCR

cDNA synthesis

The SuperScript® II Kit (Invitrogen, Carlsbad, USA) was used for cDNA synthesis. A total of 500 ng RNA was mixed with 1 µL dNTPs (10 mM) and 2 µL Random Primer Mix (New England, UK) added up to 12 µL with Ampuwa® before preannealed at 65°C for 10 min. Afterwards, 8 µL mastermix was added for the reverse transcription (see below). The cDNA synthesis reaction was performed at 42°C for 60 min, followed by an additional incubation step at 70°C for 15 min for enzyme inactivation. The synthesized cDNA was stored in -80°C and afterwards 1:10 dilutied with Ampuwa® for qRT-PCR reaction.

Mastermix for reverse transcription:

Component	**Volume**
5× First –Strand Buffer	4.0 µL
0.1 M DTT	2.0 µL
RNaseOUT	1.0 µL
SuperScript® II	1.0 µL
	∑ 8.0 µL

qRT-PCR

The following mix was used for qRT-PCR reaction:

Component	**Volume**
Gene-specific primers (forward and reverse)	2.0 µL
1:10 dilution of cDNA template	2.0 µL
Power SYBR Green (2×)	10.0 µL
Ampuwa®	6.0 µL
	∑ 25.0 µL

Gene-specific primers and Power SYBR Green used in the reaction were purchased from Metabion (Martinsried, Germany) and Applied Biosystems (Darmstadt, Germany), respectively. The qRT-PCR reaction was performed with the Roche LightCycler®480 System

(Roche, Penzberg, Germany). Two ideal housekeeping genes (HKGs), whose expression were most stable in individual organ, were identified using *geNorm* (version 3.5) from 16 HKGs as described[148]. The cDNA sequence of candidate genes was got from NCBI. Each primer was designed across an exon-exon junction with Primer3 to avoid amplification of genomic DNA, allowing binding of primers exclusively after splicing. Expression levels of mRNA dependent on the crossing point (Cp) value and amplification efficiency of the transcripts after normalized to reference HKGs[149]. Calibrator normalization was performed with control samples set to 100%.

3.2.2.6 Western blot

10% polyacrylamide gels were prepared for Western blot analysis. Protein samples were added for separation after denaturation at 99°C for 5 minutes. Spectra™ Multicolor Broad Range Protein Ladder (Fermentas, Schwerte, Germany) was used for the assessment of molecular weights. After the gel electrophoresis (40V for 40 minutes at the beginning and 100 V until the end), proteins were blotted using a tank transfer system on a Hybond-PVDF membrane (GE Healthcare, München, Germany), which was activated in 100% methanol for 10 seconds, incubated in ddH$_2$O for 5 minutes and then equilibrated in transfer buffer with Whatman® paper (Biometra, Göttingen, Germany) for at least one. Blotting was performed at 200 mA for 1 hour. Afterwards, the membranes were blocked in 5% skimmed milk in TBST for 3 hours. The blots were incubated with 1:5000 diluted primary antibodies at 4°C overnight according to manufacturer's recommendations. After 3 times washing in TBST for 10 minutes, membranes were incubated in 1:20000 diluted HRP-conjugated secondary antibodies for 1 hour at RT. Membranes were again washed 3 times for 10 minutes. Protein bands were visualizaed using the HRP luminescent substrate provided in the Western Lightning® Plus-ECL Kit (Perkin Elmer, Massachusetts, USA) and detected with Amersham™ hyperfilm ECL autoradiography films (GE Healthcare). For reprobing, the blot was incubated two times in fresh stripping buffer for 10 minutes before a two times incubation in PBS for 10 minutes. Afterwards, the blot was incubated two times for 5 minutes in PBST and transferred to blocking buffer before incubation. A 1:10000 diluted GAPDH antibody was used as loading control. All antibodies were diluted with 5% skimmed milk in PBST.

3.2.2.7 Enzyme-linked immunosorbent assays (ELISA)

All plasma samples used for ELISA measurements were taken from overnight-fasted mice. Absorptions in ELISA assays were measured using the TECAN GeniosPRO (TECAN, Grödig, Austria).

CTX-1 ELISA

The RatLaps^{TM}EIA Kit (IDS, Boldon, UK) was used for assays of CTX-1 levels. According to the kit manual, 100 µL Biotinylated RatLaps Antigen was added to each well and incubated for 30 minutes at RT. The plate was washed with 300 µL washing solution per well for 5 times before 20 µL samples solution mixed with 100 µL primary antibodies were added into each well for overnight incubation at 4°C. The plate was washed again with 300 µL washing solution per well for 5 times, before the 100 µL Peroxidase conjugated antibody was added to each well and the plate incubated for 1 hour at RT. The plate was washed again and 100 µL substrate solution was pipetted into each well for a 15-minutes incubation at RT in darkness. Finally, 100 µL stop solution was added per well to the plate and the absorbance was measured at 450 nm.

Adiponectin ELISA

The Mouse Adiponectin/Acrp30 Quantikine ELISA Kit (R&D, Minneapolis, USA) was used for assays of adiponectin levels. Plasma samples required a 2.000-fold dilution prior to assay. 50 µL diluted samples and 50 µL assay solution were well mixed and added into each well and incubated for 3 hours at RT. The plate was washed for 5 times with 400 µL washing buffer per well and incubated in 400 µL Mouse adiponectin conjugate per well for 1 hour at RT. Washing steps were repeated 5 times before 100 µL substrate solution was added to each well and plate incubated for 30 minutes under light protection. Subsequently, 100 µL Stop solution was added to each well and the optical density was measured at 450 nm.

Leptin ELISA

For the measurement of leptin levels, the Mouse Leptin ELISA Kit (EMD Milipore, Missouri, USA) was used according to the kit’s manual. 10 µL plasma sample dilutions (1:1 diluted with assay buffer) per well were mixed gently with 40 µL Assay buffer and 50 µL Transfer

Antiserum solution and incubated for 2 hours at RT. The plate was washed with 300 µL washing buffer per well for 3 times and before 100 µL detection antibody was added into each well and the plate incubated for 1 hour at RT. The plate was washed for 3 times again before enzyme solution was added and incubated for 30 minutes at RT. The plate was washed again with 300 µL washing buffer per well for 6 times, followed by the addition of 100 µL substrate solution to each well and incubation for approximately 20 minutes at RT. 100 µL stop solution was added to each well and the absorbance read at 450 nm.

Insulin ELISA

The Mouse Insulin Kit was purchased from Mercodia (Mercodia, Uppsala, Sweden). According to the manufacturer's protocol, 25 µL plasma samples and 100 µL enzyme conjugate solution were pipetted into each well and incubated for 2 hours at RT. The plate was washed 6 times with 700 µL washing buffer per well before 200 µL substrate 3,3',5,5'-Tetramethylbenzidine (TMB) was added into each well. The plate was incubated for 15 minutes at RT followed by adding of 50 µL stop solution to each well. Optical density was measured at 450 nm.

Osteocalcin ELISA

For the analysis of osteocalcin levels, the Mouse Osteocalcin ELISA Kit (Immutopics, San Clemente, USA) was used. According to the kit's manual, both controls and plasma samples were diluted 1:11 prior to the experiment. 50 µL Osteocalcin Biotinylated Antibody was added to 25 µL standard and diluted samples and incubated for 1 hour at room temperature. The plate was washed 5 times with 350 µL washing solution per well. 100 µL Mouse Osteocalcin conjugated antibody was pipetted into each well. The plate was incubated at RT for one hour without light exposure. The plate was washed 5 times with 350 µL working solution per well and incubated for 30 minutes in the dark after 100 µL substrate solution was added to each well. Finally, reaction was stopped with 50 µL stop solution added to each well and absorption was measured at 450 nm in a plate reader.

Thyroxine (T4) ELISA

T4 measurements were performed with the Thyroxine (T4) ELISA Kit (Calbiotech, Spring Valley, USA). The procedure was done according to the manufacturer's manual. 10 µL samples and 100 µL T4-enzyme conjugate solution were gently mixed into each well before one hour incubation at RT. The plate was washed with 300 µL washing buffer per well for 3 times. The substrate solution (100 µL) was added to the wells and the plate was incubated at RT for 15 minutes. 50 µL stop solution was added to each well and the absorbance read at 450 nm.

3.2.3 Histological methods[150]

3.2.3.1 Tissue preparation for paraffin sections

Tissues were isolated from euthanized mice and fixed in 4% PFA/PBS at 4°C overnight. For preparation of bone tissue, most of the muscle and connective tissues were removed and the bone subsequently decalcified in 0.5 M EDTA for 2 weeks. Fixation of bone or fat tissues was further processed according to the following protocol:

Solution	T°C	Fat	Bone
25% EtOH	RT	- -	2.0 h
50% EtOH	RT	- -	2.0 h
75% EtOH	RT	0.5 h	2.0 h/ o.n
95% EtOH	RT	1.5 h	2.0 h
100% EtOH	RT	1.0 h / o.n	2.0 h/ o.n
Xylene	RT	2 × 1.0 h	2.0 h
Xylene	37°C	- -	0.5 h
Xylene	60°C	- -	0.5 h
Xylene / paraffin	60°C	24 h	24 h

Afterwards, the tissues were embedded into paraffin in plastic molds and stored at 4°C. 5 µm sections were cut with a RM2165 microtome (Leica Instruments, Heidelberg, Germany). Deparaffinization was performed by incubation of the slides in 100% xylene for 5 minutes, followed by rehydration through an ethanol series (100%, 95%, 75% and 50% EtOH) for 5 minutes each and a final step in ddH_2O.

3.2.3.2 Hematoxylin and eosin (H&E) staining

After incubation in Mayer's Hematoxylin (Sigma, Steiheim, Germany) for 10 minutes, sections were washed with running tap water and subsequently dipped shortly in 95% ethanol for 10 times. In the following, sections were counterstained with Eosin Y for 20 seconds and dehydrated through an ethanol series (75%, 95%, 100% EtOH) for 3 minutes each. In a final step, stained slides were placed in 100% xylene for 10 minutes for clearance and finally covered with Entellan mounting medium (Merck, Darmstadt, Germany) and a cover slip. Images of H&E staining were captured using a microscope (Axioskop, Carl Zeiss, Göttingen, Germany) equipped with an Axiocam camera (Carl Zeiss, Göttingen, Germany). Image acquisition was performed with Axiovision Software (Carl Zeiss, Göttingen, Germany).

3.2.3.3 Tartrate-resistant acidic phosphatase (TRAP) staining

The dewaxed sections were incubated in TRAP buffer for 10 minutes at RT and subsequently incubated in TRAP staining solution for 2 hours at 37°C. Sections were washed with ddH_2O for 2 minutes before dipping shortly in Mayer's Hematoxylin (Sigma, Germany) for 10 times. Afterwards, sections were briefly washed with tap water and stained with 0.1% Sodiumbicarbonate buffer for 1 minute. Finally, sections were covered with Entellan mounting medium (Merck, Darmstadt, Germany) and a cover slip.

3.2.3.4 Toluidine blue staining

Sections were deparaffinized and incubated in Toluidine blue staining solution for 10 minutes at RT. Afterwards, slides were shortly dipped in 96% EtOH for 2 times and placed in 100% EtOH for 10 minutes. In a final step, slides were placed in 100 Xylene and covered with Entellan mounting medium (Merck, Darmstadt, Germany) and a slip.

3.2.4 Standardized methods used in the German Mouse Clinic (GMC)

3.2.4.1 Dysmorphological screening

In the dysmorphology screen of the GMC, the mice were analyzed for morphological and functional alterations using a 54-parameter protocol with a strong focus on bone phenotypes. Further tests for defects in bone development and homeostasis included X-ray, DEXA, as well as pQCT analysis, and in special cases, micro computed tomography[150-152]. Bone metabolic parameters as total inorganic calcium (Ca), total inorganic phosphate (Pi), total alkaline phosphatase activity (ALP) and bone markers were analyzed in plasma[153].

pQCT analysis was carried out using the Stratec XCT Research SA+ device (Stratec Medizintechnik GmbH, Germany). The mice were performed isoflurane anesthesia and left limb fixed in the holder installed in the scan area. The spatial resolution was set to 70 µm, and the distal femoral metaphysis and diaphysis of the left femur from each mouse was examined to obtain volumetric bone mineral density, content and area of the trabecular, cortical, and total bone. The reference line for the CT scans was set at the most distal point of the femur (knee joint space). At 3.0 mm proximal from the reference line, two slices were taken at 0.20 mm intervals to give characteristic cross sections of the femoral metaphysis. At 6.0 mm proximal from the reference line one slice was taken for characteristic cross sections of the diaphysis.

For micro-CT images, skull samples were stored in 75% EtOH and imaged using a SkyScan 1176 in vivo CT (Bruker micro-CT N.V. Kontich, Belgium) in the 4K-mode with 0.5 mm aluminum filter, frame averaging 1, a rotation step of 0.9° and a resolution of 9 µm/ pixel. Femur and tibia samples were replaced from 75% EtOH to 100% EtOH after overnight incubation. All soft tissues on the bones were removed. The acquisition was subsequently performed with a SkyScan 1172 in vivo CT (Bruker micro-CT N.V. Kontich, Belgium) in the 2K-mode with 0.5 mm aluminum filter, frame averaging of 2, a rotation step of 0.25° and a resolution of 6.63 µm/ pixel. Data reconstruction and visualization was performed using InstaRecon® software (InstaRecon, Inc., IL, USA) and CTVox (Bruker micro-CT N.V. Kontich, Belgium). All specimens were taken and positioned into the holder and fixed with a plastic holder for imaging.

3.2.4.2 Metabolic screening

Imbalance between energy intake and expenditure may cause obesity, diabetes and cardiovascular disease[154]. The metabolic screening focuses on the determination of energy metabolism by indirect calorimetry and body composition measurements[155].

Indirect calorimetry, as the most accurate method to assess energy needs[156], has been characterized in a comprehensive systemic phenotype screen[157]. In total, CO_2 and O_2 sensors detect the difference in CO_2 and O_2 concentrations in air volumes flowing through animal cages. The amount of CO_2/O_2 consumed over a given time period can be calculated with airflow through the cage tested in parallel. The heat production (HP) is calculated from the volume of O_2 and respiratory exchange ratio (RER) using the formula as follows:

$$HP\ [mW] = (4.44 + 1.43 \times RER) \times VO_2\ [ml/h]$$

Body composition was measured once per week from 5 to 16 weeks old mice. Noninvasive NMR Scans were used to measure fat and lean content[158,159].

3.2.4.3 Clinical chemical screening

Blood samples were taken from isoflurane-anesthetized mice by puncturing the retro-orbital sinus with non-heparinized capillaries as described[157] using an Olympus AU400 Chemistry Analyzer (Olympus, Hamburg, Germany). 21 different parameters were tested, including various enzyme activities, plasma concentrations of specific substrates and electrolytes. Moreover, basic hematological parameters were measured using a mouse blood analyzer (ABC-Blutbild-Analyzer, Scil Animal Care Company GmbH, Viernheim, Germany). The number and size of red blood cells, white blood cells and platelets were measured by electrical impedance and hemoglobin by spectrophotometry. Mean corpuscular volume (MCV), mean platelet volume (MPV) and red blood cell distribution width (RDW) are calculated directly from the cell volume measurements. The hematocrit (HCT) is assessed by multiplying the MCV with the red blood cell count. Mean corpuscular hemoglobin (MCH) and mean corpuscular hemoglobin concentrations (MCHC) are calculated according to hemoglobin/ red blood cells count (MCH) and hemoglobin/ hematocrit (MCHC)[160]. All measurements were retested after 14 days to confirm observed deviations.

For an intraperitoneal glucose tolerance test, animals were fasted for 16 to 18 hours overnight. Glucose levels were measured with an Accu-Chek Aviva glucose analyzer from Roche (Roche, Mannheim, Germany). Baseline levels of blood glucose were determined before intraperitoneal injections of 2 g glucose/kg body weight using a 20% glucose solution. After glucose injection, blood was collected from the tail at 15, 30, 60, 90 as well as 120 minutes[157].

3.2.4.4 Expression profiling

White adipose tissue (BAT) and brown adipose tissue (WAT) were selected for profiling analysis. Total RNA was isolated from 8 male mutant mice and 8 wild-type mice at the age of 16 weeks. After total RNA was concentrated, Agilent RNA 600 Pico Kit (Agilent, Germany) was used for RNA integrity number (RIN) value assay performed with the Agilent 2100 Bioanalyzer (Agilent, USA) according to the manufacturer's manual. RNA samples, whose RIN value was around 6.0 to 10.0, can be used for microarray analysis.

MouseRef-8 v2.0 Expression Bead Chip Kit (Illumina, San Diego, USA) was used for expression assay. More than 25,000 sequence-specific oligonucleotides (probes) were immobilized to beads. The total RNA was converted to cDNA, followed by an amplification step to generate labeled cRNA performed using the Ambion TotalPrep^{TM} RNA Amplification Kit (Illumina). The purified cRNA was hybridized to the Streptavidin-Cy3 labeled probes of the beads and detected when the BeadChips were scanned. Mean fluorescence intensities were obtained for each spot with the HiScan System (Illumina, USA)[161]. GenomeStudio (V2011.1) was applied for analyzing gene expression data according to the recent content derived from the NCBI RefSeq database. Nonspecific binding normalization and array metrics were performed to get equal results. Further analysis aim to detect differentially expressed genes was performed with CARMAweb package based on the R software platform[162]. Specifically, a moderated t-statistic was calculated by using the limma package and the false discovery rate (FDR) was calculated according to Benjamini & Hochberg[163]. Gene set enrichment was performed for the Gene Ontology (GO)[164] and the Kyoto Encyclopedia of Genes and Genomes (KEGG)[165] databases by using Fisher's exact test.

3.2.5 Food consumption experiment

Animals were given powdery food (freshly made from pellets) every day. Body weight and the amount of consumed food were recorded every day. Food consumption was measured by subtracting the amount of food left in the food shield and the amount of food spilled around from the initial food weight. After removing feces and wood shavings on the bottom of the food shield, spilled food was collected and weighted.

3.2.6 Statistical analyses

Indicated numbers (n) of each animal group determined the mean values, standard deviations (SD) and standard error of the mean (SEM) in the individual experiment. Statistical comparisons between multiple groups were performed using one-way analysis of variance (ANOVA). Comparisons between two groups were made by Student's t-test. Generalized Linear Model was applied with sex, genotype and body mass as factors to account for the effect of body mass in metabolic screening. Excel, StatView software (SAS cooperation) as well as SigmaStat (Jandel Scientific) were used for the different tests. A p-value below 0.05 was considered to be statistically significant. The following significance-ranking was used: * = $p \leq 0.05$, ** = $p \leq 0.01$, *** = $p \leq 0.001$.

4. Results

4.1 Metabolic phenotypes are found in the BAP002 mouse line

4.1.1 A dominant mutation of *Satb2* is identified in the BAP002 mouse line

As the most important technology to identify genetic variants in individuals[166], whole exome sequencing analysis was used to identify the causal mutation in the BAP002 mouse line. This was done in collaboration with Dr. Bettina Lorenz-Depiereux (Institute of Human Genetics, Helmholtz Zentrum München). According to alignment reading results, a total of 9.8 Gb and 9.2 Gb of mapped sequence data correspond to an average 119x and 113x coverage for the mutant and wild-type, respectively. Over 30,000 coding sequences variants were detected in both mutant and wild type. After filtering variants, which also appear in the wild-type and 120 other animals stored in our in-house database, thirty-nine candidates were identified in the mutant mice (Table 1). To further confirm the mutation, the exome sequencing analysis was repeated in additional mice bred in further generations and 12 genes were located in the analysis (Table 2). *Satb2* was the only candidate gene, which was identified in both analyses.

Table 1. Candidate genes list of BAP002 mouse line identified in the first whole exome sequencing analysis.

Location	Gene symbol	Class	Function	SNV quality
chr1:56948007-56948007	Satb2	snp	missense	228
chr1:90111698-90111698	Ugt1a	snp	missense	76
chr10:20041850-20041850	Bclaf1	snp	missense	102
chr10:20041870-20041870	Bclaf1	snp	missense	105
chr11:76859282-76859282	Ccdc55	snp	missense	33
chr11:76859285-76859285	Ccdc55	snp	missense	68
chr11:97032835-97032835	Kpnb1	snp	splice	20
chr12:60172806-60172806	Pnn	snp	missense	28
chr12:66253804-66253804	C79407	snp	missense,5utr,3utr	216
chr14:27249295-27249295	Slmap	snp	missense	20
chr15:82448740-82448740	Cyp2d34	snp	missense	228
chr15:94156372-94156372	Adamts20	snp	missense	228
chr15:100533989-100533989	AK028111 Galnt6	snp	missense,noncoding	228
chr15:103393829-103393829	Glycam1	snp	missense	228
chr18:7926110-7926112	Wac	indel	indel	203
chr18:63269567-63269567	Fam38b	snp	missense	228
chr2:4556715-4556715	Prpf18	snp	missense	20
chr2:103407523-103407523	Abtb2	snp	missense	228
chr2:120126161-120126161	Pla2g4f	snp	missense	228
chr3:93024380-93024380	Flg2	snp	missense	228
chr3:137810338-137810338	Rg9mtd2	indel	splice	37
chr4:11126579-11126579	Ccne2 Ints8	snp	splice,3utr	56
chr4:11490569-11490569	Rad54b E130016E03Rik	indel	frameshift,noncoding	25
chr4:86459382-86459382	Dennd4c	snp	missense	24
chr5:35241546-35241546	Htt	snp	missense	183
chr6:24117965-24117965	Slc13a1	snp	splice	204
chr6:146944973-146944973	Ppfibp1	snp	missense	24
chr7:107983925-107983925	Fam168a	snp	missense	228
chr8:94328716-94328716	BC100534	indel	frameshift	289
chr8:107609287-107609287	Ces3b	snp	nonsense	228
chr9:38563506-38563506	Olfr920	snp	missense	228
chr9:44439587-44439589	Ddx6	indel	indel	158
chr9:53146088-53146088	Exph5	snp	missense	21
chr9:106472958-106472961	Iqcf4	indel	frameshift	636
chrX:81170305-81170305	Dmd	snp	missense	23
chrX:146999624-146999624	Alas2	snp	missense	255

SNV: single nucleotide variants

Table 2. Candidate genes list of BAP002 mouse line identified in the second whole exome sequencing analysis.

Location	Gene symbol	Class	Function	SNV quality
chr1:56948007-56948007	Satb2	snp	missense	228
chr10:24613747-24613748	Med23	indel	frameshift	2165,1328
chr10:93507067-93507069	Fgd6	indel	indel	1620,0163
chr17:88862101-88862115	Foxn2	indel	indel, 5utr	207, 298
chr3:126782758-126782760	AK081244	indel	indel	2217,2293
chr6:130327845-130327847	Klra15, Ly49A, Klar18, Klra1, Klra22, Klra16	indel	indel, nonco	238, 244
chr7: 86839200-86839202	5730590G19Rik	indel	indel, nonco	4338, 4212

Afterwards, Sanger sequencing was performed to confirm the mutation identifying a G to T transversion at cDNA position 700 in exon 6 of the *Satb2* gene on chromosome 1, leading to a valine to leucine exchange at amino acid position 234 (V234L). The mutation was neither found in BAP002 wild-type mice nor in other wild-type mice of our in-house database. None of the other candidate genes were confirmed in mutant BAP002 mice. This mutation is in the first of two highly conserved small ubiquitin-related modifiers (SUMOs) in SATB2 (Figure 5). The BAP002 mutant mouse line was assigned an official gene symbol and designated as *Satb2*^{V234LMhda}.

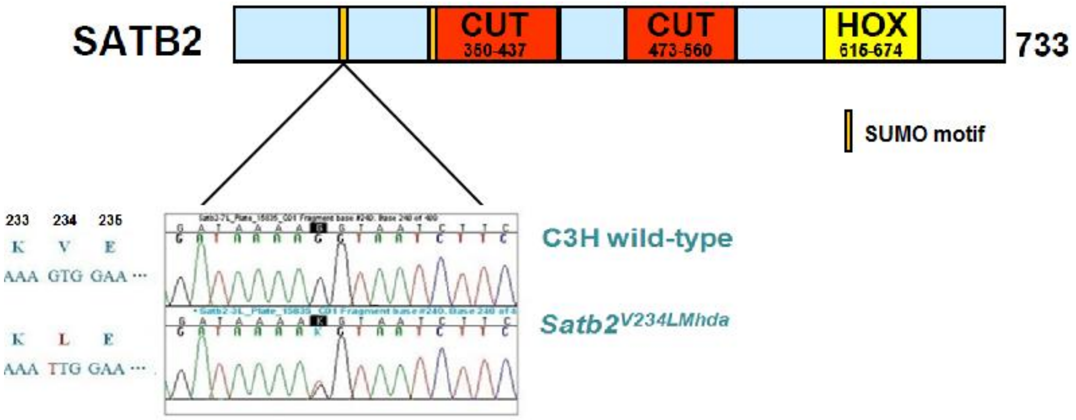

Figure 5. Schematic of SATB2 protein and mutation site in *Satb2*^{V234LMhda} mouse line.

A point mutation was identified in the *Satb2* gene on chromosome 1, leading to a valine to leucine exchange at position 234.

We carried out a Western blot analysis using a specific C-terminal specific antibody to detect SATB2 expression in white and brown adipose tissues of two phenotypes at the age of sixteen weeks. As shown in Figure 6A, two bands were observed in both adipose tissues. However, no pronounced differences expressed between *Satb*$^{V234L/+}$ and *Satb2*^{WT} mice were detected. Similar results were obtained in a Western blot analysis performed using an N-terminus conjugated antibody of SATB2 (data not shown). Interestingly, extra bands smaller than 70 kDa were also observed in an anti-SATB2 antibody image provided by Abcam (Figure 6B). Quantitative RT-PCR was performed on total RNA from white and brown adipose tissues of age-matched animals. No significant differences could be detected between the two groups (Figure 6C).

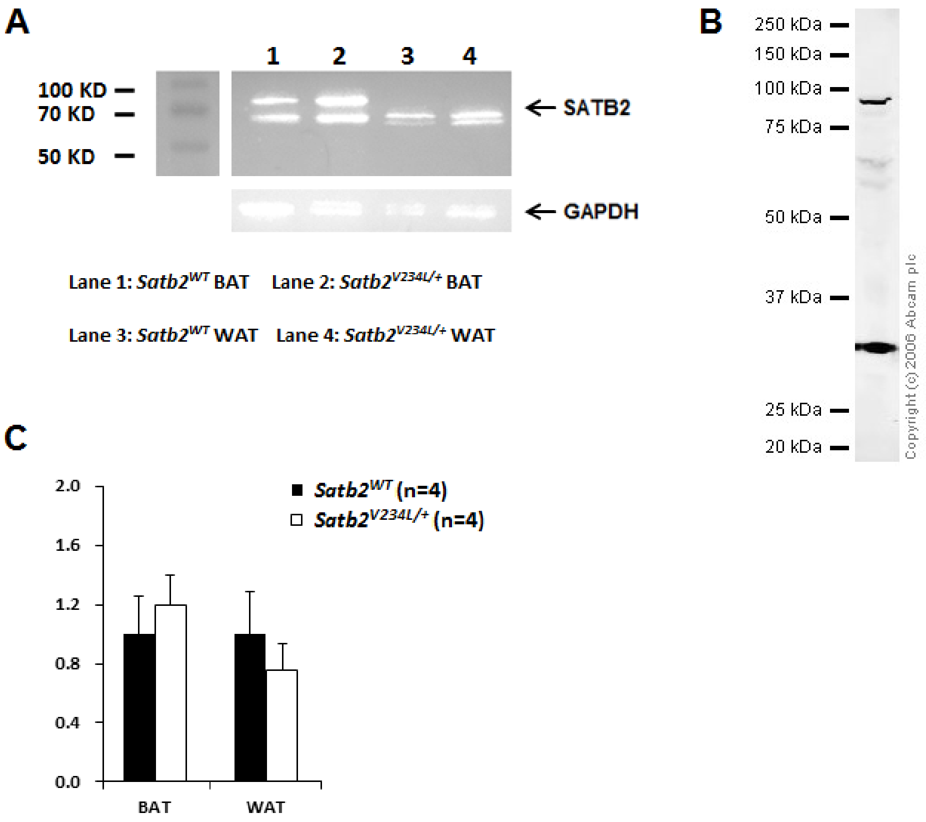

Figure 6. Western blot and RT-PCR analyses in *Satb2*$^{V234L/+}$ and *Satb2*^{WT} littermates at the age of sixteen weeks.

A Western blot analysis of SATB2 protein in brown and white adipose tissues. The predicted size of SATB2 is 83 kDa. GAPDH was used as a standard. **B** Anti-SATB2 antibody image provided by Abcam (http://www.abcam.com/satb2-antibody-ab34735.html). **C** RT-PCR results of total RNA extracted from brown and white adipose tissues of *Satb2*$^{V234L/+}$ and *Satb2*^{WT} mice.

4.1.2 Strong bone phenotypes are observed in *Satb2*$^{V234L/+}$ mice

4.1.2.1 Dysmorphological alterations in *Satb2*$^{V234L/+}$ mice

In preliminary phenotyping, some alterations were found in *Satb2*$^{V234L/+}$ mice such as high total alkaline phosphatase (ALP) blood activities, abnormal tooth enamel and a dysgnathia phenotype. Dual-energy X-ray absorptiometry (DEXA) analyses were performed to give a primary screen of bone densitometry when the mice were nineteen to twenty-one weeks old (Table 3). This was done in collaboration with Dr. Wolfgang Hans (Institute of Experimental Genetics, Helmholtz Zentrum München). In the DEXA analysis, BMD and BMC were strongly reduced in *Satb2*$^{V234L/+}$ mice of both genders, while bone content was significantly decreased only in male mutant mice. Moreover, body length, body weight, fat mass and fat content were decreased in all mutant mice, whereas lean content but not lean mass was increased compared with *Satb2*^{WT} mice.

Table 3. Bone parameters obtained by DEXA measurement at the age of nineteen to twenty-one weeks.

Parameter (19-21 weeks)	Male			Female		
	Satb2^{WT} **(n=9)**	***Satb2***$^{V234L/+}$ **(n=8)**	**P-value**	***Satb2***^{WT} **(n=10)**	***Satb2***$^{V234L/+}$ **(n=9)**	**P-value**
BMD *[mg/cm^2]*	65 ± 1	54 ± 1	≤ 0.001	58 ± 1	51 ± 1	≤ 0.001
BMC *[mg]*	944 ± 68	626 ± 19	≤ 0.001	615 ± 20	494 ± 22	≤ 0.001
Bone Content *[%]*	2.52 ± 0.14	2.02 ± 0.02	≤ 0.01	2.04 ± 0.04	2.00 ± 0.03	n.s.
Body Length *[cm]*	10.67 ± 0.08	10.38 ± 0.08	≤ 0.05	10.40± 0.07	10.06 ± 0.06	≤ 0.01
Body Weight *[g]*	37.16 ± 0.83	30.90 ± 0.84	≤ 0.001	30.04 ± 0.54	24.69 ± 1.21	≤ 0.001
Fat Mass *[g]*	14.68 ± 1.55	5.73 ± 0.55	≤ 0.001	7.45± 0.73	3.64 ± 0.56	≤ 0.001
Fat Content *[%]*	38.97 ± 3.37	18.39 ± 1.52	≤ 0.001	24.54 ± 2.03	14.16 ± 1.70	≤ 0.01
Lean Mass *[g]*	14.40 ± 0.94	17.91 ± 0.53	n.a.	15.69 ± 0.42	14.70 ± 0.58	n.a.
Lean Content *[%]*	39.27 ± 3.29	58.07 ± 1.50	≤ 0.001	52.45 ± 1.93	59.84 ± 1.02	≤ 0.01

Since *Satb2*$^{V234L/+}$ mice displayed strong craniofacial phenotypes, micro-computed tomography (Micro-CT) scans of the skulls were performed with male mice at the age of sixteen weeks. Three-dimensional images showed that incisor teeth were bent, asymmetric and almost totally broken (Figure 7B). An overall view of the cranial bones showed bilateral asymmetric and bent snouts in *Satb2*$^{V234L/+}$ mice (Figure 7D). Two-dimensional images demonstrated a reduced bone density in cranial bones of *Satb2*$^{V234L/+}$ mice compared to *Satb2*^{WT} littermates (Figure 7F).

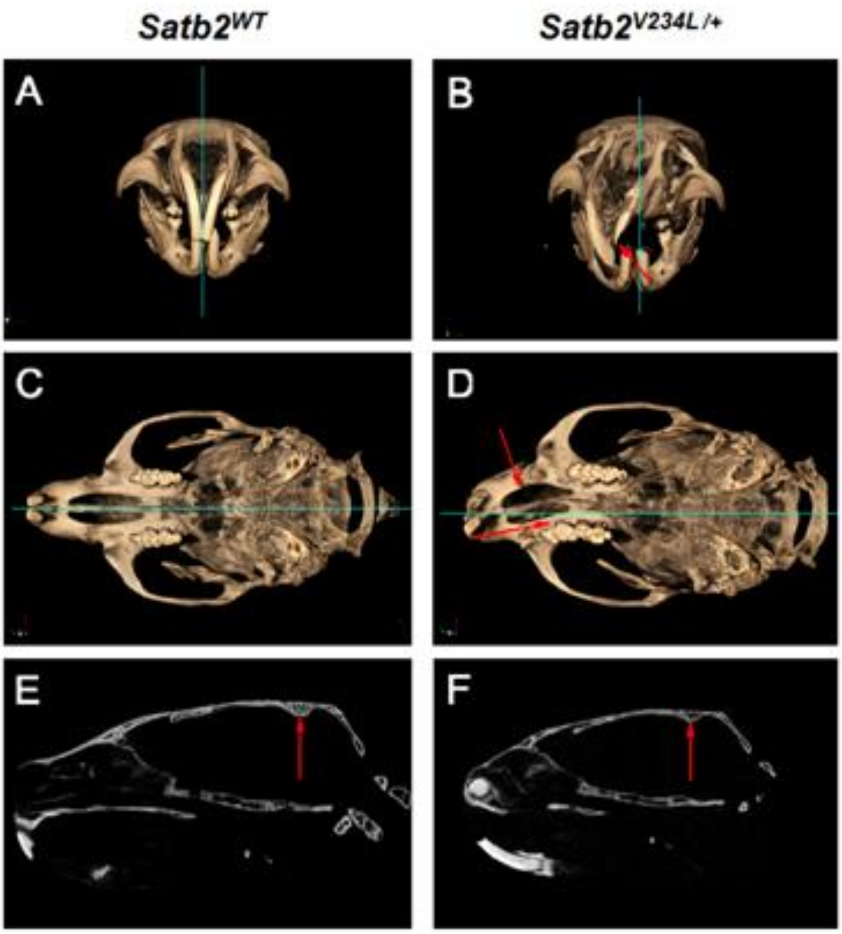

Figure 7. Micro-CT reconstruction images of cranial bones in *Satb2*$^{V234L/+}$ and *Satb2*^{WT} littermates at the age of sixteen weeks.

3D interior views of skulls in *Satb2*^{WT} (A) and *Satb2*$^{V234L/+}$ (B): incisor teeth of mutant mice were shifted and shortened. 3D occlusal views of upper jaws in *Satb2*^{WT} (C) and *Satb2*$^{V234L/+}$ (D): *Satb2*$^{V234L/+}$ mice showed bilateral asymmetric and truncated snouts, and upper molar deformities. 2D lateral view of the skulls showed lower bone density in *Satb2*$^{V234L/+}$ (F) compared to *Satb2*^{WT} mice (E). Figure kindly provided by Dr. Christian Cohrs.

To quantify alterations in bone, peripheral quantitative computed tomography (pQCT) analyses were performed in addition. The BAP002 mice were scanned using pQCT at the age of eighteen to nineteen weeks (Table 4), which was collaborated with Dr. Wolfgang Hans (Institute of Experimental Genetics, Helmholtz Zentrum München). Compared with female mice, male *Satb2*$^{V234L/+}$ mice showed stronger phenotypes. Most of the parameters in metaphysis and diaphysis were significantly reduced in male *Satb*$^{V234L/+}$ mice compared to male *Satb2*^{WT} mice. Additionally, significantly changed parameters in female mice were observed in the metaphysis only, even though all other parameters revealed a trend toward decreased values.

Table 4. Femur parameters obtained by pQCT measurement in *Satb2*$^{V234L/+}$ and *Satb2*^{WT} littermates at the age of eighteen to nineteen weeks.

	Parameter (18-19 weeks)	**Male**			**Female**		
		***Satb2*^{WT} (n=10)**	***Satb2*$^{V234L/+}$ (n=10)**	**P-value**	***Satb2*^{WT} (n=10)**	***Satb2*$^{V234L/+}$ (n=10)**	**P-value**
metaphysis	**Total Content** *[mg]*	2.23 ± 0.11	1.82 ± 0.16	≤ 0.001	2.49 ± 0.30	1.81 ± 0.12	≤ 0.001
	Total Density *[mg/cm^3]*	632.2 ± 36.9	615.6 ± 27.7	≤ 0.05	771.1 ± 45.5	704.0 ± 43.4	≤ 0.01
	Total Area *[mm^2]*	3.41 ± 0.12	2.95 ± 0.12	≤ 0.001	3.23 ± 0.36	2.57 ± 0.14	≤ 0.001
	Cortical Content *[mg]*	1.87 ± 0.12	1.53 ± 0.14	≤ 0.001	2.30 ± 0.29	1.61 ± 0.11	≤ 0.001
	Cortical Density *[mg/cm^3]*	830.0 ± 12.4	841.6 ± 20.6	n.s.	897.7 ± 31.4	899.0 ± 32.0	n.s.
	Cortical Area *[mm^2]*	2.26 ± 0.17	1.82 ± 0.19	≤ 0.001	2.57 ± 0.36	1.80 ± 0.13	≤ 0.001
	Trabecular Content *[mg]*	0.35 ± 0.33	0.28 ± 0.04	≤ 0.001	0.19 ± 0.05	0.09 ± 0.03	n.s.
	Trabecular Density *[mg/cm^3]*	308.1 ± 19.8	252.3 ± 30.7	≤ 0.001	294.0 ± 40.2	253.3 ± 38.5	n.s.
	Trabecular Area *[mm^2]*	1.15 ± 0.14	1.13 ± 0.12	n.s.	0.66 ± 0.19	0.78 ± 0.11	n.s.
diaphysis	**Total Content** *[mg]*	1.99 ± 0.09	1.80 ± 0.09	≤ 0.001	1.95 ± 0.14	1.58 ± 0.08	n.s.
	Total Density *[mg/cm^3]*	992.0 ± 26.4	1010.8 ± 34.3	n.s.	1054.2 ± 20.6	1031.8 ± 30.7	n.s.

Total Area *[mm^2]*	2.01 ± 0.07	1.79 ± 0.11	≤ 0.001	1.85 ± 0.15	1.56 ± 0.04	n.s.
Cortical Content *[mg]*	1.93 ± 0.09	1.76 ± 0.08	≤ 0.001	1.90 ± 0.14	1.55 ± 0.08	n.s.
Cortical Density *[mg/cm^3]*	1128.6 ± 10.4	1126.2 ± 14.7	n.s.	1163.8 ± 12.8	1125.0 ± 18.1	n.s.
Cortical Area *[mm^2]*	1.71 ± 0.07	1.56 ± 0.07	≤ 0.001	1.64 ± 0.12	1.37 ± 0.05	n.s.
Trabecular Content *[mg]*	0.06 ± 0.01	0.05 ± 0.01	≤ 0.05	0.05 ± 0.01	0.04 ± 0.01	n.s.
Trabecular Density *[mg/cm^3]*	212.7 ± 22.4	207.0 ± 14.4	n.s.	216.5 ± 9.5	206.4 ± 16.7	n.s.
Trabecular Area *[mm^2]*	0.30 ± 0.04	0.23 ± 0.05	≤ 0.05	0.22 ± 0.03	0.19 ± 0.03	n.s.

Taken together, abnormal teeth phenotypes, strong craniofacial malformations and impaired bone metabolism were expressed in *Satb2*$^{V234L/+}$ mice.

4.1.2.2 Clinical chemical abnormalities in *Satb2*$^{V234L/+}$ mice

Clinical chemical parameters were measured in plasma to analyze possible changes in metabolic pathways[167]. This part of work was done in collaboration with Dr. Birgit Rathkolb (Institute of Experimental Genetics, Helmholtz Zentrum München). Parameters showing significant changes in two repeated clinical chemical measurements are shown in Table 5. Significantly decreased cholesterol, ferritin, transferrin and iron concentrations as well as α-amylase activities were observed in *Satb2*$^{V234L/+}$ mice, while the ALP activities were significantly increased in *Satb2*$^{V234L/+}$ mice compared to *Satb2*^{WT} mice. Some of these parameters are reported being more or less connected with bone formation[168,169]. The differences were slightly stronger in male *Satb2*$^{V234L/+}$ mice (Table 5).

Table 5. Significantly changed parameters obtained by clinical chemical measurement in *Satb2*$^{V234L/+}$ and *Satb2*^{WT} littermates at the age of fourteen weeks.

Parameter	Male			Female		
	Satb2^{WT} (n=10)	*Satb2*$^{V234L/+}$ (n=10)	P-value	*Satb2*^{WT} (n=10)	*Satb2*$^{V234L/+}$ (n=10)	P-value
Cholesterol *[mg/dL]*	175.0 ± 5.13	147.4 ± 3.30	≤ 0.001	121.1 ± 5.46	111.8 ± 5.55	n.s.
α-Amylase *[U/L]*	616 ± 10.4	579 ± 9.4	≤ 0.05	536 ± 12.6	499 ± 17.7	n.s.
ALP *[U/L]*	96.2 ± 2.57	113.8 ± 3.39	≤ 0.001	141.0 ± 5.54	165.6 ± 3.62	≤ 0.01
Ferritin *[ng/mL]*	27.0 ± 1.03	26.6 ± 1.86	n.s.	45.0 ± 2.88	32.6 ± 1.43	≤ 0.01
Transferrin *[mg/dL]*	139.0 ± 1.81	130.9 ± 1.26	≤ 0.01	138.7 ± 1.29	133.5 ± 1.75	≤ 0.05
Iron *[µg/dL]*	205.9 ± 3.75	188.7 ± 5.34	≤ 0.05	200.6 ± 4.76	194.0 ± 11.67	n.s.

Moreover, ALP activities were compared at different time points (twelve, twenty-four, thirty-six and fifty-two weeks). Significantly increased ALP activities were observed in *Satb2*$^{V234L/+}$ mice when compared to *Satb2*^{WT} mice at different ages. The differences became less obvious along the age as shown in Figure 8.

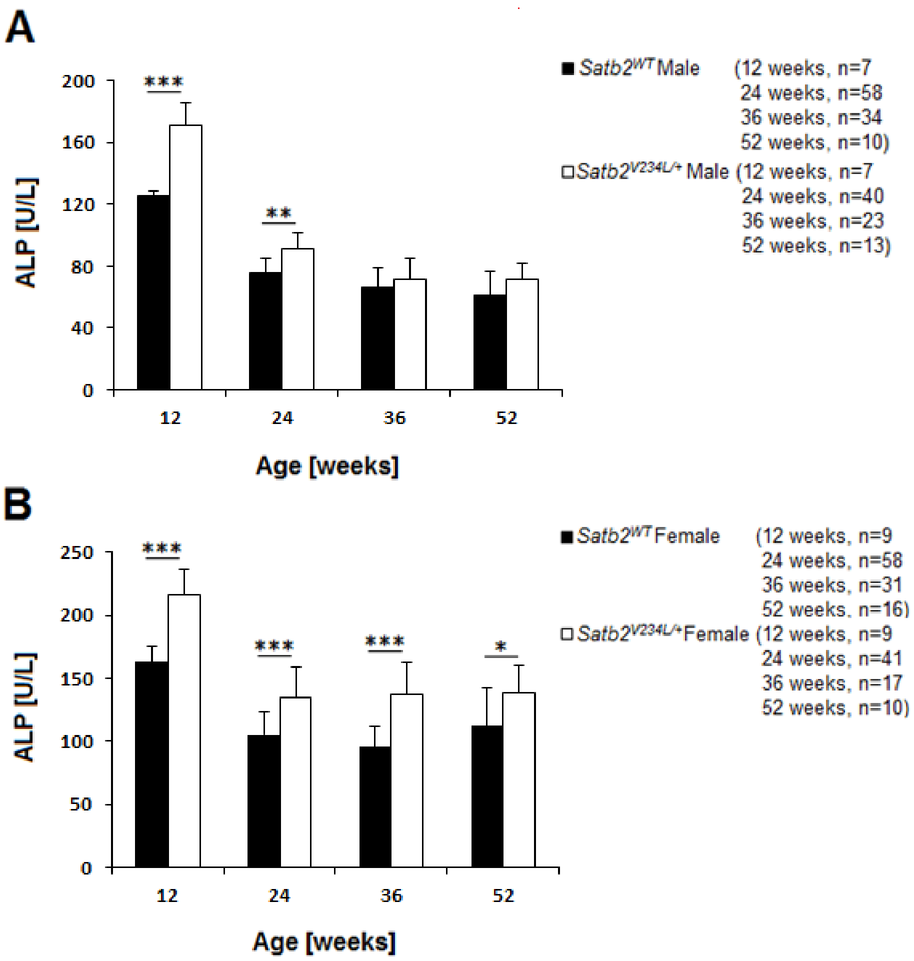

Figure 8. ALP activities in *Satb2*$^{V234L/+}$ and *Satb2*^{WT} mice measured at four different time points.

ALP activities were significantly increased in male (A) and female (B) *Satb2*$^{V234L/+}$ mice when measured at four different ages. Female *Satb2*$^{V234L/+}$ mice depicted 216 ± 19 U/l ($p \le 0.001$), 135 ± 22 U/l ($p \le 0.001$), 137 ± 24 U/l ($p \le 0.001$) and 139 ± 21 ($p \le 0.05$) U/l when measured at an age of twelve, twenty-four, thirty-six and fifty-two weeks (vs 163 ± 13 U/l, 105 ±18 U/l, 96 ± 16 U/l and 112 ± 31 U/l in *Satb2*^{WT} mice). At the same ages in male *Satb2*$^{V234L/+}$ mice 171 ± 14 U/l ($p \le 0.001$), 91 ± 11 U/l ($p \le 0.01$), 72 ± 13 (not significant) and 72 ± 10 U/l (not significant) were measured, compared to male *Satb2*^{WT} mice showing 125 ± 4 U/l, 76 ± 9 U/l, 66 ± 13 U/l and 61 ± 16 U/l. *: $p \le 0.05$, **: $p \le 0.01$, ***: $p \le 0.001$.

Although some parameters obtained in hematological analysis revealed significant differences between *Satb2*$^{V234L/+}$ and *Satb2*^{WT} mice at the age of fourteen weeks, these changes could be not confirmed when the same cohort was measured two weeks later (data not shown).

4.1.2.3 Histological abnormalities of bone in *Satb2*$^{V234L/+}$ mice

Microscopical analyses were performed with long bones (femur and tibia) taken from sixteen weeks old BAP002 mice. H&E stained long bones showed disordered areas in cortical bone matrix. These areas were more present in *Satb2*$^{V234L/+}$ mice (Figure 9B) than in *Satb2*^{WT} mice (Figure 9A) and could be a hint to increased bone remodeling[170]. Furthermore, an abnormal haphazard organization of the collagen fibers was observed in *Satb2*$^{V234L/+}$ mice (Figure 9B). In contrast, the cortical bone in *Satb2*^{WT} mice showed as a regular parallel alignment of collagen into sheets. The number of osteoblasts was decreased in *Satb2*$^{V234L/+}$ mice (Figure 9C, 9D and 9G). Strikingly, as a new phenotype not described in *Satb2*$^{-/-}$ mice[124], more TRAP-positive osteoclasts were observed in *Satb2*$^{V234L/+}$ mice than in *Satb2*^{WT}mice (Figure 9E, 9F and 9H). Differences of metaphyseal bone cells were statistically significant (t-test and Wilcoxon-Mann-Whitney-Test, $p \leq 0.05$). This part of work was done in collaboration with Dr. Julia Calzada-Wack (Institute of Pathology, Helmholtz Zentrum München).

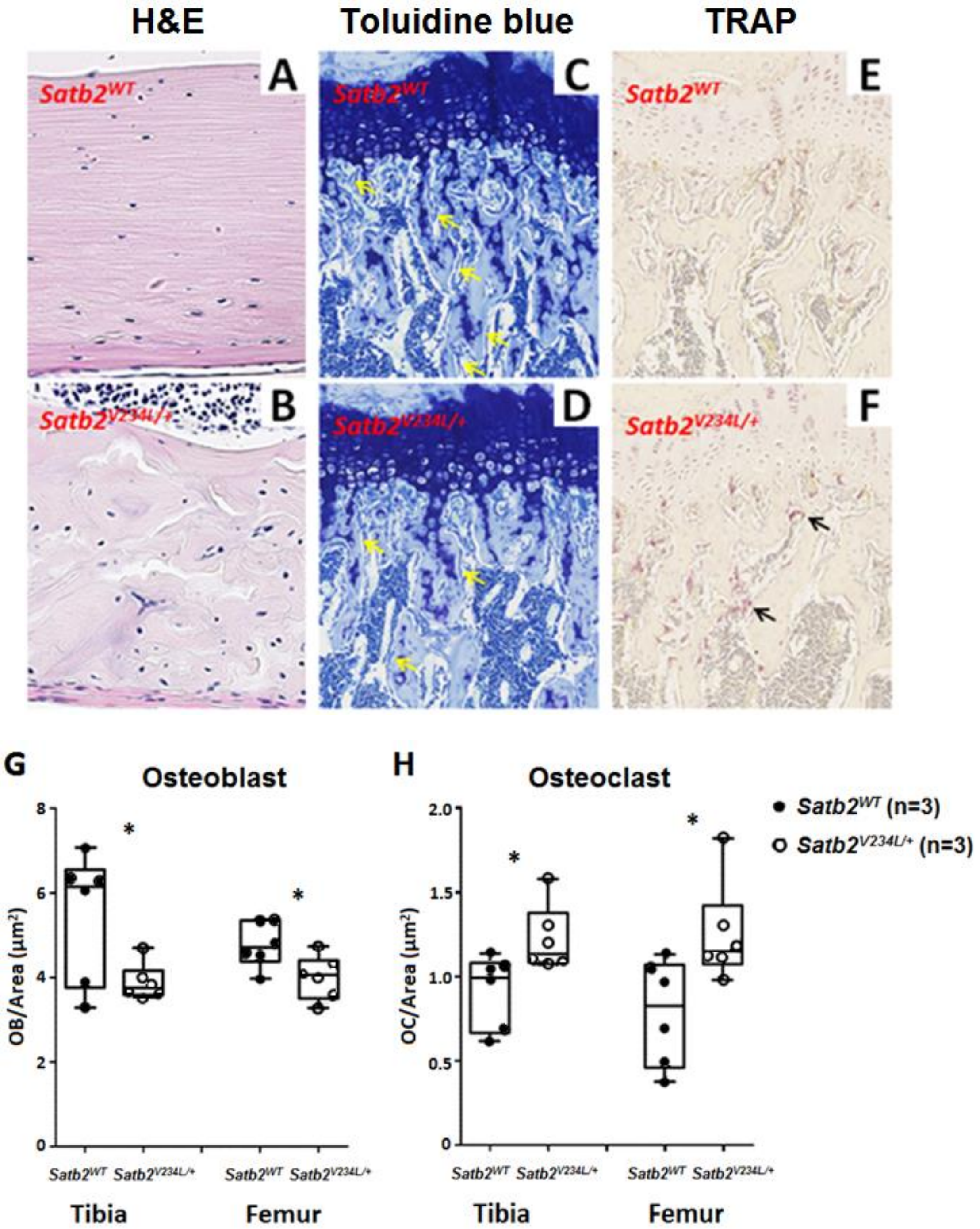

Figure 9. Histological analyses of long bone in sixteen weeks old *Satb2*$^{V234L/+}$ and *Satb2*^{WT} mice.

A and B H&E staining of medial longitudinal sections through the femur of *Satb2*^{WT} (A) and *Satb2*$^{V234L/+}$ (B) mice (20×). **C and D** Toluidine blue stained osteoblasts (yellow arrows) in the proximal tibia of *Satb2*^{WT} (C) and *Satb2*$^{V234L/+}$ (B) littermates (10×). **E and F** TRAP stained osteoclasts (black arrows) in the proximal tibia of *Satb2*^{WT} (E) and *Satb2*$^{V234L/+}$ (F) mice (10×). **G and H** Histomorphometric quantification of osteoblast amount relative to trabecular area (G) and osteoclast amount relative to trabecular area (H) of sixteen weeks mice. *: $p \leq 0.05$.

4.1.2.4 Alterations of bone formation markers in *Satb2*$^{V234L/+}$ mice

Osteoblast and osteoclast numbers were observed being significantly different between *Satb2*$^{V234L/+}$ and *Satb2*^{WT}mice in histological analysis. To give further support to prove an impaired bone turnover, circulating plasma osteocalcin (OC) and CTX-1 values were measured, which are specific markers of osteoblasts and osteoclasts, respectively[171,172]. Plasma osteocalcin was measured in male mice only (n=10). *Satb2*$^{V234L/+}$ mice exhibited significantly decreased OC levels (Figure 10A), which were in line with decreased osteoblast numbers in *Satb2*$^{V234L/+}$ mice.

When CTX-1 values were measured in twenty-four weeks old mice, no significant differences were observed between *Satb2*$^{V234L/+}$ and *Satb2*^{WT} mice of both sexes (Figure 10B), while eight months old female *Satb2*$^{V234L/+}$ mice showed a significant increase. In age-matched male *Satb2*$^{V234L/+}$ mice, only a tendency to increased CTX-1 values was observed, however, not reaching statistical significance (Figure 10C).

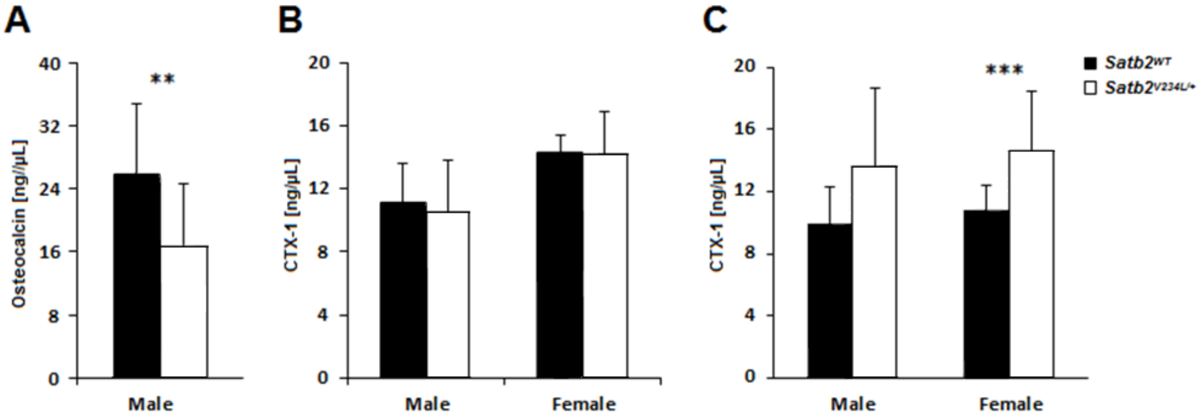

Figure 10. Osteocalcin and CTX-1 values in *Satb2*$^{V234L/+}$ and *Satb2*^{WT} mice.

A Plasma osteocalcin was significantly decreased in male *Satb2*$^{V234L/+}$ mice at the age of sixteen weeks (n=10). **B** Plasma CTX-1 values showed no differences between *Satb2*$^{V234L/+}$ and *Satb2*^{WT} mice at the age of twenty-four weeks (n=10). **C** When the mice were eight months old, female *Satb2*$^{V234L/+}$ mice (n=7) showed significantly higher CTX-1 values than *Satb2*^{WT} mice (n=9). Male *Satb2*$^{V234L/+}$ mice (n=9) exhibited a tendency to increased CTX-1 values when compared to *Satb2*^{WT} mice (n=10), but this was not significant. **: $p \leq 0.01$, ***: $p \leq 0.001$.

4.1.3 Strong metabolic phenotypes are observed in *Satb2*$^{V234L/+}$ mice

4.1.3.1 Altered metabolic rate in *Satb2*$^{V234L/+}$ mice

Our previous measurements of nineteen to twenty weeks old mice showed that *Satb2*$^{V234L/+}$ mice had a reduced body mass, accumulated less fat mass, but more lean mass than *Satb2*^{WT} mice. However, the role of SATB2 in energy metabolism is still unclear and has not been analyzed so far.

Therefore, nuclear magnetic resonance (NMR) measurements were carried out with chow-diet fed BAP002 mice at the age of seven to sixteen weeks (Figure 11). Body composition analysis revealed significantly decreased body weight, fat mass and fat content in *Satb2*$^{V234L/+}$ mice compared to *Satb2*^{WT} mice. Moreover, *Satb2*$^{V234L/+}$ mice showed significantly decreased lean mass compared to *Satb2*^{WT} mice. However, the proportions of lean mass at the age of sixteen weeks were higher in *Satb2*$^{V234L/+}$ mice. Differences of body composition parameters between the genotypes became more obvious along the aging process. No sex-dependent effects were observed in this analysis.

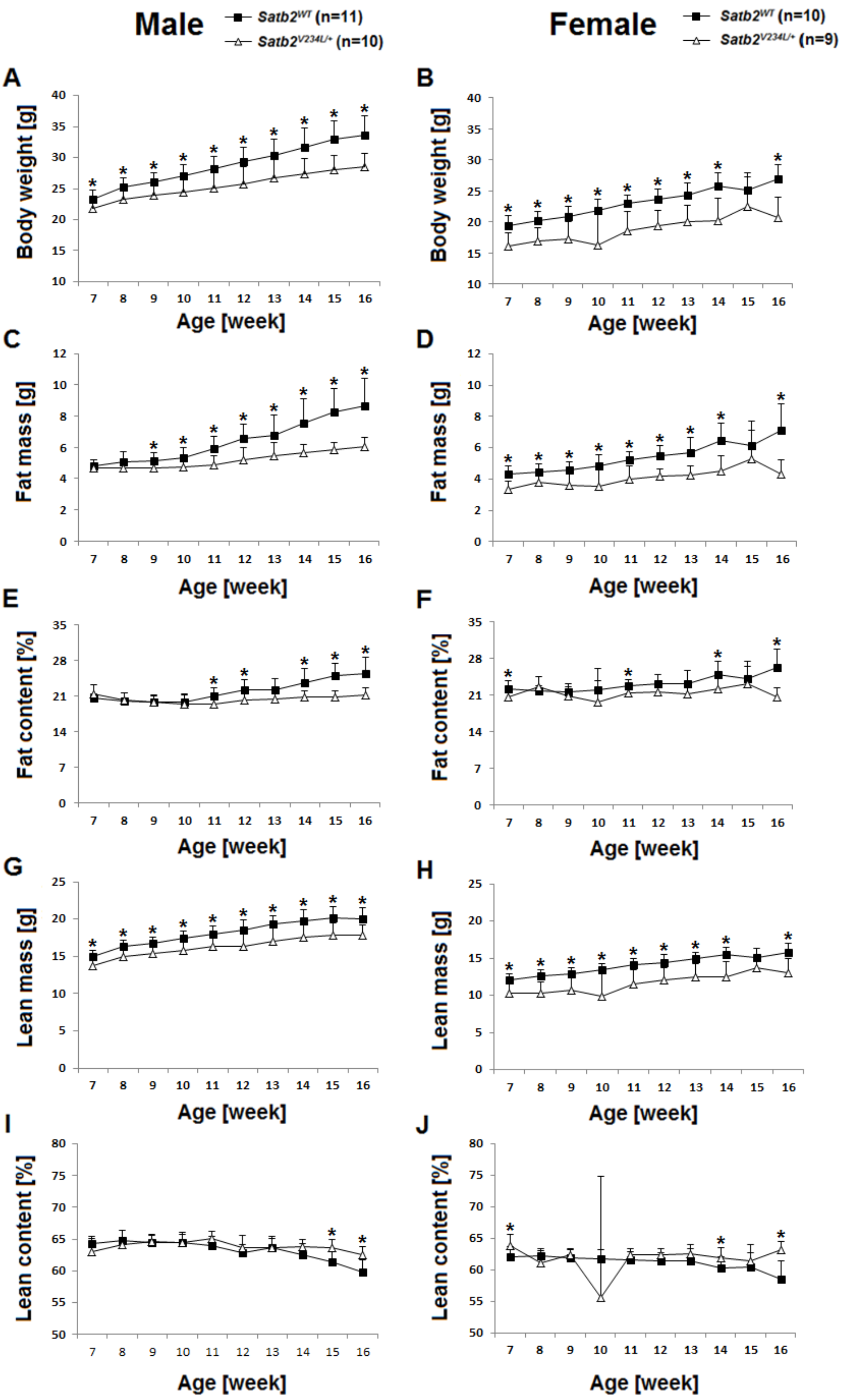

Figure 11. Body composition parameters in *Satb2*$^{V234L/+}$ and *Satb2*^{WT} littermates at the age of seven to sixteen weeks.

A and B Body weight of *Satb2*^{WT} and *Satb2*$^{V234L/+}$ mice. **C and D** Fat mass of *Satb2*^{WT} and *Satb2*$^{V234L/+}$ mice. **E and F** Body fat content of *Satb2*^{WT} and *Satb2*$^{V234L/+}$ mice. **G and H** Lean mass of *Satb2*^{WT} and *Satb2*$^{V234L/+}$ mice. **I and J** Body lean content of *Satb2*^{WT} and *Satb2*$^{V234L/+}$ mice. *: $p \leq 0.05$.

Since body composition phenotypes were most obvious when the mice were sixteen weeks old, linear mixed-effects models were performed to investigate the effects of body weight on fat mass and lean mass. After body weight normalization, *Satb2*$^{V234L/+}$ mice exhibited lower fat mass than *Satb2*^{WT} mice in both genders. Furthermore, female mice had more fat than male mice, but this was observed only in *Satb2*^{WT} and not in *Satb2*$^{V234L/+}$ mice (Figure 12A). However, no significant effect on lean mass was observed between genotypes or genders (Figure 12B).

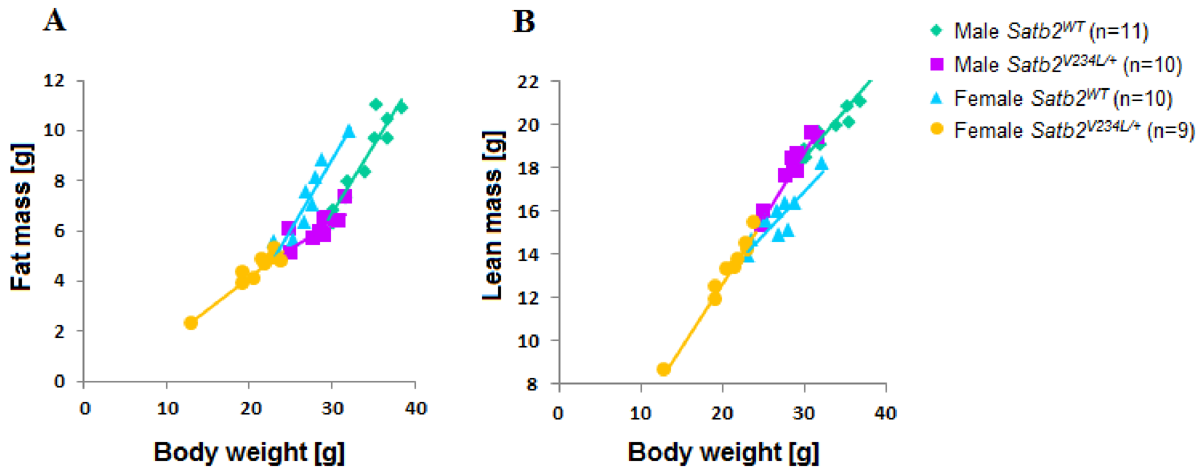

Figure 12. Body weight normalized to fat mass (A) and lean mass (B) in *Satb2*$^{V234L/+}$ and *Satb2*^{WT} mice at the age of sixteen weeks.

To investigate whether these body composition alterations in *Satb2*$^{V234L/+}$ mice are primarily caused or secondarily induced by the abnormal teeth phenotype, a food consumption experiment was performed with six weeks old female BAP002 mice for four weeks. As shown in Figure 13A, body weight differences existed between the two groups of mice from six to ten weeks old even under powdery chow. Body weight of *Satb2*$^{V234L/+}$ mice was significantly lower than *Satb2*^{WT} mice when the experiment started. The significant difference disappeared when powdery food was given for six days and appeared again when the mice were around ten weeks old (Figure 13A). The mean cumulative food intake of mutant and wild-type mice is shown in the Figure 13B. There was no genotype effect on food consumption between the groups. These results suggested that lower body weight and fat mass observed in *Satb2*$^{V234L/+}$ mice were not caused by impaired teeth.

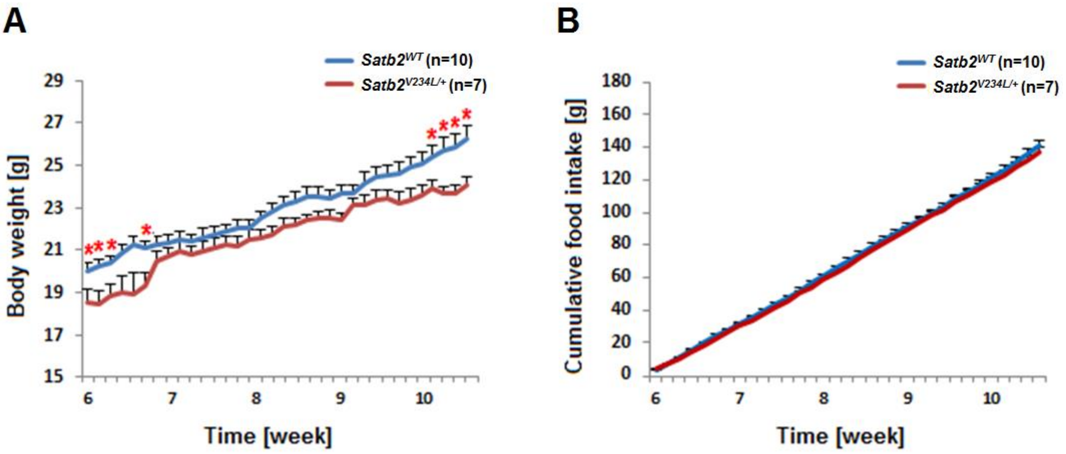

Figure 13. Body weight and cumulative food intake of *Satb2*$^{V234L/+}$ and *Satb2*^{WT} mice at the age of six to ten weeks.

Physical activity and metabolic rate are involved in energy expenditure components. Indirect calorimetry (IC) measurement was performed to test energy expenditure in *Satb2*^{V234L} littermates, which was done in collaboration with Dr. Jan Rozman (Institute of Experimental Genetics, Helmholtz Zentrum München). Locomotor activity was evaluated by recording both horizontal and vertical movements and metabolic rate was assessed by the respiratory exchange ratio (RER), which was calculated as the ratio between carbon dioxide production (VCO_2) and oxygen consumption (VO_2) over a period of 21 hours. The maximum oxygen consumption (max VO_2) is defined as the average oxygen consumption during incremental exercise[173]. The minimum oxygen consumption (min VO_2) is defined as the average oxygen consumption in the resting phase[173]. *Satb2*$^{V234L/+}$ mice showed decreased VO_2 (average VO_2, min VO_2 and max VO_2) when compared with *Satb2*^{WT} mice at the age of ten and sixteen weeks. However, indistinguishable differences were observed in the RER and locomotor activity (distance and rearing) between *Satb2*$^{V234L/+}$ and *Satb2*^{WT} mice in two measurements.

Table 6. Metabolic parameters of *Satb2*$^{V234L/+}$ and *Satb2*^{WT} mice obtained in the first IC measurement at the age of ten weeks.

Parameter	Male			Female		
	***Satb2*^{WT} (n=11)**	***Satb2*$^{V234L/+}$ (n=10)**	**P-value**	***Satb2*^{WT} (n=10)**	***Satb2*$^{V234L/+}$ (n=9)**	**P-value**
Body weight *[g]*	29.41 ± 2.33	25.66 ± 2.81	≤ 0.05	23.57 ±1.74	19.33 ± 2.55	≤ 0.001
Food intake *[g]*	1.76 ± 1.02	1.92 ± 0.78	n.s.	2.41 ± 1.01	1.39 ± 0.98	≤ 0.05
avg VO2 *[ml/h]*	82.23 ± 5.91	81.85 ± 8.86	n.s.	83.06 ± 7.75	65.35 ± 14.18	≤ 0.01
min VO2 *[ml/h]*	56.73 ± 7.13	49.20 ± 7.55	≤ 0.05	58.40 ± 9.94	35.11 ± 13.37	≤ 0.05
max VO2 *[ml/h]*	128.73 ± 18.85	125.70 ± 13.48	n.s.	118.40 ± 11.41	102.00 ± 16.37	≤ 0.05
avg RER	0.84 ± 0.05	0.85 ± 0.04	n.s.	0.87 ± 0.06	0.83 ± 0.06	n.s.
avg Distance *[cm]*	4003 ± 1011	4367 ± 2183	n.s.	3930 ± 703	3545 ± 768	n.s.
avg Rearing *[counts]*	116 ± 22	142 ± 39	n.s.	97 ± 30	126 ± 58	n.s.

Table 7. Metabolic parameters of *Satb2*$^{V234L/+}$ and *Satb2*^{WT} mice obtained in the second IC measurement at the age of sixteen weeks.

Parameter	Male			Female		
	***Satb2*^{WT} (n=11)**	***Satb2*$^{V234L/+}$ (n=10)**	**P-value**	***Satb2*^{WT} (n=8)**	***Satb2*$^{V234L/+}$ (n=8)**	**P-value**
Body weight *[g]*	33.67 ± 3.10	28.54 ± 2.16	≤ 0.001	27.13 ± 2.89	21.65 ± 1.77	≤ 0.001
Food intake *[g]*	2.68 ± 0.98	2.15 ± 0.85	n.s.	2.66 ± 1.21	1.51 ± 1.06	n.s.
avg VO2 *[ml/h]*	89.81 ± 6.06	82.06 ± 8.92	≤ 0.05	91.38 ± 11.42	70.99 ± 14.81	≤ 0.01
min VO2 *[ml/h]*	65.82 ± 7.12	54.20 ± 7.54	≤ 0.05	62.75 ± 8.43	43.13 ± 15.91	≤ 0.05
max VO2 *[ml/h]*	130.45 ± 11.82	122.70 ± 13.15	≤ 0.05	131.63 ± 21.10	110.00 ± 17.30	≤ 0.05
avg RER	0.88 ± 0.05	0.86 ± 0.04	n.s.	0.89 ± 0.08	0.84 ± 0.06	n.s.
avg Distance *[cm]*	5324 ± 2988	7342 ± 7005	n.s.	7264 ± 1689	6731 ± 3573	n.s.
avg Rearing *[counts]*	92 ± 25	115 ± 37	n.s.	168 ± 119	145 ± 117	n.s.

Multiple linear regression models were carried out to estimate the VO_2 by adjusting to genotype, sex, total fat mass and lean mass. Interestingly, we found that *Satb2*$^{V234L/+}$ mice had decreased VO_2 compared to *Satb2*^{WT} mice when the animals were ten weeks old (Figure 14A). In contrast, male *Satb2*$^{V234L/+}$ mice expressed increased VO_2 compared to sex-matched *Satb2*^{WT} mice when the animals were measured at sixteen weeks of age, while no genotype differences were observed in female mice at this age (Figure 14B). These results indicated that only sixteen weeks old male *Satb2*$^{V234L/+}$ mice displayed increased energy expenditure compared to *Satb2*^{WT} mice.

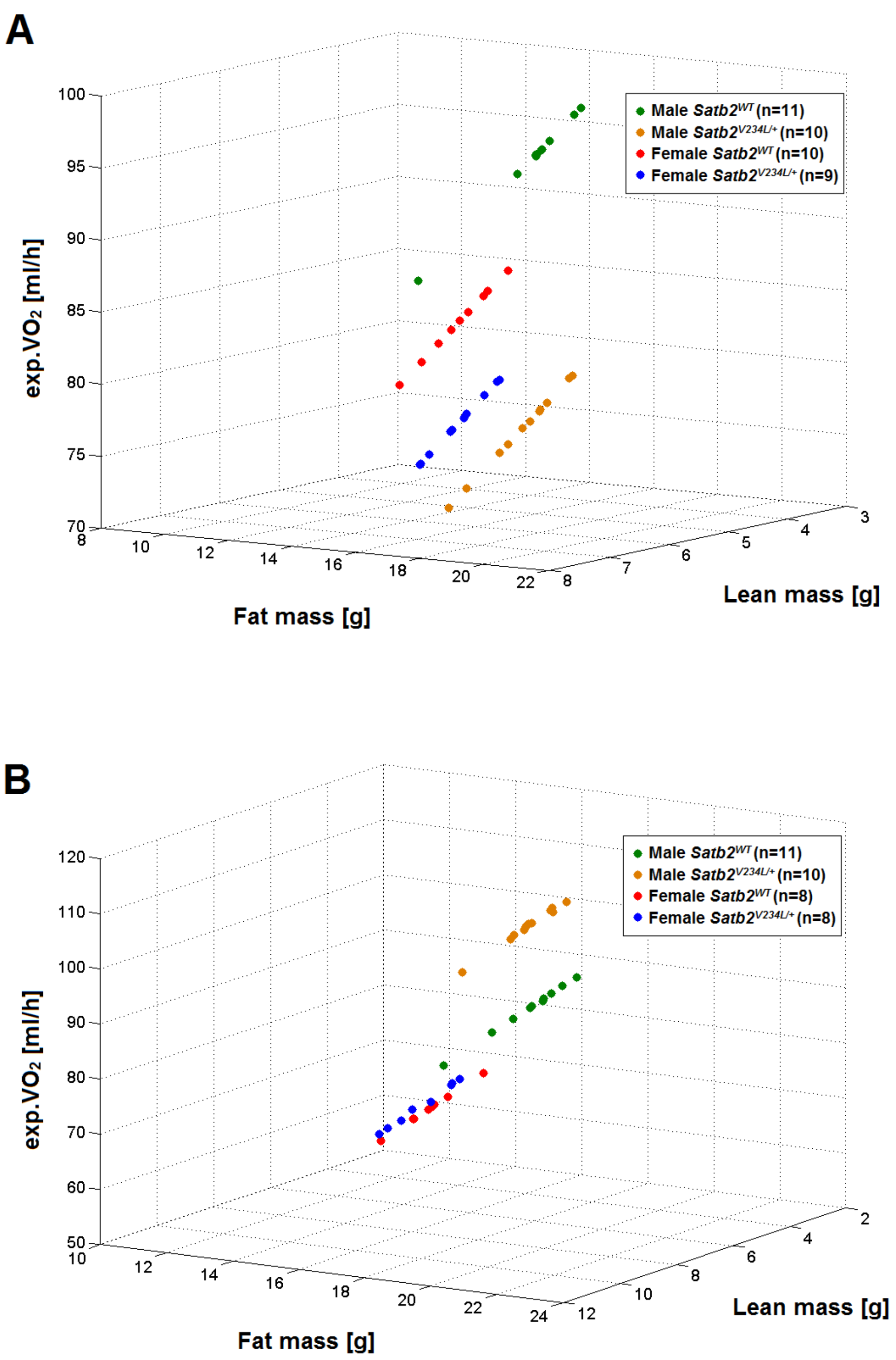

Figure 14. Oxygen expenditure (exp. VO_2) adjusted to fat mass and lean mass in ten and sixteen weeks old *Satb2*$^{V234L/+}$ and *Satb2*^{WT} mice.

A Oxygen consumption normalized to fat mass and lean mass between different groups when the mice were ten weeks old. **B** Oxygen consumption – fat mass and lean mass correlation in *Satb2*^{WT} and *Satb2*$^{V234L/+}$ mice at the age of sixteen weeks.

4.1.3.2 Reduced adiposity and increased browning of adipose tissue observed in *Satb2*$^{V234L/+}$ mice

Increased energy expenditure is considered as the main reason of reduced adiposity[174-176]. Given that strong differences were shown in the body composition parameters and energy expenditure, the effect of the mutation on adipose tissues was investigated in sixteen weeks old *Satb2*$^{V234L/+}$ and *Satb2*^{WT} mice. Epididymal white adipose tissue (eWAT) and brown adipose tissue (BAT) were isolated for morphological analyses. A pronounced browning phenotype expressed in eWAT of *Satb2*$^{V234L/+}$ mice compared to *Satb2*^{WT} mice was found, as judged by multilocular lipid droplets and UCP1 expression (Figure 15A to D)[177]. In comparison to *Satb2*^{WT} mice, *Satb2*$^{V234L/+}$ mice displayed also smaller adipocytes with rich cytoplasmic staining in BAT (Figure 15E and F). H&E staining of eWAT and BAT from younger (three and eight weeks of age) and older (thirty-two weeks of age) animals confirmed this phenotype of *Satb2*$^{V234L/+}$ mice (results not shown). Moreover, the cell-size difference was age-dependently increased corresponding to the observed body-weight difference between the genotypes.

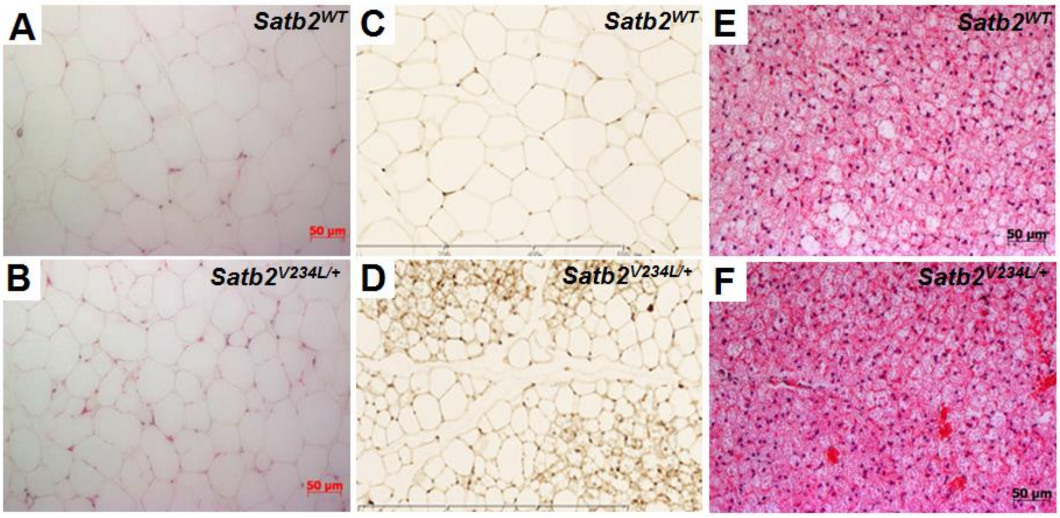

Figure 15. eWAT and BAT histology in sixteen weeks old *Satb2*$^{V234L/+}$ and *Satb2*^{WT} mice.

A and B H&E staining of eWAT from sixteen weeks old animals revealed smaller size of adipocytes and more lipid droplets in *Satb2*$^{V234L/+}$ compared to in *Satb2*^{WT} mice. **C and D** Immunohistochemistry showing that UCP1-positive adipocytes appeared in *Satb2*$^{V234L/+}$ but not in *Satb2*^{WT} mice. **E and F** H&E stained adipocytes in BAT showed increased cytoplasmic staining in *Satb2*$^{V234L/+}$ compared to *Satb2*^{WT} mice.

4.1.3.3 Increased glucose tolerance displayed in *Satb2*$^{V234L/+}$ mice

An intraperitoneal glucose tolerance test (ipGTT) was performed with 16-hour fasted mice at the age of thirteen weeks, which was done in collaboration with Dr. Birgit Rathkolb (Institute of Experimental Genetics, Helmholtz Zentrum München). Blood glucose levels were measured at 0, 15, 30, 60 and 120 minutes after glucose injection. As in wild-type littermates, the glucose levels rose quickly in *Satb2*$^{V234L/+}$ mice, but to a lower extent than in *Satb2*^{WT} mice (Figure 16A and B). In addition, the area under the curve (AUC) was significantly smaller in *Satb2*$^{V234L/+}$ mice compared to *Satb2*^{WT} mice (Figure 16C), indicating an increased glucose tolerance in *Satb2*$^{V234L/+}$ mice.

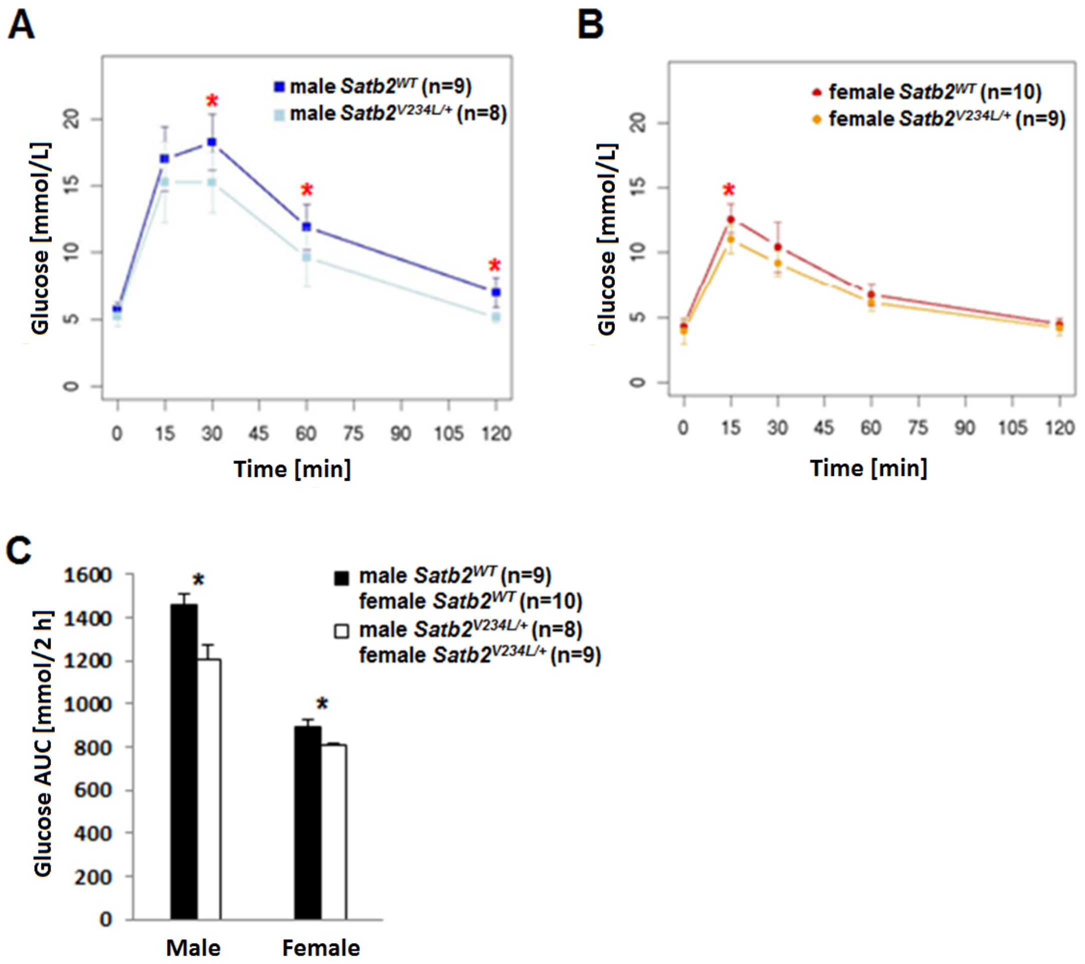

Figure 16. Comparison of intraperitoneal glucose tolerance test (ipGTT) and respective areas under the curve (AUC) in *Satb2*$^{V234L/+}$ and *Satb2*^{WT} mice at the age of thirteen weeks.

Blood glucose levels in male (A) and female (B) *Satb2*$^{V234L/+}$ and *Satb2*^{WT} mice. AUC of each individual ipGTT in 120 minutes was calculated for statistical analysis (C). *: p≤ 0.05.

We next identified determinants of elevated glucose tolerance in *Satb2*$^{V234L/+}$ mice. To follow up this observation, ipGTTs were performed with seventeen weeks old *Satb2*^{V234L} and *Satb2*^{WT} littermates after fasting for six hours. In addition, blood insulin levels were measured at 0, 30 and 120 minutes after glucose injection. On the whole, *Satb2*$^{V234L/+}$ mice expressed a tendency to decreased insulin levels compared to *Satb2*^{WT} mice (Figure 17). The differences between female *Satb2*$^{V234L/+}$ and *Satb2*^{WT} mice were significant when the blood was collected at 30 and 120 minutes. In conclusion, *Satb2*$^{V234L/+}$ mice expressed an increased glucose tolerance as observed in thirteen weeks old mice. In seventeen weeks old *Satb2*$^{V234L/+}$ mice, insulin levels were significantly decreased.

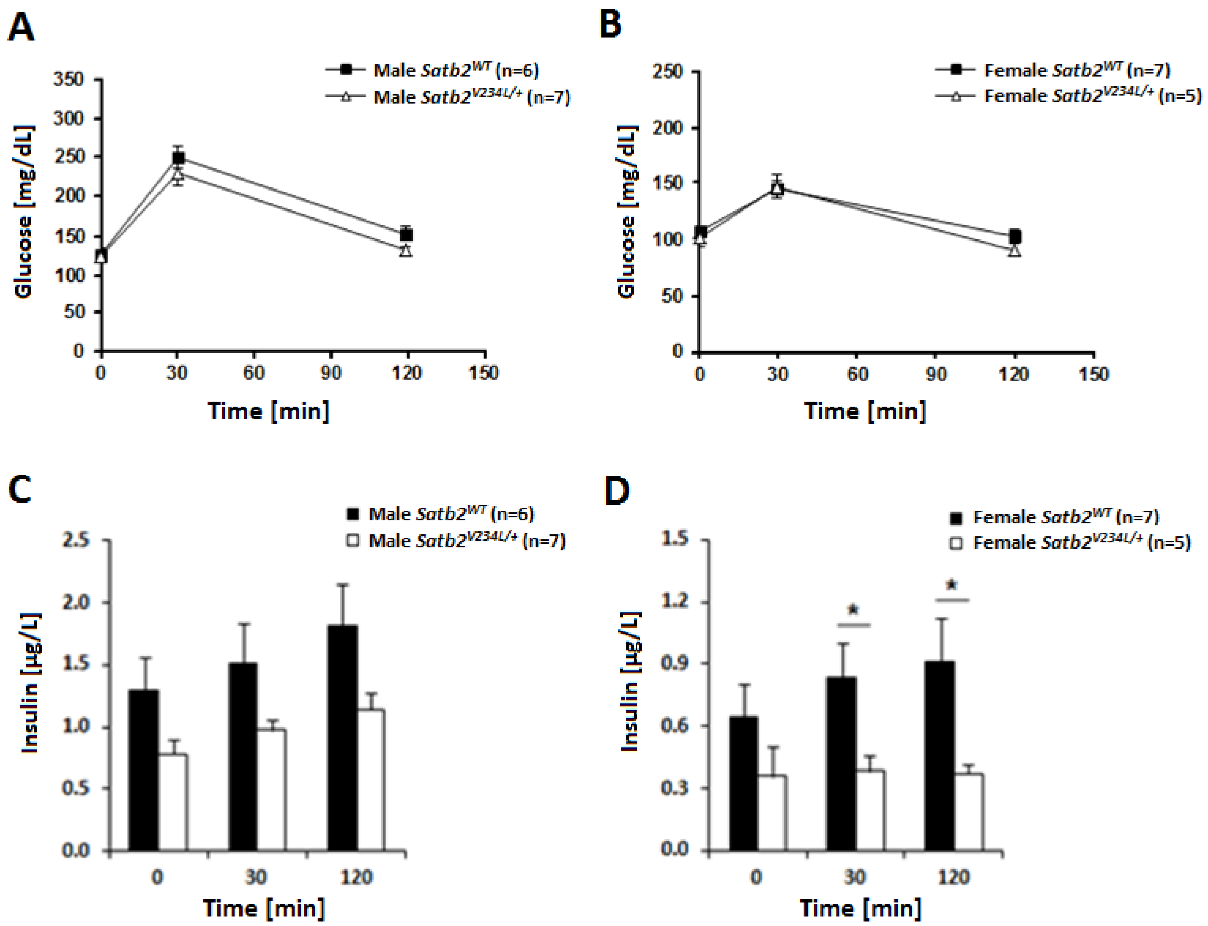

Figure 17. Glucose and insulin concentrations of *Satb2*$^{V234L/+}$ and *Satb2*^{WT} mice following ipGTTs at seventeen weeks of age.

Blood glucose concentration of male (A) and (B) *Satb2*$^{V234L/+}$ and *Satb2*^{WT} mice during ipGTT at time-points 0, 30 and 120 minutes. Insulin concentrations of male (C) and female (D) mice when measured at time-points of 0, 30 and 120 minutes. *: $p \leq 0.05$.

Concomitantly to the ipGTT measurement, concentrations of leptin and adiponectin in plasma were also determined in sixteen weeks old mice after overnight fasting. As important adipose tissue-derived hormones, leptin and adiponectin have been shown to influence glucose homeostasis in rodent and humans[178-181]. However, both genders of *Satb2*$^{V234L/+}$ mice showed a tendency to decreased leptin levels compared to wild-type mice at the age of sixteen weeks (Figure 18A) and no statistically significant differences in adiponectin levels were observed between *Satb2*$^{V234L/+}$ and *Satb2*^{WT} mice of this age (Figure 18B).

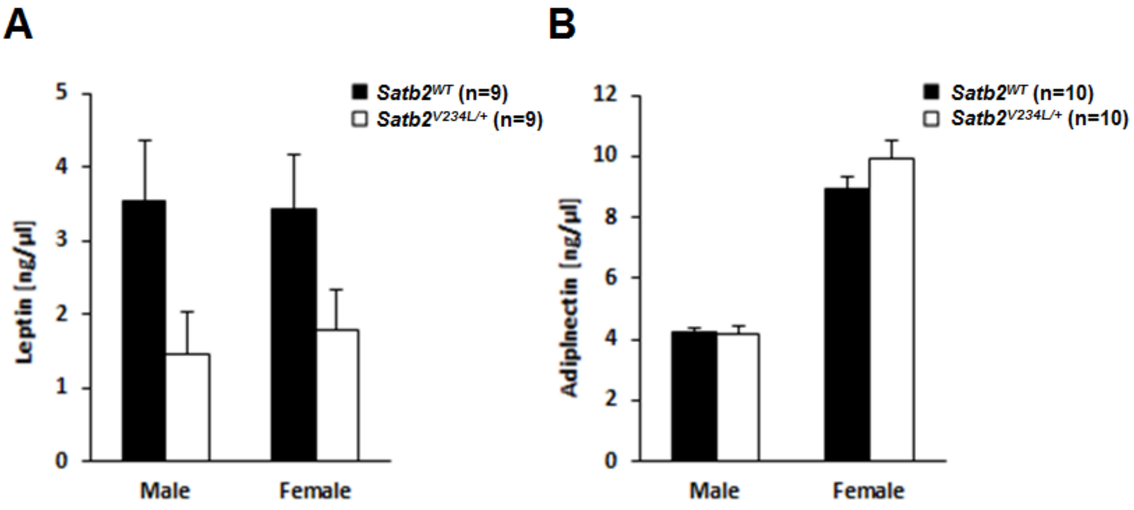

Figure 18. Levels of leptin and adiponectin in plasma of *Satb2*$^{V234L/+}$ and *Satb2*^{WT} mice at the age of sixteen weeks.

Satb2$^{V234L/+}$ mice showed a decreased tendency for plasma leptin levels compared with *Satb2*^{WT} mice (A). No significant difference was expressed in the levels of plasma adiponectin between *Satb2*$^{V234L/+}$ and *Satb2*^{WT} mice (B).

4.1.3.4 Differential eWAT and BAT gene expression between *Satb2*$^{V234L/+}$ and *Satb2*^{WT} mice

The eWAT and BAT gene expression profile was performed with male *Satb2*$^{V234L/+}$ and *Satb2*^{WT} mice. The profiling was done in collaboration with Dr. Marion Horsch (Institute of Experimental Genetics, Helmholtz Zentrum München). Of the 9363 probe sets on the microarray, 364 probe sets in eWAT showed significantly different levels in *Satb2*$^{V234L/+}$ mice when compared with *Satb2*^{WT} mice. We then conducted Principal Component Analysis (PCA) using all probes to characterize the samples from different tissues (eWAT and BAT) and genotypes (*Satb2*$^{V234L/+}$ and *Satb2*^{WT}) (Figue 19). Scatter plots of PC1 and PC2 revealed an obvious difference of gene expression in eWAT between *Satb2*$^{V234L/+}$ and *Satb2*^{WT}. However, no difference was observed in BAT between samples of different genotypes.

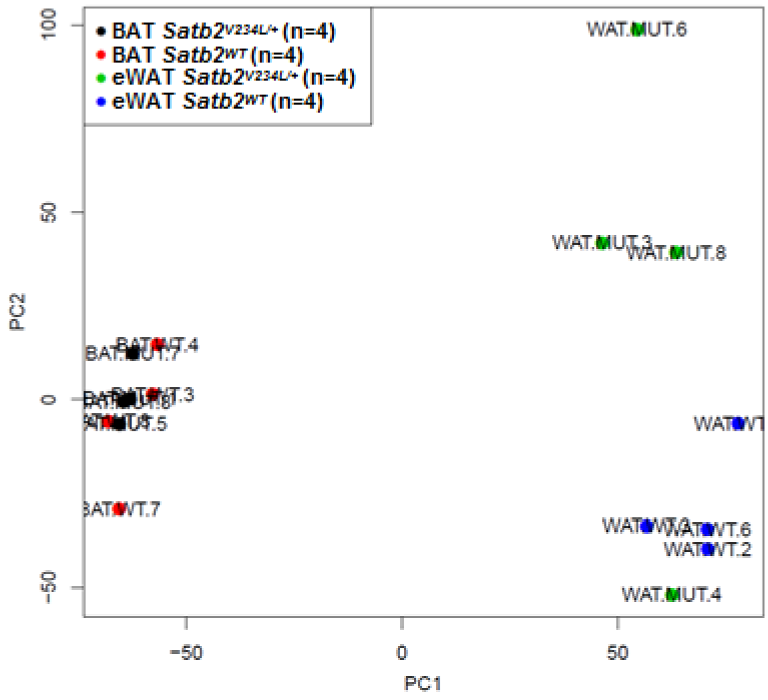

Figure 19. Principal component analysis of microarray results in *Satb*$^{V234L/+}$ and *Satb*^{WT} mice at the age of sixteen weeks.

RNA samples isolated from brown adipose tissue (BAT) and epididymal white adipose tissue (eWAT) of *Satb2*$^{V234L/+}$ and *Satb2*^{WT} were carried out for microarray assay.

To identify functional differences in eWAT between *Satb2*$^{V234L/+}$ and *Satb2*^{WT} mice a KEGG (Kyoto Encyclopedia of Genes and Genomes) pathway analysis was carried out (performed by Steffen Sass, Insitute of Computational Biology, Helmholtz Zentrum München) with 364 significantly regulated genes. The results showed that differentially expressed genes were mainly involved in the pathways shown in Table 8. We noticed that the top-ranked pathways are generally related to metabolic function (e.g., adipocytokine signaling, oxidative phosphorylation).

Table 8. KEGG pathway analysis of differentially expressed genes in eWAT of *Satb2*$^{V234L/+}$ mice compared to *Satb2*^{WT} mice.

KEGG Pathway Term	Count	Genes
Adipocytokine signaling pathway	12	Akt2,Irs2,Jak2,Mapk8,Mapk9,Nfkbia,Pck1,Ppargc1a, Ptpn11,Rxrb,Slc2a4,Stat3
Oxidative phosphorylation	10	Atp5a1,Atp6v1c2,Cox10,Ndufa10,Ndufb9,Ndufv1, Sdhb,Sdhc,Sdhd,Uqcrc2
Citrate cycle (TCA cycle)	5	Mdh1,Pck1,Sdhb,Sdhc,Sdhd
Alzheimer's disease	11	Atp5a1,Bace1,Mapt,Mme,Ndufa10,Ndufb9,Ndufv1, Sdhb,Sdhc,Sdhd,Uqcrc2
Parkinson's disease	9	Atp5a1,Ndufa10,Ndufb9,Ndufv1,Ppid,Sdhb,Sdhc, Sdhd,Uqcrc2
Huntington's disease	11	Atp5a1,Ndufa10,Ndufb9,Ndufv1,Ppargc1a,Ppid,Sdhb, Sdhc,Sdhd,Ucp1,Uqcrc2
Metabolic pathways	35	Agpat3,Agpat6,Atp5a1,Atp6v1c2,Ccbl2,Cox10,Dgat1, Echs1,Fech,G6pd2,Hadh,Hsd11b1,Hyal2,Mdh1,Mlycd, Ndst1,Ndufa10,Ndufb9,Ndufv1,Nmnat1,Ocrl,Pck1,Pgm1, Pi4kb,Pip5k1b,Pisd,Pnmt,Ptges2,Rrm1,Rrm2b,Sdhb, Sdhc,Sdhd,Tkt,Uqcrc2
Insulin signaling pathway	8	Akt2,Irs2,Mapk8,Mapk9,Pck1,Ppargc1a,Ppp1r3c,Slc2a4
Hepatitis C	8	Akt2,Eif2ak2,Mapk8,Mapk9,Nfkbia,Pias4,Psme3,Stat3
Progesterone-mediated oocyte maturation	6	Adcy9,Akt2,Anapc7,Mapk8,Mapk9,Rps6ka1
Fatty acid elongation in mitochondria	2	Echs1,Hadh
Pancreatic cancer	5	Akt2,Brca2,Mapk8,Mapk9,Stat3
Neurotrophin signaling pathway	7	Akt2,Irs2,Mapk8,Mapk9,Nfkbia,Ptpn11,Rps6ka1
Type II diabetes mellitus	4	Irs2,Mapk8,Mapk9,Slc2a4
Homologous recombination	3	Blm,Brca2,Rad50
Ubiquitin mediated proteolysis	7	Anapc7,Cul5,Pias4,Rchy1,Trim32,Ube2q1,Wwp1
Pentose phosphate pathway	3	G6pd2,Pgm1,Tkt
mTOR signaling pathway	4	Akt2,Eif4b,Rictor,Rps6ka1
Valine, leucine and isoleucine biosynthesis	2	Lars2,Vars
NOD-like receptor signaling pathway	4	Mapk8,Mapk9,Nfkbia,Tab3
Glutathione metabolism	4	G6pd2,Oplah,Rrm1,Rrm2b
Non-homologous end-joining	2	Prkdc,Rad50
Inositol phosphate metabolism	4	Ipmk,Ocrl,Pi4kb,Pip5k1b
Proximal tubule bicarbonate reclamation	2	Mdh1,Pck1
Selenocompound metabolism	2	Ccbl2,Txnrd3

Further analysis of the microarray data was performed by Dr. Peter Huypens (Institute of Experimental Genetics, Helmholtz Zentrum München) and based on the protein knowledge database UniProKB (http://www.uniprot.org/). Interestingly, we found that some of the differentially expressed genes are closely associated with insulin sensitivity, adipose tissue browning, mitochondrial function as well as epigenetic and transcriptional regulation.

Therefore, a selection of 9 genes (*Ucp1*, *Cidea*, *Pgc1α*, *Isr2*, *Slc2a4*, *Akt2*, *Ptpn1*, *Mapk8* and *Mapk9*), which are known to be associated with BAT and insulin sensitivity, were chosen to confirm their differential gene expression in eWAT from *Satb2*$^{V234L/+}$ mice by qRT-PCR (Table 9).

Table 9. Candidate genes for qRT-PCR expression analysis in eWAT isolated from *Satb2*$^{V234L/+}$ and *Satb2*^{WT} mice.

Gene symbol	Gene name
Ucp1	Uncoupling protein 1
Cidea	Cell death-inducing DFFA-like effector A
Pgc1α/Ppargc1a	Peroxisome proliferator-activated receptor gamma coactivator 1-alpha
Isr2	Insulin receptor substrate 2
Slc2a4	Solute carrier family2, facilitated glucose transporter member 4
Akt2	Thymoma viral proto-onmcogene 2
Ptpn1	Protein tyrosine phosphatase 1
Mapk8	Mitogen-activated protein kinase 8
Mapk9	Mitogen-activated protein kinase 9

After normalizing the expression levels with the mean value of reference genes (*Cyc1* and *Tbp*), all genes showed the same tendency as in the previous microarray experiments, but only the expression of *Pgc1α* and *Mapk8* was significantly changed in *Satb2*$^{V234L/+}$ mice compared to *Satb2*^{WT} mice (Figure 20).

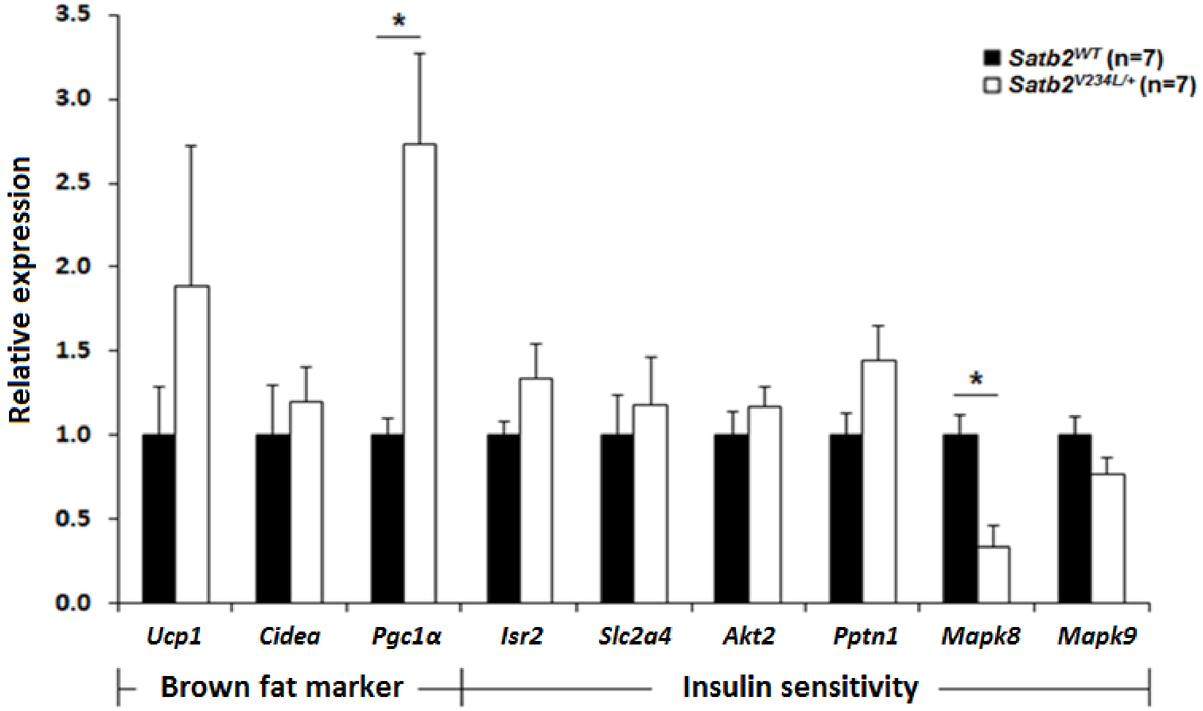

Figure 20. qRT-PCR analysis of eWAT gene expression from male *Satb2*$^{V234L/+}$ and *Satb2*^{WT} mice at the age of sixteen weeks.

Expression levels of selected genes in eWAT from *Satb2*$^{V234L/+}$ and *Satb2*^{WT} mice (n=7). Expression levels were normalized to the housekeeping genes *Cyc1* and *Tbp*. (*: $p \leq 0.05$.)

4.2 Differences found in the Dll1T720A mouse line

4.2.1 Primary screen in the GMC without wild-type littermates

In the primary screen of the Dll1T720A mouse line, some significant phenotypes were shown in the homozygous Dll1T720A mutants (*Dll1*$^{T720A/-}$) compared with wild-type (*Dll1*^{WT}) mice. *Dll1*$^{T720A/-}$ mice were leaner and smaller, bone mineral and fat related parameters were strongly reduced compared with *Dll1*^{WT} mice. Furthermore, *Dll1*$^{T720A/-}$ mice exhibited increased locomotor activities and decreased grip strength. Some parameters were notably changed in clinical chemical and hematological screening (Table 10).

Table 10. Parameters which were significantly changed in *Dll1*$^{T720A/-}$ mice compared to *Dll1*^{WT} mice in the primary GMC screen.

Screen	Parameters
Dysmorphology	bone mineral density ↓, bone mineral content ↓, body length ↓, body weight ↓, body weight ↓, fat content ↓, lean content ↑
Behavior	forward locomotion ↑
Neruology	grip strength ↓
Clinical chemistry	cholesterol ↓, alkaline phosphatase ↑, alpha-amylase ↓, ferritin, transferrin ↓, red blood cell ↓, hemoglobin ↓, hematocrit ↓, mean corpuscular volume ↑, mean corpuscular hemoglobin ↑, red blood cell distribution width ↓

Moreover, non-invasive blood pressure, the steroid hormone dehydroepiandrosterone (DHEA) and most of main leukocyte subsets (frequencies of B cells and CD4T, IgG and IgM antibodies) in the immunology screen were significantly changed between *Dll1*$^{T720A/-}$ and *Dll1*^{WT} mice. Since no wild-type littermates were available and the age of mice for some measurements was not comparable, parts of the measurements in the primary screen should be repeated with age-matched Dll1T720A cohorts of mutants and wild-type littermates.

4.2.2 Secondary Screen including wild-type littermates revealed transient differences in body composition

Loss-of-function of DLL1 can induce plenty of alternative phenotypes in skeletal development, metabolism and energy balance[182-185]. Therefore, dysmorphological, metabolic, clinical chemical, hematological and grip-force analyses were repeated in the secondary GMC screen. In addition, some metabolism-related parameters were measured to verify the metabolic phenotypes of *Dll1*$^{T720A/-}$ mutant mice observed in the primary screen.

The *Dll1*$^{T720A/-}$ mice and wild-type littermates as control were generated from intercross matings of heterozygous *Dll1*$^{T720A/+}$ mice (Figure 21A). Genotyping was performed by restriction digestion of a *Dll1* PCR fragment with Bpu10I, which can recognize the A to G mutation in Dll1T720A mutants (Figure 21B).

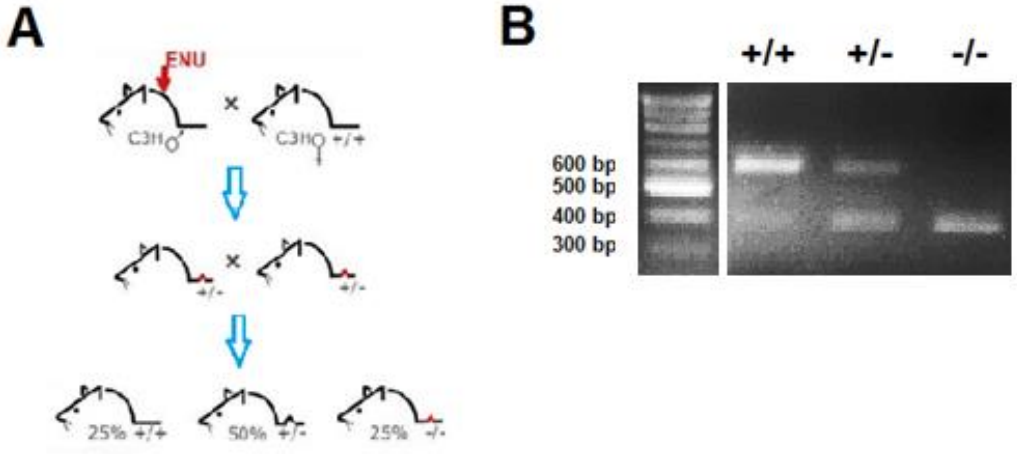

Figure 21. Breeding scheme and genotyping of the Dll1T720A mouse line.

A. Schematic diagram of the Dll1T720A mice breeding process. **B** Genotyping results of littermates from a heterozygous *Dll1*$^{T720A/+}$ intercross. Wild-type mice had 2 bands (638 + 86 bp), heterozygous *Dll1*$^{T720A/+}$ mice had 4 bands (638 + 419 + 219 + 86 bp) and homozygous *Dll1*$^{T720A/-}$ mice had 3 bands (419 + 219 + 86 bp). Due to the chosen gel concentration bands smaller than 419 bp are not visible.

To investigate bone mineral density (BMD), dual-energy X-ray absorptiometry (DEXA) and peripheral quantitative computed tomography (pQCT) measurements were performed on same mice for three times at different time points. The measurements were done in collaboration with Dr. Wolfgang Hans (Institute of Experimental Genetics, Helmholtz

Zentrum München). Most of DEXA parameters displayed no significant differences between analyzed groups when the mice were measured at the age of nine, sixteen and thirty-three weeks (Table 11-13). However, BMD and bone mineral content (BMC) values of male *Dll1*$^{T720A/-}$ mice were significantly decreased at the age of sixteen weeks, while age-matched female *Dll1*$^{T720A/-}$ mice showed a trend towards increased values. Instead of abnormal BMD and BMC, reduced body length and body weight were observed in thirty-three old male *Dll1*$^{T720A/-}$ mice. Female mice slightly showed a tendency to decreased values.

Table 11. Bone parameters obtained by DEXA measured at the age of nine weeks.

Parameter (9 weeks)	**Male**			**Female**		
	Dll1^{WT} **(n=10)**	***Dll1***$^{T720A/-}$ **(n=10)**	**P-value**	***Dll1***^{WT} **(n=10)**	***Dll1***$^{T720A/-}$ **(n=10)**	**P-value**
BMD *[mg/cm^2]*	48 ± 3	49 ± 3	n.s.	48 ± 3	50 ± 4	n.s.
BMC *[mg]*	476 ± 47	420 ± 91	n.s.	400 ± 55	414 ± 62	n.s.
Bone content *[%]*	1.73 ± 0.16	1.54 ± 0.32	n.s.	1.72 ± 0.22	1.70 ± 0.23	n.s.
Bone length *[cm]*	9.50 ± 0.24	9.54 ± 0.16	n.s.	9.33 ± 0.14	9.49 ± 0.23	n.s.
Body weight *[g]*	27.53 ± 1.23	27.17 ± 0.89	n.s.	23.33 ± 0.77	24.44 ± 1.48	n.s.

Table 12. Bone parameters obtained by DEXA measured at the age of sixteen weeks.

Parameter (16 weeks)	**Male**			**Female**		
	Dll1^{WT} **(n=10)**	***Dll1***$^{T720A/-}$ **(n=10)**	**P-value**	***Dll1***^{WT} **(n=10)**	***Dll1***$^{T720A/-}$ **(n=10)**	**P-value**
BMD *[mg/cm^2]*	60 ± 4	58 ± 2	≤ 0.05	59 ± 3	61 ± 2	n.s.
BMC *[mg]*	803 ± 162	689 ± 53	≤ 0.05	680 ± 134	783 ± 182	n.s.
Bone content *[%]*	2.30 ± 0.39	2.06 ± 0.13	n.s.	2.21 ± 0.28	2.41 ± 0.41	n.s.
Bone length *[cm]*	9.93 ± 0.23	9.98 ± 0.25	n.s.	9.81 ± 0.23	10.04 ± 0.17	≤ 0.05
Body weight *[g]*	34.74 ± 1.86	33.38 ± 1.62	n.s.	30.54 ± 2.24	32.21 ± 2.29	n.s.

Table 13. Bone parameters obtained by DEXA measured at the age of thirty-three weeks.

Parameter (33 weeks)	Male			Female		
	Dll1^{WT} (n=10)	*Dll1*$^{T720A/-}$ (n=10)	P-value	*Dll1*^{WT} (n=10)	*Dll1*$^{T720A/-}$ (n=10)	P-value
BMD *[mg/cm^2]*	81 ± 29	68 ± 3	n.s.	73 ± 1	71 ± 4	n.s.
BMC *[mg]*	1039 ± 480	1280 ± 116	n.s.	1467 ± 87	1373 ± 273	n.s.
Bone content *[%]*	2.30 ± 1.07	3.11 ± 0.29	n.s.	3.21 ± 0.14	3.23 ± 0.35	n.s.
Bone length *[cm]*	11.07 ± 0.27	10.64 ± 0.24	≤ 0.05	11.10 ± 0.22	10.99 ± 0.18	n.s.
Body weight *[g]*	44.14 ± 1.35	41.23 ± 1.54	n.s.	45.76 ± 3.48	42.09 ± 5.20	≤ 0.05

To confirm the findings obtained by DEXA measurement and to give a more detailed analysis of bone parameters, pQCT measurements were performed in the secondary screen for three times at different time points to quantify alterations in the femur of *Dll1*$^{T720A/-}$ mice. The pQCT scans were taken at proximal femur metaphysis and diaphysis (Figure 22), some parameters of the metaphysis were significantly elevated in female *Dll1*$^{T720A/-}$ mice at the age of eight and sixteen weeks (Table 14, 15). When the mice were thirty-two weeks old, no phenotypes were observed in female mutant mice, but male mutant mice showed some significantly decreased bone parameters compared with wild-type mice (Table 16).

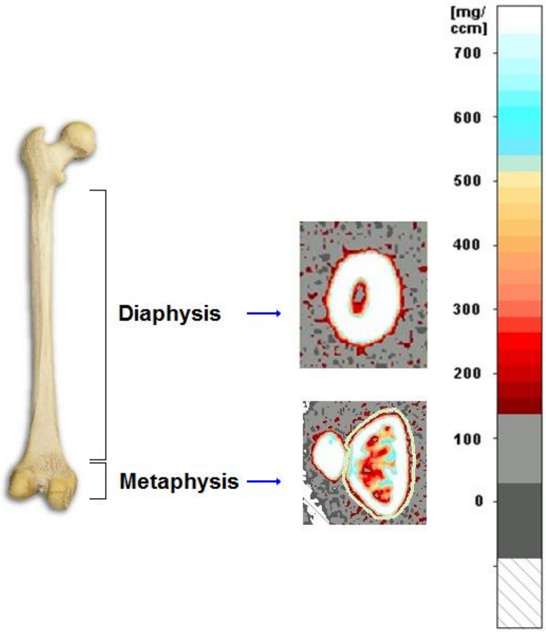

Figure 22. Schematic diagram of pQCT measurements of diaphysis and metaphysis in femur.

Table 14. Femur parameters obtained by pQCT measured at the age of eight weeks.

	Parameter (8 weeks)	Male			Female		
		$Dll1^{WT}$ (n=10)	$Dll1^{T720A/-}$ (n=10)	P-value	$Dll1^{WT}$ (n=10)	$Dll1^{T720A/-}$ (n=10)	P-value
metaphysis	**Total Content** *[mg]*	2.36 ± 0.08	2.44 ± 0.12	n.s.	2.45 ± 0.12	2.62 ± 0.12	≤ 0.01
	Total Density *$[mg/cm^3]$*	699.12 ± 21.44	710.40 ± 30.24	n.s.	784.44 ± 49.62	784.97 ± 41.65	n.s.
	Total Area *$[mm^2]$*	3.38 ± 0.13	2.43 ± 0.14	n.s.	3.13 ± 0.17	3.35 ± 0.23	≤ 0.05
	Cortical Content *[mg]*	2.06 ± 0.08	2.14 ± 0.15	n.s.	2.26 ± 0.14	2.43 ± 0.13	≤ 0.05
	Cortical Density *$[mg/cm^3]$*	841.12 ± 22.47	855.23 ± 29.76	n.s.	924.02 ± 31.13	906.04 ± 47.06	n.s.
	Cortical Area *$[mm^2]$*	2.45 ± 0.11	2.51 ± 0.21	n.s.	2.44 ± 0.16	2.69 ± 0.24	≤ 0.05
	Trabecular Content *[mg]*	0.30 ± 0.03	0.29 ± 0.05	n.s.	0.20 ± 0.04	0.20 ± 0.03	n.s.
	Trabecular Density *$[mg/cm^3]$*	322.07 ± 13.99	321.85 ± 16.89	n.s.	286.75 ± 22.36	300.91 ± 17.23	n.s.
	Trabecular Area *$[mm^2]$*	0.93 ± 0.10	0.93 ± 0.17	n.s.	0.68 ± 0.18	0.67 ± 0.13	n.s.
diaphysis	**Total Content** *[mg]*	2.00 ± 0.06	2.08 ± 0.08	≤ 0.05	1.88 ± 0.06	1.99 ± 0.11	≤ 0.05
	Total Density *$[mg/cm^3]$*	900.74 ± 32.36	996.48 ± 28.33	n.s.	1037.83 ± 48.31	1047.26 ± 31.98	n.s.
	Total Area *$[mm^2]$*	2.02 ± 0.09	2.08 ± 0.08	n.s.	1.82 ± 0.12	1.90 ± 0.09	n.s.
	Cortical Content *[mg]*	1.94 ± 0.06	2.01 ± 0.08	≤ 0.05	1.84 ± 0.06	1.94 ± 0.11	≤ 0.05
	Cortical Density *$[mg/cm^3]$*	1121.00 ± 26.02	1132.48 ± 21.47	n.s.	1149.58 ± 46.91	1145.73 ± 29.28	n.s.
	Cortical Area *$[mm^2]$*	1.73 ± 0.07	1.78 ± 0.07	n.s.	1.60 ± 0.11	1.69 ± 0.10	n.s.
	Trabecular Content *[mg]*	0.07 ± 0.01	0.07 ± 0.01	n.s.	0.05 ± 0.01	0.05 ± 0.01	n.s.
	Trabecular Density *$[mg/cm^3]$*	219.25 ± 18.25	210.86 ± 16.43	n.s.	209.11 ± 24.60	236.55 ± 37.19	n.s.
	Trabecular Area *$[mm^2]$*	0.29 ± 0.05	0.31 ± 0.03	n.s.	0.22 ± 0.04	0.21 ± 0.03	n.s.

Table 15. Femur parameters obtained by pQCT measured at the age of sixteen weeks.

	Parameter (16 weeks)	Male		P-value	Female		P-value
		Dll1^{WT} (n=10)	*Dll1*$^{T720A/-}$ (n=10)		*Dll1*^{WT} (n=10)	*Dll1*$^{T720A/-}$ (n=10)	
metaphysis	**Total Content** *[mg]*	2.13 ± 0.10	2.14 ± 0.13	n.s.	2.00 ± 0.11	2.16 ± 0.11	≤ 0.01
	Total Density *[mg/cm^3]*	658.17 ± 22.98	660.39 ± 34.74	n.s.	703.48 ± 38.22	711.98 ± 18.98	n.s.
	Total Area *[mm^2]*	3.24 ± 0.14	2.25 ± 0.15	n.s.	2.85 ± 0.10	3.03 ± 0.17	≤ 0.05
	Cortical Content *[mg]*	1.81 ± 0.11	1.81 ± 0.15	n.s.	1.78 ± 0.12	1.91 ± 0.11	≤ 0.05
	Cortical Density *[mg/cm^3]*	803.04 ± 26.99	818.86 ± 20.03	n.s.	858.12 ± 18.02	855.54 ± 18.99	n.s.
	Cortical Area *[mm^2]*	2.27 ± 0.19	2.20 ± 0.14	n.s.	2.07 ± 0.13	2.23 ± 0.14	≤ 0.05
	Trabecular Content *[mg]*	0.32 ± 0.03	0.34 ± 0.05	n.s.	0.23 ± 0.02	0.25 ± 0.02	n.s.
	Trabecular Density *[mg/cm^3]*	327.16 ± 24.95	324.40 ± 14.25	n.s.	295.71 ± 28.77	310.53 ± 11.01	n.s.
	Trabecular Area *[mm^2]*	0.98 ± 0.12	1.04 ± 0.16	n.s.	0.78 ± 0.14	0.80 ± 0.08	n.s.
diaphysis	**Total Content** *[mg]*	1.49 ± 0.06	1.52 ± 0.07	n.s.	1.32 ± 0.03	1.38 ± 0.06	≤ 0.01
	Total Density *[mg/cm^3]*	806.49 ± 22.09	825.27 ± 27.74	n.s.	829.23 ± 25.98	830.27 ± 21.97	n.s.
	Total Area *[mm^2]*	1.84 ± 0.08	1.84 ± 0.07	n.s.	1.59 ± 0.05	1.66 ± 0.04	≤ 0.05
	Cortical Content *[mg]*	1.41 ± 0.05	1.45 ± 0.07	n.s.	1.26 ± 0.04	1.32 ± 0.06	≤ 0.01
	Cortical Density *[mg/cm^3]*	998.69 ± 10.89	1011.62 ± 18.67	n.s.	1013.28 ± 10.74	1008.67 ± 19.51	n.s.
	Cortical Area *[mm^2]*	1.41 ± 0.05	1.43 ± 0.06	n.s.	1.24 ± 0.02	1.31 ± 0.06	≤ 0.01
	Trabecular Content *[mg]*	0.08 ± 0.01	0.07 ± 0.01	n.s.	0.06 ± 0.01	0.06 ± 0.01	n.s.
	Trabecular Density *[mg/cm^3]*	174.64 ± 8.57	177.77 ± 12.14	n.s.	175.97 ± 8.24	175.28 ± 9.81	n.s.
	Trabecular Area *[mm^2]*	0.43 ± 0.05	0.41 ± 0.04	n.s.	0.35 ± 0.05	0.36 ± 0.04	n.s.

Table 16. Femur parameters obtained by pQCT measured at the age of thirty-two weeks.

	Parameter (32 weeks)	**Male**			**Female**		
		$Dll1^{WT}$ **(n=7)**	$Dll1^{T720A/-}$ **(n=7)**	**P-value**	$Dll1^{WT}$ **(n=7)**	$Dll1^{T720A/-}$ **(n=7)**	**P-value**
metaphysis	**Total Content** *[mg]*	2.46 ± 0.10	2.35 ± 0.10	n.s.	2.94 ± 0.13	2.98 ± 0.15	n.s.
	Total Density $[mg/cm^3]$	676.39 ± 26.54	647.90 ± 25.78	n.s.	801.62 ± 24.33	813.82 ± 46.12	n.s.
	Total Area $[mm^2]$	3.64 ± 0.12	3.64 ± 0.13	n.s.	3.66 ± 0.12	3.66 ± 0.09	n.s.
	Cortical Content *[mg]*	2.11 ± 0.12	1.96 ± 0.13	≤ 0.05	2.75 ± 0.15	2.81 ± 0.20	n.s.
	Cortical Density $[mg/cm^3]$	862.27 ± 19.06	842.29 ± 13.97	≤ 0.05	923.84 ± 31.31	912.89 ± 14.92	n.s.
	Cortical Area $[mm^2]$	2.45 ± 0.16	2.33 ± 0.14	n.s.	2.98 ± 0.17	3.07 ± 0.20	n.s.
	Trabecular Content *[mg]*	0.35 ± 0.03	0.39 ± 0.05	≤ 0.05	0.19 ± 0.04	0.17 ± 0.05	n.s.
	Trabecular Density $[mg/cm^3]$	293.46 ± 17.21	301.36 ± 12.87	n.s.	275.44 ± 25.92	294.51 ± 22.88	n.s.
	Trabecular Area $[mm^2]$	1.19 ± 0.14	1.31 ± 0.17	n.s.	0.69 ± 0.18	0.58 ± 0.21	n.s.
diaphysis	**Total Content** *[mg]*	2.56 ± 0.11	2.41 ± 0.14	≤ 0.05	2.48 ± 0.06	2.51 ± 0.07	n.s.
	Total Density $[mg/cm^3]$	1058.74 ± 23.07	1050.61 ± 23.43	n.s.	1114.73 ± 49.32	1135.04 ± 31.32	n.s.
	Total Area $[mm^2]$	2.42 ± 0.08	2.29 ± 0.12	≤ 0.05	2.23 ± 0.09	2.22 ± 0.06	n.s.
	Cortical Content *[mg]*	2.50 ± 0.11	2.35 ± 0.14	≤ 0.05	2.44 ± 0.07	2.47 ± 0.06	n.s.
	Cortical Density $[mg/cm^3]$	1181.40 ± 16.80	1173.43 ± 22.13	n.s.	1210.33 ± 15.27	1219.47 ± 19.58	n.s.
	Cortical Area $[mm^2]$	2.11 ± 0.07	2.00 ± 0.13	n.s.	2.01 ± 0.06	2.02 ± 0.05	n.s.
	Trabecular Content *[mg]*	0.07 ± 0.01	0.06 ± 0.01	n.s.	0.05 ± 0.02	0.04 ± 0.01	n.s.
	Trabecular Density $[mg/cm^3]$	216.63 ± 14.71	216.20 ± 17.92	n.s.	229.73 ± 34.08	239.47 ± 33.15	n.s.
	Trabecular Area $[mm^2]$	0.31 ± 0.03	0.29 ± 0.04	n.s.	0.22 ± 0.10	0.19 ± 0.04	n.s.

To further investigate bone morphology and density, high-resolution images of tibia and femur from sixteen weeks old mice were performed by micro computed tomography (µCT). The work was done in collaboration with Dr. med. Paul Zaslansky (Julius Wolff Institute for Biomechanics and Musculoskeletal Regeneration, Charité - Universitätsmedizin Berlin). Three-dimensional reconstruction images showed the anterior surface of the long bones. No abnormalities were observed in the overview graphics of mutant mice when compared to control mice (Fig. 23A, C). Two-dimensional images showed trabecular bone and cortical bone of tibia and femur, which expressed no differences between control and mutant groups (Fig. 23B, D).

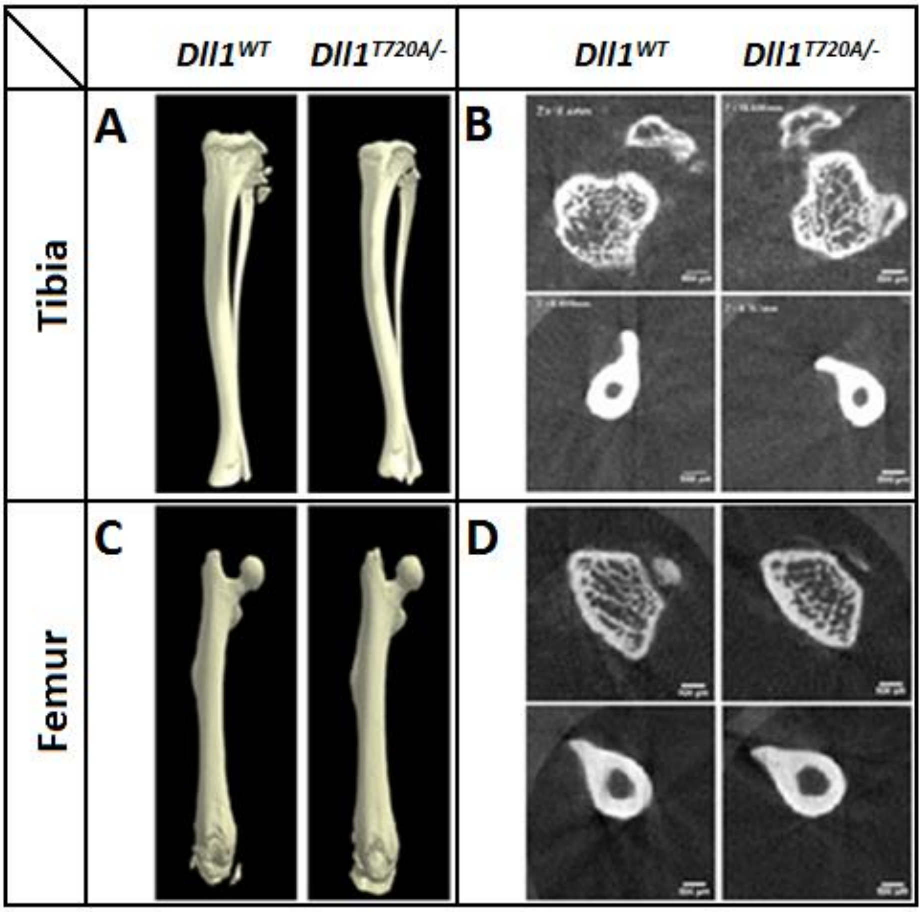

Figure 23. Micro CT analysis of the tibiae and femora at the age of sixteen weeks.

A and C Three-dimensional reconstruction images of tibia (A) and femur (C). **B and D** Two-dimensional images of trabecular (upper panels) and cortical bone (lower panels) of tibia (B) and femur (D).

Metabolic analysis

Metabolic analysis was performed to further explore the metabolic phenotypes (increased lean body mass and reduced body size) of *Dll1*$^{T720A/-}$ mice observed in the primary screen. Body compositions were tested for four times in eight to fifty-two weeks old mice by nuclear magnetic resonance (NMR) technology. Body mass, fat content and lean content of the mice are shown by diagrams for all time points of the measurement (Fig. 24). Mean body mass of both male and female *Dll1*$^{T720A/-}$ mice revealed a trend towards decreased values. Specifically, at the age of thirty-two weeks body mass of mutant mice was significantly decreased in both genders when compared with *Dll1*^{WT} mice. Fat content of male *Dll1*$^{T720A/-}$ mice was lower than of wild-type counterparts from the beginning of the study until the age of thirty-two weeks. Unlike male mutant mice, female mice showed no significant differences between genotypes at all measured time points. As expected based on changes in the fat content, both male and female *Dll1*$^{T720A/-}$ mice depicted a tendency toward an increased percent lean mass especially when the male mice were measured at the age of thirty weeks. However, the lean content of male *Dll1*$^{T720A/-}$ mice was significantly lower than in *Dll1*^{WT} littermates when the mice were fifty-two weeks old.

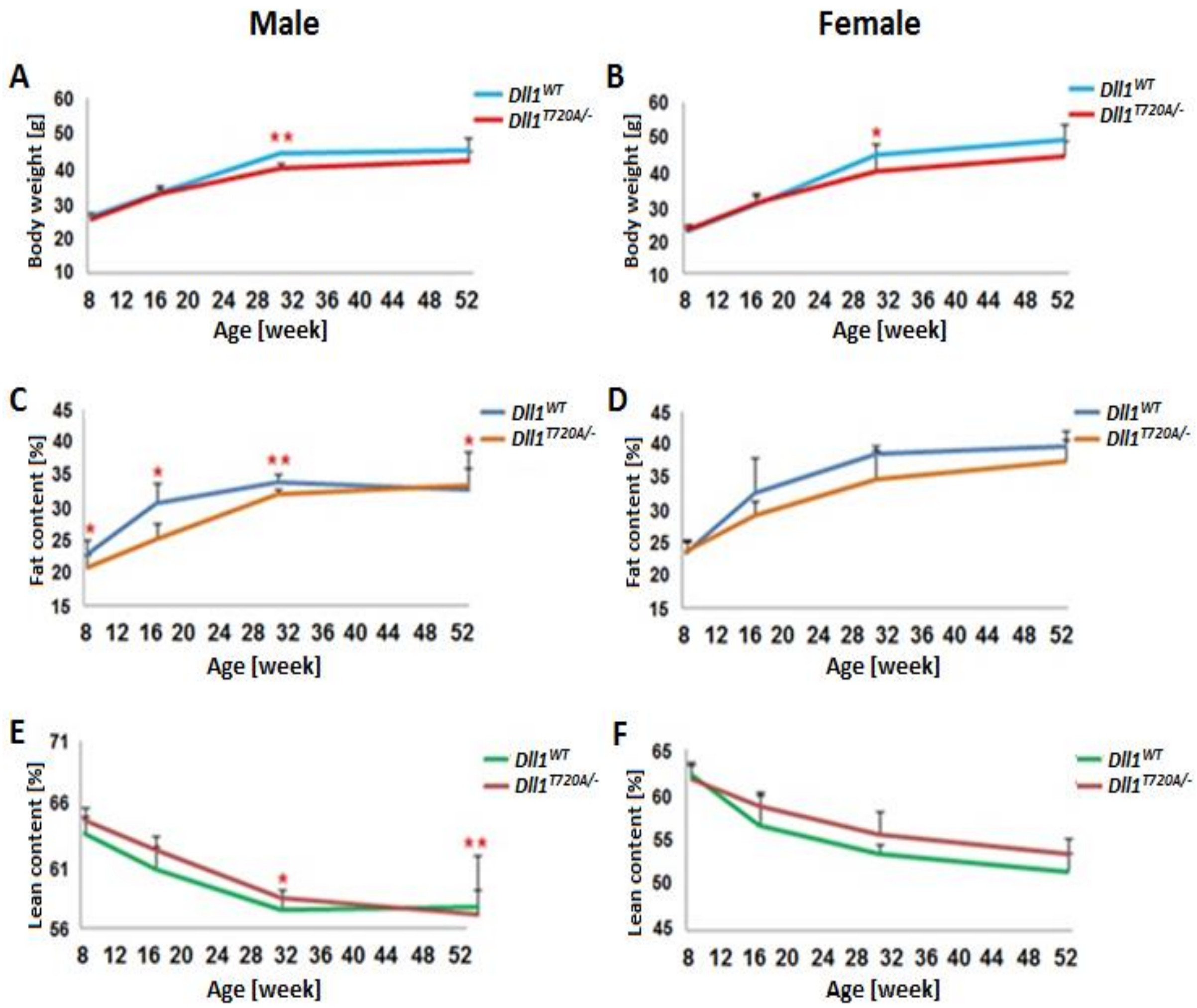

Figure 24. Body composition parameters in percent found in *Dll1*$^{T720A/-}$ and *Dll1*^{WT} mice measured at four time points from eight until fifty-two weeks of age (n=7).

A and B Body weight curves of male (A) and female (B) mice during the measurement period. *Dll1*$^{T720A/-}$ mutant mice displayed strongly reduced body weight in both genders at the age of thirty-two weeks. **C and D** Fat content curves of male (C) and female (D) mice during the observation period. The fat content of male *Dll1*$^{T720A/-}$ mice was significantly decreased at all time points except at the age of fifty-two weeks. **E and F** Lean content curves of the male (E) and female (F) mice revealed that male *Dll1*$^{T720A/-}$ mice had higher lean content at the age of thirty-two weeks but lower values at the age of fifty-two weeks.

Stronger differences were observed when the mice were sixteen weeks old. Linear mixed-effects models were performed to analyze body composition parameters at this time point. Each type of event (sex, genotype and body weight) was investigated for a significant effect on fat mass and lean mass (Table 17). Fat mass and lean mass were significantly different between *Dll1*$^{T720A/-}$ and *Dll1*^{WT} mice. The differences were affected by sex and body weight but not by genotype (Figure 25).

Table 17. Body composition parameters obtained by NMR measured at the age of sixteen weeks.

Parameter	**Male**		**Female**		**Linear model (P-value)**			
16 weeks	***Dll1***^{WT} **(n=7)**	***Dll1***$^{T720A/-}$ **(n=7)**	***Dll1***^{WT} **(n=7)**	***Dll1***$^{T720A/-}$ **(n=7)**	**sex**	**genotype**	**body weight**	**Sex genotype**
Body weight *[g]*	44.3 ± 0.6	40.1 ± 1.8	44.7 ± 3.0	40.0 ± 4.8	n.s.	≤ 0.01	n/a	n.s.
Fat mass *[g]*	14.0 ± 0.6	12.0 ± 0.7	17.3 ± 1.6	14.1 ± 3.3	≤ 0.01	n.s.	≤ 0.01	≤ 01
Lean mass *[g]*	25.5 ± 0.4	23.5 ± 1.0	23.9 ± 1.2	22.1 ± 1.8	≤ 0.01	n.s.	≤ 0.01	n.s.

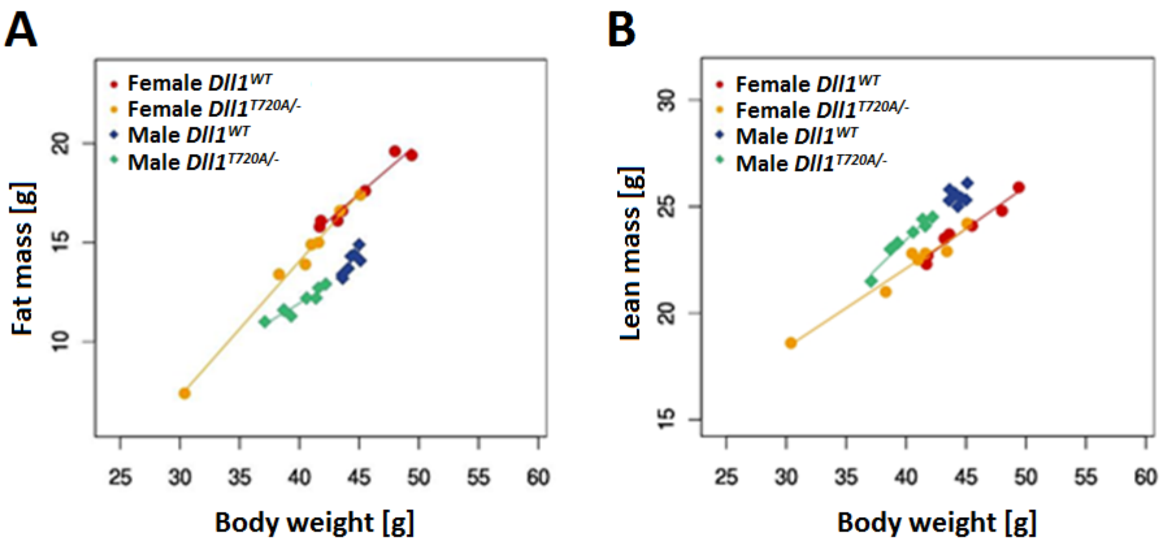

Figure 25. Body weight normalized to fat mass and lean mass in *Dll1T*$^{720A/-}$ and wild-type mice at the age of sixteen weeks old (n=7).

A Fat mass normalized to body weight between different groups in sixteen weeks old *Dll1*^{T720A} mice. **B** Lean mass to body weight correlation in *Dll1*^{T720A} mice at the age of sixteen weeks. No significant differences were observed between *Dll1*$^{T720A/-}$ mice and age-matched *Dll1*^{WT} mice.

In addition to the studies above, indirect calorimetric (IC) assays were performed when the mice were sixteen and fifty-two weeks old. The IC assay is focusing on energy metabolism by monitoring body mass, food intake, locomotor activities and respiratory exchange ratio under *ad libitum* conditions. No significant differences in energy metabolism parameters could be detected in *Dll1*$^{T720A/-}$ mice at the age of sixteen and fifty-two weeks. Since metabolic rate is strongly influenced by body weight[186], oxygen consumption values were normalized to individual body weight and performed least squared linear regression and fit the data to the formula y = mx + b (Figure 26) in all genotypes. Female and male *Dll1*$^{T720A/-}$ mice depicted a tendency toward higher weight specific oxygen consumption at sixteen and fifty-two weeks respectively, but the differences were not significant. This part of work was done in collaboration with Dr. Jan Rozman (Institute of Experimental Genetics, Helmholtz Zentrum München).

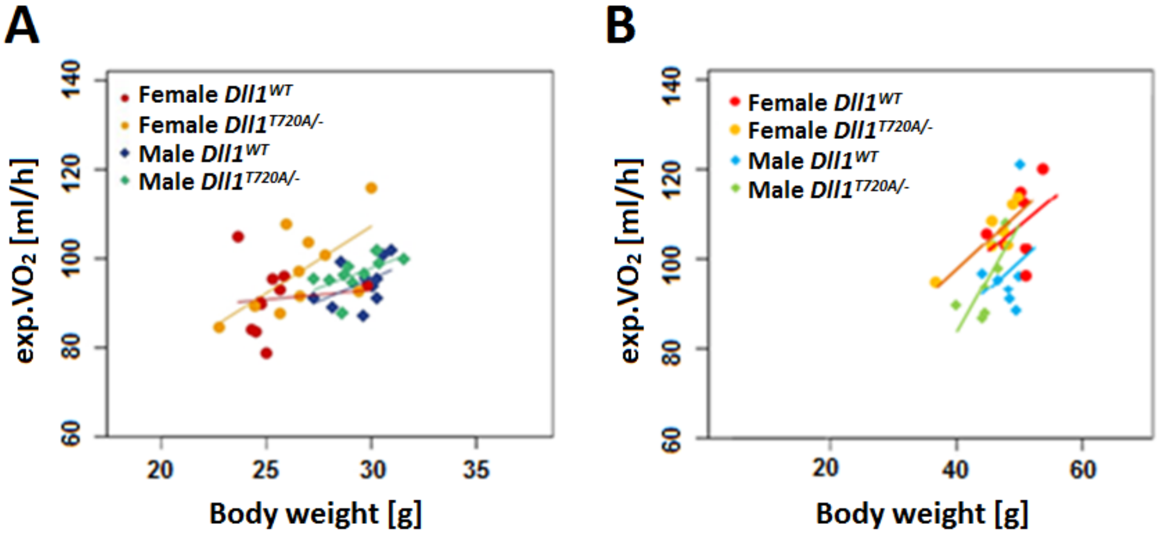

Figure 26. Correlation between body weight and oxygen expenditure (exp. VO_2) in sixteen and fifty-two weeks old mice.

A Oxygen consumption normalized to body weight between different groups when the mice were sixteen weeks old (n=10). **B** Oxygen consumption – body weight correlation in *Dll1*$^{T720A/-}$ mice and *Dll1*^{WT} mice at the age of fifty-two weeks (n=7). No significant differences were observed between *Dll1*$^{T720A/-}$ mice and age-matched *Dll1*^{WT} mice in both measurements.

To follow up the obvious body weight phenotypes expressed in sixteen weeks old mice, Hematoxylin and Eosin (H&E) staining of fat tissues were performed in age-matched *Dll1*$^{T720A/-}$ and *Dll1*^{WT} mice. No adipocyte size differences were observed between the two genotypes both in epididymal white adipose tissues (eWAT) and brown adipose tissues (BAT) (Figure 27).

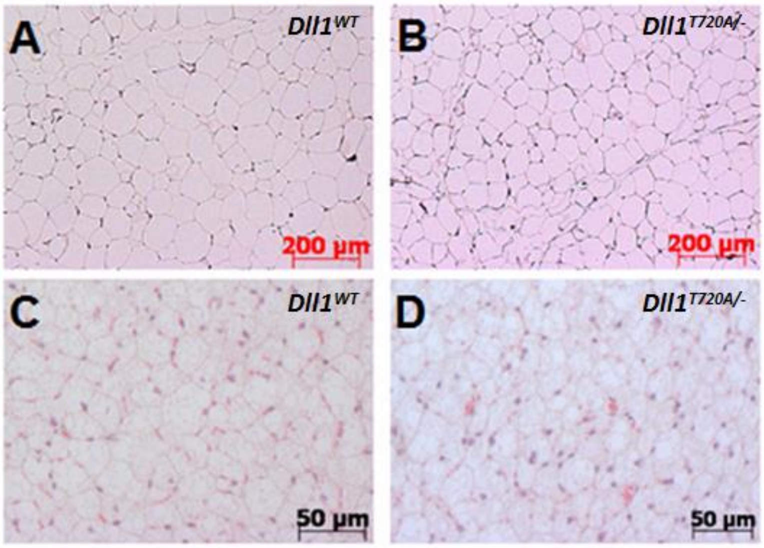

Figure 27. H&E staining of white and brown fat tissues in sixteen weeks old *Dll1*$^{T720A/-}$ and *Dll1*^{WT} mice.

WAT (A and B) and BAT (C and D) shown by H&E staining without showing clear differences in size.

Clinical chemical screening

Glucose tolerance, clinical chemical and hematological parameters were measured in plasma of *Dll1*$^{T720A/-}$ mutant mice and wild-type mice. The work was done in collaboration with Dr. Birgit Rathkolb (Institute of Experimental Genetics, Helmholtz Zentrum München). The trapezoidal rule was used to calculate the areas under the curve (AUC) when performing the intraperitoneal glucose tolerance test (ipGTT) as described[187,188]. IpGTT was first measured when the mice were ten weeks old (Figure 28A). Male *Dll1*$^{T720A/-}$ mice showed a significantly larger $AUC_{0\text{-}30min}$ than the respective control mice ($p \leq 0.05$). The same tendency was seen for the first 30 minutes in female *Dll1*$^{T720A/-}$ mice, indicative of a decreased glucose tolerance in *Dll1*$^{T720A/-}$ mice. However, the $AUC_{30\text{-}120min}$ was significantly smaller only in male ($p \leq 0.05$), but not in female *Dll1*$^{T720A/-}$ mice. The second assay was performed when the mice were thirty-three weeks old (Figure 28B). In contrast to ten weeks old mice, the $AUC_{0\text{-}30min}$ of male *Dll1*$^{T720A/-}$ mice was significantly smaller ($p \leq 0.05$) and showed an increased tendency between 30 and 120 minutes when compared with *Dll1*^{WT} mice. Female *Dll1*$^{T720A/-}$ mice exhibited a decreased AUC trend than age-matched *Dll1*^{WT} mice.

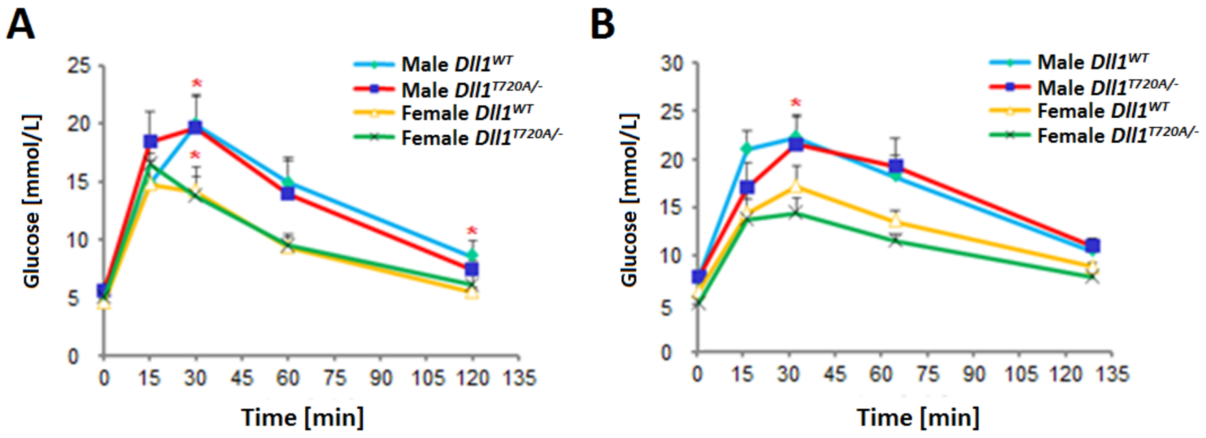

Figure 28. IpGTT in female and male *Dll1*$^{T720A/-}$ and wild-type mice in different age groups (n=10).

A IpGTT in ten weeks old mice**.** The glucose tolerance of male *Dll1*$^{T720A/-}$ mice was significantly decreased in the first 30 minutes and significantly increased from 30 to 120 minutes. **B** IpGTT in thirty-three weeks old mice**.** Significantly (p≤0.05) elevated glucose tolerance was revealed in male *Dll1*$^{T720A/-}$ mice from 0 to 30 minutes. *: p≤0.05.

Concerning clinical chemical and hematological phenotypes found significantly altered in the primary screen, these phenotypes were not observed in the secondary screen when the mice were thirty-three weeks old. However, only a few parameters were significantly changed only in female *Dll1*$^{T720A/-}$ mice. No differences could be observed between *Dll1*$^{T720A/-}$ and *Dll1*^{WT} mice except notable increased lactic acid dehydrogenase (LDH) levels in female *Dll1*$^{T720A/-}$ mice (Table 18). Although levels of white blood cell (WBC), mean corpuscular hemoglobin concentrations (MCHC) and red blood cell distribution width (RDW) were significantly different between female *Dll1*$^{T720A/-}$ mice and *Dll1*^{WT} mice (Table 19), the vales of different genotypes were close (WBC: *Dll1*$^{T720A/-}$ 9.21± 1.23 vs *Dll1*^{WT} 9.20 ± 0.96, p≤*0.005*; MCHC: *Dll1*$^{T720A/-}$ 28.73± 0.53 vs *Dll1*^{WT} 28.27± 0.49, *p≤0.05*; RDW: *Dll1*$^{T720A/-}$ 12.41± 0.19 vs *Dll1*^{WT} 12.67± 0.21, p≤*0.05*).

Table 18. Clinical chemical parameters measured at the age of thirty-three weeks.

Parameter (33 weeks)	Male *Dll1^{WT}* (n=7)	Male *Dll1$^{T720A/-}$* (n=7)	P-value	Female *Dll1^{WT}* (n=7)	Female *Dll1$^{T720A/-}$* (n=7)	P-value
Na *[mmol/L]*	147.6 ± 1.40	147.4 ± 2.37	n.s.	144.7 ± 2.14	144.3 ± 3.90	n.s.
K *[mmol/L]*	4.69 ± 0.20	4.50 ± 0.26	n.s.	4.09 ± 0.19	4.33 ± 0.26	n.s.
Ca *[mmol/L]*	2.36 ± 0.05	2.33 ± 0.05	n.s.	2.32 ± 0.07	2.32 ± 0.08	n.s.
Cl *[mmol/L]*	105.6 ± 0.76	105.0 ± 1.51	n.s.	105.0 ± 1.69	105.0 ± 3.62	n.s.
Phosphate *[mmol/L]*	1.64 ± 0.24	1.51 ± 0.33	n.s.	1.57 ± 0.16	1.41 ± 0.27	n.s.
Total Protein *[g/L]*	60.2 ± 2.31	58.3 ± 1.83	n.s.	58.0 ± 2.14	57.5 ± 2.44	n.s.
Urea *[mmol/L]*	8.42 ± 0.58	8.94 ± 0.62	n.s.	7.12 ± 0.70	8.04 ± 1.10	n.s.
Cholesterol *[mmol/L]*	4.97 ± 0.36	4.71 ± 0.42	n.s.	3.96 ± 0.32	3.61 ± 0.29	n.s.
Triglyceride *[mmol/L]*	4.11 ± 0.91	3.68 ± 0.66	n.s.	4.71 ± 1.20	4.23 ± 2.07	n.s.
GPT *[U/L]*	46.3 ± 16.71	34.9 ± 8.45	n.s.	25.7 ± 5.38	27.6 ± 4.16	n.s.
GOT *[U/L]*	50.9 ± 5.24	47.4 ± 3.78	n.s.	51.1 ± 5.93	53.7 ± 7.70	n.s.
ALP *[U/L]*	75 ± 7.6	74 ± 9.0	n.s.	97 ± 12.1	101 ± 19.1	n.s.
Glucose *[mmol/L]*	10.44 ± 1.26	10.18 ± 1.44	n.s.	10.00 ± 1.07	9.99 ± 1.55	n.s.
Lactat *[mmol/L]*	10.69 ± 1.42	11.63 ± 1.68	n.s.	9.51 ± 1.49	10.08 ± 0.73	n.s.
Fe *[µmol/L]*	34.93 ± 1.87	35.01 ± 3.22	n.s.	31.21 ± 2.18	37.97 ± 9.40	n.s.
LDH *[U/L]*	177.1 ± 29.30	154.1 ± 25.96	n.s.	131.6 ± 8.89	164.0 ± 16.59	≤ 0.01
Albumin *[g/L]*	30.31 ± 1.25	29.07 ± 1.05	n.s.	30.06 ± 1.44	30.09 ± 1.40	n.s.

GOT: glutamic oxaloacetic transaminase; GPT: glutamic pyruvic transaminase; ALP: alkaline phosphatase; LDH: lactate dehydrogenase .

Table 19. Hematological parameters measured at the age of thirty-three weeks.

Parameter (34 weeks)	**Male**			**Female**		
	Dll1^{WT} **(n=7)**	***Dll1***$^{T720A/-}$ **(n=7)**	**P-value**	***Dll1***^{WT} **(n=7)**	***Dll1***$^{T720A/-}$ **(n=7)**	**P-value**
WBC *[$10^3/mm^3$]*	8.94 ± 3.34	7.21 ± 1.06	n.s.	9.21 ± 1.23	9.70 ± 0.96	≤ 0.005
RBC *[$10^3/mm^3$]*	9.22 ± 0.31	9.21 ± 0.23	n.s.	9.67 ± 0.44	9.73 ± 0.39	n.s.
PLT *[$10^3/mm^3$]*	1075 ± 118.5	1151 ± 107.0	n.s.	1113 ± 106.3	1151 ± 166.5	n.s.
HGB *[g/dL]*	14.93 ± 0.48	14.87 ± 0.35	n.s.	15.60 ± 0.61	15.70 ± 0.65	n.s.
HCT *[%]*	51.30 ± 1.94	51.71 ± 1.52	n.s.	55.31 ± 2.61	54,66 ± 2.02	n.s.
MCV *[fl]*	55.6 ± 0.79	56.3 ± 0.76	n.s.	57.0 ± 0.58	56.1 ± 0.90	n.s.
MCH *[pg]*	162 ± 0.24	16.1 ± 0.26	n.s.	16.2 ± 0.35	16.2 ± 0.17	n.s.
MCHC *[g/dL]*	29.11 ± 0.54	28.76 ± 0.33	n.s.	28.27 ± 0.49	28.73 ± 0.53	≤ 0.05
RDW *[%]*	12.7 ± 0.25	12.6 ± 0.11	n.s.	12.7 ± 0.21	12.4 ± 0.19	≤ 0.05
MPV *[fl]*	5.83 ± 0.22	5.91 ± 0.18	n.s.	6.09 ± 0.19	6.07 ± 0.34	n.s.

WBC: white blood cell; RBC: red blood cell; PLT: platelet; HGB: hemoglobin; HCT: hematocrit; MCV: mean corpuscular volume; MCH: mean corpuscular hemoglobin; MCHC: mean corpuscular hemoglobin concentrations; RDW: red blood cell distribution width; MPV: mean platelet volume.

Grip strength measurement (Neurology screen)

The grip strength meter system was used for evaluating limb muscle strength, suggesting the functional consequences of mice on skeletal muscle control[189]. The strength of forelimbs (2 paws) and combined of forelimbs/ hind limbs (4 paws) was measured when the mice were fifty-four weeks old. The work was performed in collaboration with Dr. Lore Becker (Institute of Experimental Genetics, Helmholtz Zentrum München). No indications of a significant effect were found between the two genotypes. Additionally, when the grip strength data was normalized to body weight no significant differences could be detected. However, a slight body weight effect regarding the forelimb grip strength could be observed (Figure 29).

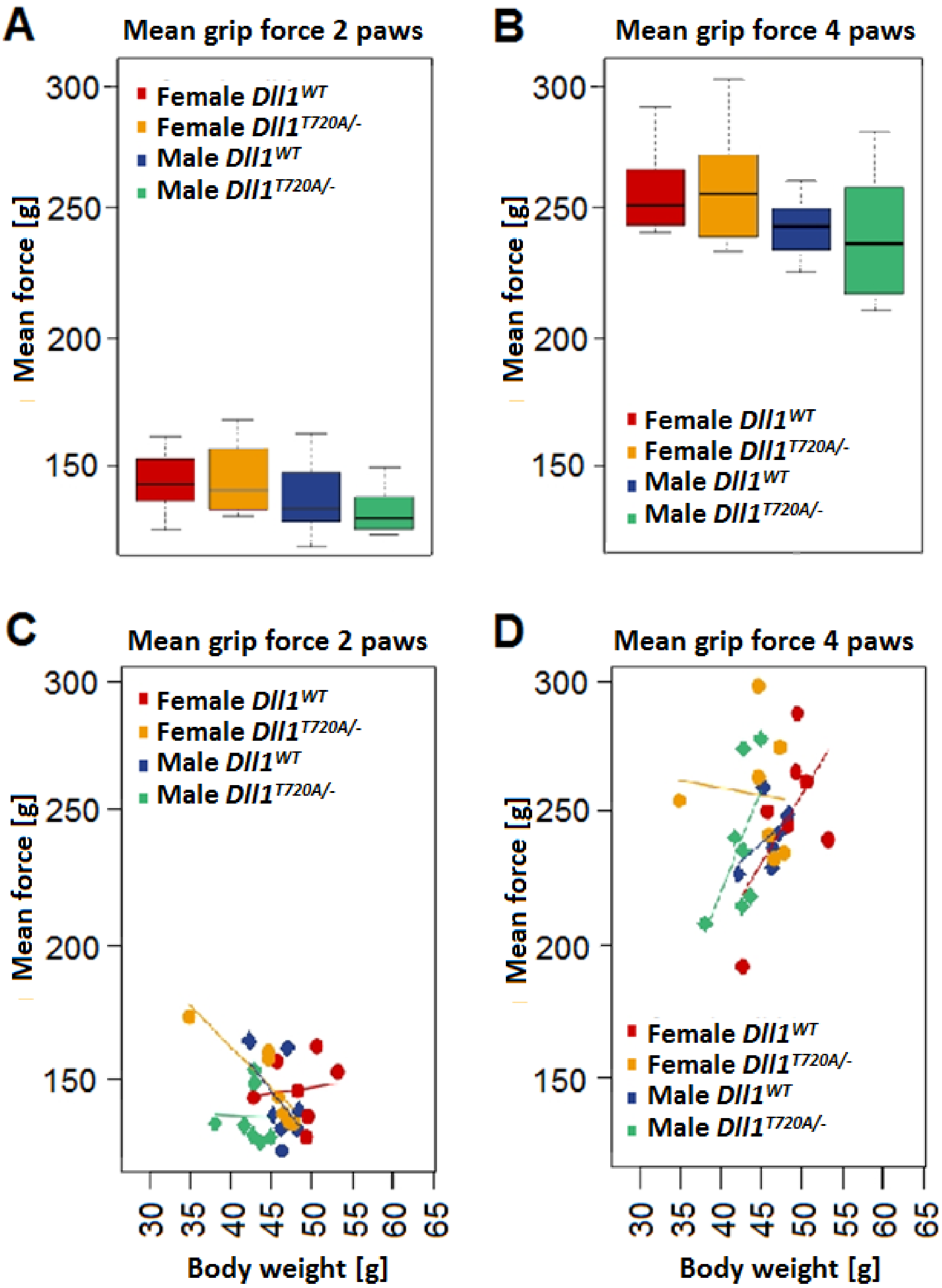

Figure 29. Box plot and linear regression model of grip force measurement in *Dll1*$^{T720A/-}$ and wild-type mice at the age of fifty-four weeks (n=7).

A and B Results of the grip force analysis displayed no significant differences in the mean grip strength of 2 paws (A) and 4 paws (B) between *Dll1*$^{T720A/-}$ and *Dll1*^{WT} mice. **C and D** Normalization of grip strength to body weight of 2 paws (C) and 4 paws (D) gave no statistical differences between *Dll1*$^{T720A/-}$ and *Dll1*^{WT} mice.

Total Thyroxine (T4) ELISA

Thyroid hormone can regulate metabolic pathways relevant to resting energy expenditure [190]. Thyroxine (T4) is the major form of thyroid hormone in the blood and was identified as metabolic biomarker and can be used in treatments of hypothyroid disorders[191-193]. Since *Dll1*$^{T720A/-}$ mice expressed observed metabolic changes in the previous measurements, levels of T4 were analyzed when the mice were 16 weeks old (Figure 30). The histogram of T4 levels showed no statistically significant differences revealed between *Dll1*$^{T720A/-}$ and *Dll1*^{WT} mice in both sexes.

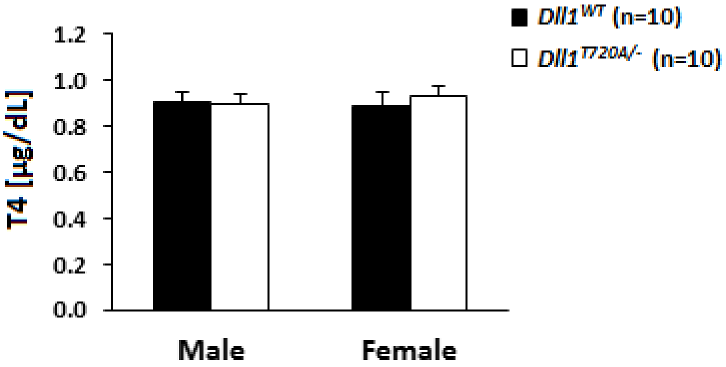

Figure 30. T4 ELISA analysis in sixteen weeks old mice.

Total thyroxine ELISA of 16 weeks old mice showed no notable differences between *Dll1*$^{T720A/-}$ and *Dll1*^{WT} mice in both male and female (n=10).

5. Discussion

5.1 The *Satb2*^{V234LMdha} mouse line

Metabolic bone diseases are disorders of bone caused by a broad spectrum of abnormalities. To gain better understanding of disease development, chemically induced mutant mice are screened to identify the mechanisms that regulate bone homeostasis. ENU mutagenesis has been used as a powerful chemical approach to identify novel mutations. The genome-wide random distribution of mutations following ENU mutagenesis have produced mouse models for various alterations, such as skeletal disorders, craniofacial abnormalities as well as metabolic syndromes[194-196]. In our genome-wide ENU mutagenesis screen, the novel dominant BAP002 mouse line was characterized by high total alkaline phosphatase (ALP) blood activities, abnormal tooth enamel and a dysgnathia phenotype[197].

5.1.1 A dominant *Satb2* mutation isolated in BAP002 mice

Using whole exome sequencing, a new dominant allele in the *Satb2* gene was found responsible for the phenotypes observed in heterozygous BAP002 mice. This V234L mutation lies in the first of two highly conserved SUMOylation sites in SATB2[120]. SUMOylation is a posttranslational modification involved in various cellular processes[198] and it targets SATB2 to the nuclear periphery[120]. Interestingly, the V234L mutation in BAP002 mice affects the third amino acid in the IKVE motif, which follows the consensus sequence ψ-K-x-D/E, where ψ is a large hydrophobic residue and x could be any residue[198]. Therefore, the valine to leucine exchange in SATB2^{V234L} should not affect SUMOylation of the protein. Moreover, results obtained from several protein prediction softwares (e.g. http://sumosp.biocuckoo.org/online.php; http://provean.jcvi.org/seq_submit.php) verified the sequence variation as *neutral* and not inducing structural or functional alterations. Nevertheless, future experiments might include a SUMOylation assay to validate the functionality of the altered recognition motif in SATB2^{V234L}.

Interestingly, analyzing mutant genomic DNA from BAP002 using NNSPLICE 0.9, a splice-site prediction tool (http://www.fruitfly.org/seq_tools/splice.html), an impaired splice-donor site at the end of exon 6 was suggested. Assuming that this is the case in *Satb2*$^{V234L/+}$ mice, exon 6 of the mutant allele would be elongated by around 50 nucleotides before generating a premature stop codon, which fulfills the criteria for nonsense mediated decay (NMD) and would force the elimination of the mutant allele. In this case, only around 50% of *Satb2* mRNA should be expressed in *Satb2*$^{V234L/+}$ mice compared to *Satb2*^{WT} mice, and no mutant protein would be generated. However, beyond this prediction, comparable *Satb2* expression levels were detected in the genotypes at both the transcriptional and protein levels, suggesting that the ENU-generated point mutation results in a normal protein variation but not an activated NMD. Up to date, SATB2 protein expression in adipose tissues was not examined in other studies. So, we currently could not explain where the observed, but obviously specific SATB2 bands in the Western-blot analysis originate from.

In the present work, *Satb2*$^{V234L/+}$ mice did not exhibit a lower frequency of weaning as described for haploinsufficient *Satb2*$^{\mathrm{tm1\ (cre)Vit}}$ mice[134]. In contrast, heterozygous *Satb2*$^{\mathrm{tm1Rug}}$ mice were phenotypically normal[124]. The different findings on these two heterozygous *Satb2* mutant mouse lines might be related to inbred strain differences. However, *Satb2*$^{V234L/-}$ mice are obviously dying following E13.5, which is in line with the perinatal lethality observed in homozygous *Satb2*$^{\mathrm{tm1(cre)Vit}}$ and *Satb2*$^{\mathrm{tm1Rug}}$ mice[124,134]. Further analyses will be necessary to address this observation along consecutive developmental stages.

5.1.2 Regulation of bone development and turnover by SATB2

5.1.2.1 Impaired bone turnover in *Satb2*$^{V234L/+}$ mice

It was shown by DEXA analysis that *Satb2*$^{V234L/+}$ mice have decreased total BMC and BMD in addition to reduced body weight, body length and fat mass. No differences were found in the ratio of body weight to body length indicating that the alteration of body weight in *Satb2*$^{V234L/+}$ mice might be due to decreased bone mass or fat mass. BMC and BMD were proved to directly regulate bone size and strength in humans and mice[199,200]. Furthermore, low BMC and BMD values are associated with an increased risk for osteoporosis, osteoporotic fractures as well as other bone diseases[201,202]. Changes of bone mineral parameters may also be related to reduced physical activity[203]. Although reduced bone mass and BMD has been suggested to change with lower grip forth[204,205], compared to wild-type littermates, no alterations had been detected regarding the grip force of two and four paws in *Satb2*$^{V234L/+}$ mice. However, an impact of the body weight on grip strength was revealed in the measurement. An early effect of SATB2 on bone mineralization has been previously confirmed by Alizarin Red staining of E15.5 homozygous *Satb2*$^{\mathrm{tm1Rug}}$ embryos[124,132]. Moreover, 2D images of the skull demonstrated that *Satb2*$^{V234L/+}$ mice have reduced bone density in cranial bones compared to *Satb2*^{WT} mice, which is in accordance with the observed phenotypes detected by DEXA analysis.

ALP is a major enzyme to regulate inorganic phosphate and pyrophosphate levels in mineralizing tissues[206]. Bone-specific ALP accounts for the primary part of total ALP and its activity is closely related to bone formation in bone metabolic diseases[207]. Since bone-specific ALP is hard to measure directly in mice[208], total ALP is generally used to represent bone-specific ALP in the absence of liver diseases shown by other liver enzymes being within the normal ranges. A positive correlation between total ALP activity and bone-specific ALP was found in mouse[209] and human cells[210]. In the present study, total plasma ALP activities were increased in both genders. This result is consistent with an impaired bone metabolism as observed in animal and clinical studies representing decreased bone mineral parameters[211,212]. However, the differences between *Satb2*$^{V234L/+}$ and *Satb2*^{WT} mice became less obviously with age. Since ALP action on bone mineralization starts in early developmental stages and its activity is increased in healthy young individuals, this observation in *Satb2*$^{V234L/+}$ mice may be in line with this mechanism. Nevertheless, the increased activities in older individuals give a hint to maintained impaired bone metabolism[213].

In previous studies, *Satb2* has been shown to affect bone formation[124,134]. In *Satb2*^{V234L} littermates, bone quality parameters (density, content as well as cross section area) of metaphysis and diaphysis in long bone were assessed by pQCT measurement. Significantly reduced bone parameters in metaphysis observed by pQCT measurement give rise to the decreased BMC and BMD as measured by DEXA analysis. However, only in male *Satb2*$^{V234L/+}$ mice significantly decreased parameters were also observed in the diaphysis compared to male *Satb2*^{WT} mice. Interestingly, sex-related differences are also well known from other mice of different inbred strains[214,215], probably due to the impact of female sex hormones leading to an increase of bone mass in female compared to male mice[216,217].

Apart from the impaired bone turnover found in *Satb2*$^{V234L/+}$ mice, µCT analysis of the skulls revealed upper jaw abnormalities and laterognathia in *Satb2*$^{V234L/+}$ mice as a direct effect of SATB2 on mandibular and dental length as previously described[218]. Together with several other genes that affect craniofacial development *Satb2* has been shown to be regulated by BMP4[219]. In human patients, deletions, disruptions as well as a *de novo* mutation in *SATB2* were found to cause facial dysmorphism including a cleft palate, asymmetric mandibular hypoplasia and abnormal sinuses[135,220-222]. With the exception of a cleft palate, these phenotypes are quite similar to *Satb2*$^{V234L/+}$ mice. The functions of SATB2 on jaw development were suggested to be mediated by SOX9 action via a cis-regulation complex[221]. In spite of that, the action of a regulatory element, which is outside of the *SATB2* coding regions, on implementing the clefts is still in discussion[223]. Interestingly, no cleft defects were observed in *Satb2*$^{V234L/+}$. However, *Satb2*$^{V234L/-}$ (homozygous) embryos analyzed at E13.5 showed mild anomalies of the oral cavity and the palatal shelf.

5.1.2.2 Impaired bone remodeling in *Satb2*$^{V234L/+}$ mice

Similar to skeletal abnormalities observed in patients carrying a *SATB2* mutation, we detected osteopenic alterations in adult *Satb2*$^{V234L/+}$ mice. Impaired bone remodeling observed in *Satb2*$^{V234L/+}$ mice was characterized by haphazard organized collagen fibers, reduced numbers of osteoblasts and increased numbers of osteoclasts. These pathological alterations partly confirm the bone defects found by DEXA and pQCT measurements. The haphazard organizations of collagen fibers demonstrates a disrupted lamellar pattern, which could reflect a deficiency of osteoblastic bone formation and an imbalance of osteoblasts and osteoclasts[224]. The reduced number of osteoblasts found in *Satb2*$^{V234L/+}$ mice was also reflected by decreased plasma osteocalcin levels, indicating a decreased bone formation[225-227].

Besides the decrease in osteoblast numbers, increased osteoclast formation in *Satb2*$^{V234L/+}$ mice may cause enhanced bone resorption, which was partly supported by increased plasma CTX-1 levels found in twenty-four weeks old male *Satb2*$^{V234L/+}$ mice and in eight month old female *Satb2*$^{V234L/+}$ mice and a tendency to increased values in male *Satb2*$^{V234L/+}$ mice. However, due to technical and capacity reasons it was not possible to follow this observation with sufficient numbers of mice tested at several time points. Thus, the observed sex differences found in CTX-1 measurement may also be due to other than genotype effects. To date, the impact of *Satb2* on osteoclastogenesis is still unclear. Although *Satb2* showed no expression in osteoclasts[124], some key osteogenic genes, such as *Runx2* and *Osterix* as well as *Atf4*, which are associated with *Satb2*[124] have been reported to modulate osteoclast differentiation[228-230]. However, a measurement of bone markers only provides a screenshot based on the individual bone turnover situation. Herein, it is still under discussion if osteoclast generation is regulated by osteoblast function[231] or if osteoclasts or their precursors negatively regulate osteoblasts probably through osteoblast-extrinsic factors[232].

In addition, some significant changes of bone-homeostasis associated parameters were obtained by clinical chemical measurements. Levels of iron and ferritin were found to be significantly decreased in *Satb2*$^{V234L/+}$ mice compared to *Satb2*^{WT} mice. Iron and ferritin were shown to directly affect bone metabolism in both animals and humans[233-235]. In agreement with our study, iron deficiency was found to be associated with increased bone resorption and decreased bone formation, as supported by decreased bone mineral content, bone mineral density as well as osteocalcin concentration[233,236]. As good biomarker for iron stores, ferritin was observed to decrease in women with high bone resorption and osteoporotic disease[235,237,238]. However, the regulation of iron in bone remodeling is so far not fully understood. *In vitro* results suggested that iron-transferrin complesxes might affect pre-osteoclast differentiation[239]. In addition, several factors may also contribute to decreased iron and ferritin levels observed in *Satb2*$^{V234L/+}$ mice, such as gender, age and temperature[238,240].

5.1.2.3 Abnormal enamel structure in *Satb2*$^{V234L/+}$ mice

Apart from known actions of *Satb2* on skeletal homeostasis, our group found for the first time that SATB2 could influence the enamel structure as shown by an ultra-structural tooth phenotype in *Satb2*$^{V234L/+}$ mice. Although tooth deficiency has been identified in *SATB2* haploinsufficiency and *Satb2*$^{-/-}$ mice[124,134], enamel abnormalities observed in *Satb2*$^{V234L/+}$ mice have not been reported for other *Satb2* mutations. In *Satb2*$^{V234L/+}$ mice, areas of aprismatic hydroxyapatite were deposited within the prism pattern (analysis performed by Dr. Hartwig Seedorf, Department of Prosthetic Dentistry, University Medical Center, Hamburg-Eppendorf, Germany). The prismless outer and inner enamel layers observed in

Satb2$^{V234L/+}$ mice could be explained by an abrasiveness of the teeth as reported in an earlier study[241]. Additional studies revealed a high expression of *Satb2* in mesenchymal stem cells derived from teeth[242] and in dental mesenchyme of murine embryos[124]. Bone and dentin are mineralized tissues which are differentiated from osteoblasts and odontoblasts, respectively. The mineralization of both is highly controlled by type I collagen during osteogenesis and dentinogenesis[243]. Recently, some diseases have been reported to disrupt bone mineralization of bone and dentin in patients[244-246] and several genetic disorders have been described[247]. Mouse models of these diseases have also been established[248,249]. However, so far no mouse models exist to study molecular pathways responsible for both enamel and bone mineralization. Therefore, *SATB2* may play a dominant role to regulate enamel micro-architecture formation through affecting ameloblastic differentiation besides its known effect on bone metabolism.

As presented herein, *Satb2*$^{V234L/+}$ mice are multiple affected in skeletal development, craniofacial morphology, bone remodeling as well as enamel formation. Although SATB2 signaling has been demonstrated to regulate embryonic development and osteoblastic differentiation it is still difficult to explain how this gene affects both increased bone turnover and aprismatic hydroxyapatite formation. Unfortunately, we were not able to measure gene expression in bone tissues because of technical problems. Therefore, further investigations on the transcriptional network related to *Satb2* should be performed to unravel the complex mechanisms modulating bone remodeling and enamel abnormalities.

5.1.3 Impact of the *Satb2* mutation on metabolism disorders

SATB2 has been identified as a DNA binding protein. Mutations in *Satb2* are associated with an isolated cleft palate and altered osteoblasts differentiation[124]. This is partly supported by our results. In addition, our findings suggest that SATB2 is also associated with the growth of adipose tissues. The growth of adipose tissue can be classified in two ways: an increase in the number of adipocytes (hyperplasia) and an enlargement of the size of adipocytes (hypertrophy). Our histological analyses revealed that *Satb2*$^{V234L/+}$ mice show a reduced size of lipids droplet together with an increased number of adipocytes per area compared to *Satb2*^{WT} mice both in terms of white and brown adipose tissues (eWAT and BAT respectively).

In the literature, a decreased size of white adipocytes is often associated with food restriction[250], increased exercises[251] as well as a low ambient temperature[252]. Since our analyses based on strictly age-matched mutants and wile-type littermates that were housed under identical environmental conditions and show no differences in locomotor, activity, the smaller size of white adipocytes in *Satb2*$^{V234L/+}$ mice seems to be of genetic origin.

5.1.3.1 Browning of adipose tissue in *Satb2*$^{V234L/+}$ mice

Studies indicate that besides the classical brown fat, which derived from a *Myf*5 expressing precursor cells[253], “brite” or “beige” cells that respond to cold exposure or β_3 agonist stimulation[62] exist within white adipose tissues. Although of different developmental origin, UCP1 is still considered to be the hallmark of both types of brown/beige adipocytes[254]. Having observed more UCP1-positive adipocytes in eWAT of *Satb2*$^{V234L/+}$ mice compared to wild-type littermates, we assumed that this browning could be promoted by *Satb2* haploinsufficiency. This hypothesis was then confirmed by gene array and qRT-PCR analyses, which were performed using age-matched animals. The analyses demonstrated that the expression level of some brown/beige adipocyte markers[255] was significantly (*Paprgc1a*, also known as *Pgc1a*) or tendentially (*Ucp1*, Cidea) increased in eWAT of *Satb2*$^{V234L/+}$ compared to *Satb2*^{WT} mice. PGC1α was identified to promote UCP1 activity after being activated by β-adrenergic and cAMP-dependent pathways[256]. Overexpression of PGC1a has been demonstrated to upregulate the expression of UCP1 and CIDEA in white subcutaneous fat depots in mice[257]. Additionally, a recent study reported that zinc finger protein 516 (ZFP516) activated PGC1α and UCP1 during WAT browning through the cAMP-CREB/ATF2 pathway[258], which was in line with significantly higher *Zfp516* expression levels observed in our gene array analysis. Therefore, we hypothesize that SATB2 may modulate browning WAT generation through the cAMP-CREB/ATF2 pathway.

Regulatory mechanisms such as phosphorylation, methylation/demethylation and histone modifications take place during adipocyte differentiation and adipogenesis[259-261]. Our gene array analysis showed that several epigenetic and transcriptional regulators were significantly regulated between the two groups. A total of 22 differentially regulated probe sets were classified as epigenetic regulators. However, it is not clear whether the differential expression of these epigenetic genes reflect the abundant appearance of BAT in epidydimal fat pads of *Satb2*$^{V234L/+}$ mice or whether SATB2 itself serves as a regulator of the expression of these genes. In vitro knockout of SATB2 in 3T3-L1 adipocytes would help to evaluate this possibility.

5.1.3.2 Insulin sensitivity increased in *Satb2*$^{V234L/+}$ mice

We found that our *Satb2* mutation leads to browning of WAT and an increased expression level of *Ucp1* in eWAT in *Satb2*$^{V234L/+}$ mice. Transgenic mice that over-express *Ucp1* in white adipose tissues show a better glucose tolerance and are more insulin sensitive than control mice[82]. These clues led us to hypothesize that an altered glucose metabolism may occur in our mutant mice. The decrease of glucose levels during an ipGTT in *Satb2*$^{V234L/+}$ mice at the age of thirteen and seventeen weeks suggests that *Satb2*$^{V234L/+}$ mice are comparatively increased glucose tolerant compared to *Satb2*^{WT} mice. In addition, in further support of such a link, we noticed reduced insulin levels in 17-week-old *Satb2*$^{V234L/+}$ mice compared to age-matched *Satb2*^{WT} mice during ipGTT at all three time-points (0, 60 and 120 minutes). This result suggests a higher glucose tolerance of *Satb2*$^{V234L/+}$ mice caused by increased insulin sensitivity instead of activated insulin secretion. Our observations are in agreement with studies showing that glucose tolerance and insulin sensitivity were improved in mice with induced browning white adipose tissue[262]. However, one recent study demonstrated that brite adipose tissue, although showing an enhanced glucose uptake capacity, does not show a higher insulin sensitivity compared to WAT[263]. It has been demonstrated in rat adipocytes that leptin acts as a negative regulator of insulin sensitivity and glucose uptake[264]. However, in our tests, we did not observe a significant difference in leptin levels between the two genotypes, indicating that leptin was not crucial to active insulin sensitivity in *Satb2*$^{V234L/+}$ mice.

In the context of an increased glucose uptake and decreased insulin levels in plasma of *Satb2*$^{V234L/+}$ mice, expression of some genes related to insulin sensitivity in eWAT further suggest that the browning of white fat is responsible for the altered insulin sensitivity in *Satb2*$^{V234L/+}$ mice. Our gene expression profiling data showed significantly up-regulated expression of *Irs2*, *Slc2a4* (also known as *Glut4*) and *Akt2*, but a significant decreased expression of *Mapk8* as well as *Mapk9* in *Satb2*$^{V234L/+}$ mice compared to wile-type littermates.

Insulin receptor substrate 2 (IRS2) belongs to a molecular family that is directly phosphorylated in the insulin signaling pathway[265]. Up-regulated *Irs2* was found to activate glucose tolerance and insulin sensitivity[266,267], which is in agreement with the phenotype we observed in our ipGTT study. It has been recently reported that the effect of IRS2 functionality on insulin metabolism is more likely mediated by maintaining a functional β-cell mass rather than β-cell proliferation[268]. In addition, adiponectin was shown to increase *Irs2* expression in the liver through activation of STAT3[267], which was also found to be significantly unregulated in eWAT of *Satb2*$^{V234L/+}$ mice. However, the levels of plasma adiponectin in the two groups of mice in our study were quite similar. So, future experiments could help to clarify whether *Irs2* up-regulation is also present in the pancreas of *Satb2*$^{V234L/+}$ mice and whether differences in functional β-cell mass exist between mutant and wild-type mice. Additionally, *Slc2a4/Glut4* and *Akt2* are essential genes in the insulin-signaling pathway, with Glut4 being the major transporter protein for glucose uptake in muscle cells. Increased levels of *Slc2a4/Glut4* and *Akt2* in skeletal muscle were shown to be associated with improved insulin sensitivity[269]. Interestingly, previous studies discovered that *Glut4* gene expression was higher in BAT compared to WAT of humans[270] and increased *Glut4* expression was observed in mice showing browning of white fat[271]. Although it is assumed that *Akt2* contributes to adipose differentiation[272], the effect of AKT2 on browning remains poorly understood.

MAPK8 and MAPK9, also known as JNK1 and JNK2, are two mitogen-activated protein kinases ubiquitously expressed in mice[273]. As the main JNK isoforms expressed in adipose tissues[273], JNK1 and JNK2 were indicated to regulate metabolic changes through the modification of IRS1[274,275]. Here we found that the expression of MAPK8/JNK1 was significantly decreased in *Satb2*$^{V234L/+}$ mice compared to *Satb2*^{WT} mice. Deficiency of JNK1 led to higher insulin sensitivity and enhanced insulin receptor signaling in mice[276], which is in line with increased insulin sensitivity in *Satb2*$^{V234L/+}$ mice. Additionally, similar expression levels of MAPK9/JNK2 between the two groups suggest that JNK2 might not play a measurable role in the heterozygous mice. However, we observed that IRS2 but not IRS1, was strongly regulated in *Satb2*$^{V234L/+}$ mice compared to *Satb2*^{WT} mice. Though IRS2 has been shown to compensate IRS1 activity in the liver after refeeding[277], it is still ambiguous how the homeostasis of IRS1 and IRS is regulated.

5.1.3.3 Energy expenditure changes in *Satb2*$^{V234L/+}$ mice

The present study showed that body weight and composition were strongly affected in *Satb2*$^{V234L/+}$ compared to *Satb2*^{WT} mice of both genders. We found that the statistically decreased body weight, fat mass and lean mass in *Satb2*$^{V234L/+}$ mice compared to wild-type mice became even more noticeable over time. The reduced fat content in male *Satb2*$^{V234L/+}$ mice was more significant when mice were eleven weeks of age or older. These observations were consistent with the linear regression analysis results, which suggested that the decreased body weight in *Satb2*$^{V234L/+}$ mice was primarily due to a reduction in body fat mass rather than lean mass. This conclusion is in line with the reduced size of adipocytes observed in *Satb2*$^{V234L/+}$ mice. Moreover, decreased bone mineral and bone density in *Satb2*$^{V234L/+}$ mice may possibly be attributable to a different body weight. However, lean mass – not fat mass - is considered as a predictor of bone mass to represent the associations between adipose tissue and bone[278,279].

Another possible explanation for the reduced body weight is reduced food intake. On the basis that the brittle teeth of the mutant mice may affect food intake, food consumption measurements were in first experiments performed in female mice fed with powder diet food. We demonstrated that the changes in body weight and fat mass were not due to food consumption. Monitoring of food intake during the indirect calorimetry measurements supported this conclusion for both male and female mice. However, it’s difficult for us to explain the disappearance of significant body weight difference between the two groups during the age of seven to ten weeks. Therefore, we concluded that it was not a dietary response that resulted in body weight-related phenotypes in *Satb2*$^{V234L/+}$ mice.

The maintenance in body weight results from a stable balance between food intake and energy expenditure[174]. As energy expenditure is generally composed of basal metabolic expenditure and physical activity expenditure[280], we produced a formula of energy homeostasis, as follows:

Body weight = Food intake - basal metabolic expenditure - physical activity expenditure

Our data clearly indicate that *Satb2*$^{V234L/+}$ mice are leaner whilst consuming a similar quantity of food compared to *Satb2*^{WT} mice. Previous GMC results revealed no significant difference in physical activities between the two groups. So we supposed that *Satb2*$^{V234L/+}$ mice have a higher basal metabolic rate compared to *Satb2*^{WT} mice.

The optimal strategy to determine basal energy expenditure in mice is indirect calorimetry measurement[281,282]. Oxygen consumption and the calculation of the respiratory exchange ratio (RER) reflect energy expenditure[283] and basal substrates for oxidation[284]. Surprisingly, *Satb2*$^{V234L/+}$ mice showed significantly decreased absolute VO_2 levels compared to *Satb2*^{WT} mice in two measurements, which suggested reduced energy expenditure even though this is normally associated with a higher body weight[285,286]. In addition, no significant effects on the mean RER were detected between the genotypes in two measurements, as well as in mean distance and mean rearing. Since fat tissue and lean tissue have different metabolic rates and the metabolic activity of fat tissue is approximately 15-25% of that of lean tissue in mice[287], it is necessary to normalize the data with fat mass and lean mass when analyzing calorimetry data[288]. We therefore used the linear model *'lean mass + (0.2×fat mass)*[288,289] to adjust the data. No clear differences were observed between the two genotypes (data not shown). But, a genotype effect was observed when the data were analyzed by using the analysis of covariance (ANCOVA) and included lean mass and fat mass as covariates[290,291]. Still, we could not explain the opposite observations made in the measurements of mice of two different ages: *Satb2*$^{V234L/+}$ mice showed lower VO_2 expenditure at the age of ten weeks but higher VO_2 expenditure at the age of sixteen weeks. Generally, measurements of energy metabolism should be performed over several days and should include several variable factors, such as temperature, pressure, humidity and so on[288,292]. Since our measurements were only performed for 16 hours at two age-points, we suggest to repeat this screen with longer measurements including more parameters at multiple age-points.

To our knowledge, there is no previous report on browning and metabolic phenotypes associated with SATB2 function. Transformation from white adipocytes into brite adipocytes has been well founded to be stimulated by cold exposure and β3-adrenergic agonists[64]. Since cold activation or similar metabolic phenotypes were not observed in mice treated with β3-adrenergic receptors agonists (β3-ARs)[293,294], we likewise suggest that β-adrenergic receptors might be activated in *Satb2*$^{V234L/+}$ mice. The function of β3-ARs on energy expenditure was found to be mainly controlled by the sympathetic nervous system in the brain[295]. Mainly, the regulation of body weight and energy homeostasis is performed by distinct nuclei localized in the hypothalamus. Furthermore, cell in the hypothalamus (paraventricular nucleus, lateral hypothalamus and arcuate nucleus) were found to be involved in the regulation of brown adipocytes[296]. Interestingly, *Satb2* is found to be specifically expressed in these areas of certain neuron development[125]. How SATB2 acts to stimulate the recruitment of sympathetic nerves to white adipose tissue is unknown. Therefore, we speculate that SATB2 mediates recruitment of browning white adipocytes and modulates energy metabolism via a hypothalamic and β3-adrenergic receptor pathway. However, it is still not clear whether the observed browning white adipocytes in $Satb2^{V234L/+}$ mice are classical or atypical brown adipocytes. Additional metabolic analyses of the $Satb2^{V234L/+}$ mice have to be performed to answer these questions.

5.2 The *Dll1*^{T720A} mouse line

The highly evolutionarily conserved Notch signaling pathway regulates cell developmental decisions by cell-to-cell interactions between receptors and ligands. DLL1 (Delta-like 1) belongs to the Delta/Serrate/LAG-2 (DSL) ligand family, which can interact with Notch receptors on adjacent cells[138]. DLL1 function has been reported to be necessary for early developmental processes such as somitogenesis, left-right axis formation, neurogenesis and pancreas formation[185,297-300]. Mice that are heterozygous for a *Dll1*^{LacZ} loss-of-function allele depict a haploinsufficient phenotype affecting immunological and metabolic processes[183]. Moreover, a possible role of *Dll1* in the homeostasis of the adult pancreas has been described in the frame of a previous PhD work in β-cell specific *Dll1* knockdown mice (see PhD thesis by Dr. Davide Cavanna).

When homozygous *Dll1*^{T720A} mutant mice were investigated for the first time in the German Mouse Clinic (GMC) no age-matched wild-type littermates were available. Instead, all measured parameters of this preliminary screening were compared to C3HeB/FeJ wild-type mice. Compared to these wild-type mice homozygous *Dll1*^{T720A} mice expressed alterations mainly in body weight, size, body composition as well as the skeleton. *Dll1*$^{T720A/-}$ mice were smaller, leaner, with reduced bone mineral density and fat content, and showd an increased locomotor activity, and are somewhat in line with *Dll1*$^{LacZ/+}$ mice regarding body weight and alterations in clinical chemical parameters[301].

Therefore, to confirm the phenotypes exhibited in *Dll1*$^{T720A/-}$ mice selected screens were repeated with a second cohort of *Dll1*$^{T720A/-}$ mice, this time together with real wild-type littermates. In contrast to the preliminary findings mentioned above, only transient differences were observed between *Dll1*$^{T720A/-}$ mutants and wild-type littermates. For example, differences in the body composition were observed only in male *Dll1*$^{T720A/-}$ mice, especially at the age of thirty-two weeks. Likewise, only a few skeletal parameters showed slight significant changes in *Dll1*$^{T720A/-}$ mice compared with *Dll1*^{WT} mice.

A role for Notch signaling in early bone development has been demonstrated[302,303] and its function during bone homeostasis discussed[304,305]. But less is known about the role of the Notch ligand DLL1 and in particular of its intracellular domain in these processes. Recently, our and other labs demonstrated that the DLL1 intracellular domain (DICD) is able to interact via its C-terminal PDZ-binding motif with PDZ-domain containing proteins[306-309], which are scaffolding proteins that assemble intracellular multi-protein signaling complexes[306,310]. Biochemical analyses demonstrated that the amino acid exchange existing in the PDZ binding motif of DLL1 in *Dll1*$^{T720A/-}$ mice is no longer able to interact with the PDZ protein MAGI2 (Gerhard Przemeck, personal communication). Interestingly, mice hemizygous for a loss-of-function (*LacZ)* and the *T720A* allele of *Dll1* show a clear short-tail phenotype and skeletal defects along the entire body axis (Gerhard Przemeck, personal communication) that do not appear in heterozygous *Dll1*$^{LacZ/+}$ nor in homozygous *Dll1*$^{T720A/-}$ mice, respectively. Although this finding confirms a function of the DLL1 PDZ-binding motif it does not point to any molecular mechanisms involving DLL1-dependent PDZ interactions. So, further experiments are required.

The repeated measurements with the second cohort of *Dll1*$^{T720/-}$ mice together with real wild-type littermates could not reproduce the findings that were made when *Dll1*$^{T720/-}$ mice were at first compared to wild-type mice from another ENU-generated *Dll1* mouse line. Both mouse lines originate independently from each other from two different F1-founder animals and might be varyingly often backcrossed to C3HeB/FeJ wild-type mice. So, it is thinkable that, although on the same genetic background, genomic differences between the two wild-type cohorts may have existed. Another possibility might be that mutant and wild-type mice from the first round of measurements were bred in different animal facilities.

In conclusion, homozygous *Dll1*$^{T720/-}$ mice showed under the tested conditions no phenotype regarding the bone, body composition and energy expenditure. However, taking the already known metabolic changes found in haploinsufficient *Dll1*$^{LacZ/+}$ mice into account, future experiments might also include high-fat diet challenged *Dll1*$^{T720A/-}$ mice.

6. References

1. Downey, P.A. & Siegel, M.I. Bone biology and the clinical implications for osteoporosis. *Phys Ther* **86**, 77-91 (2006).
2. Buckwalter, J.A., Glimcher, M.J., Cooper, R.R. & Recker, R. Bone biology. I: Structure, blood supply, cells, matrix, and mineralization. *Instr Course Lect* **45**, 371-86 (1996).
3. Fan, X. & Tang, L. Aberrant and alternative splicing in skeletal system disease. *Gene* **528**, 21-6 (2013).
4. Kim, Y.K. *et al.* Tooth-derived bone graft material. *J Korean Assoc Oral Maxillofac Surg* **39**, 103-111 (2013).
5. Benjamin, M., Kaiser, E. & Milz, S. Structure-function relationships in tendons: a review. *J Anat* **212**, 211-28 (2008).
6. Fliedner, T.M. The role of blood stem cells in hematopoietic cell renewal. *Stem Cells* **16 Suppl 1**, 13-29 (1998).
7. Feng, J.Q., Clinkenbeard, E.L., Yuan, B., White, K.E. & Drezner, M.K. Osteocyte regulation of phosphate homeostasis and bone mineralization underlies the pathophysiology of the heritable disorders of rickets and osteomalacia. *Bone* **54**, 213-21 (2013).
8. Guntur, A.R. & Rosen, C.J. Bone as an endocrine organ. *Endocr Pract* **18**, 758-62 (2012).
9. Olsen, B.R., Reginato, A.M. & Wang, W. Bone development. *Annu Rev Cell Dev Biol* **16**, 191-220 (2000).
10. Dodds, R.A. *et al.* Human osteoclasts, not osteoblasts, deposit osteopontin onto resorption surfaces: an in vitro and ex vivo study of remodeling bone. *J Bone Miner Res* **10**, 1666-80 (1995).
11. Nishimura, R. *et al.* Signal transduction and transcriptional regulation during mesenchymal cell differentiation. *J Bone Miner Metab* **26**, 203-12 (2008).
12. Kronenberg, H.M. Developmental regulation of the growth plate. *Nature* **423**, 332-6 (2003).
13. Zou, H., Choe, K.M., Lu, Y., Massague, J. & Niswander, L. BMP signaling and vertebrate limb development. *Cold Spring Harb Symp Quant Biol* **62**, 269-72 (1997).
14. Shum, L., Wang, X., Kane, A.A. & Nuckolls, G.H. BMP4 promotes chondrocyte proliferation and hypertrophy in the endochondral cranial base. *Int J Dev Biol* **47**, 423-31 (2003).
15. Matsubara, T. *et al.* BMP2 regulates Osterix through Msx2 and Runx2 during osteoblast differentiation. *J Biol Chem* **283**, 29119-25 (2008).
16. Cohen, M.M., Jr. The new bone biology: pathologic, molecular, and clinical correlates. *Am J Med Genet A* **140**, 2646-706 (2006).
17. Udagawa, N. *et al.* Osteoprotegerin produced by osteoblasts is an important regulator in osteoclast development and function. *Endocrinology* **141**, 3478-84 (2000).
18. Phan, T.C., Xu, J. & Zheng, M.H. Interaction between osteoblast and osteoclast: impact in bone disease. *Histol Histopathol* **19**, 1325-44 (2004).
19. Horowitz, M.C., Bothwell, A.L., Hesslein, D.G., Pflugh, D.L. & Schatz, D.G. B cells and osteoblast and osteoclast development. *Immunol Rev* **208**, 141-53 (2005).
20. Ducy, P. *et al.* Increased bone formation in osteocalcin-deficient mice. *Nature* **382**, 448-52 (1996).
21. Nakamura, A. *et al.* Osteocalcin secretion as an early marker of in vitro osteogenic differentiation of rat mesenchymal stem cells. *Tissue Eng Part C Methods* **15**, 169-80 (2009).
22. Khoshniat, S. *et al.* Phosphate-dependent stimulation of MGP and OPN expression in osteoblasts via the ERK1/2 pathway is modulated by calcium. *Bone* **48**, 894-902 (2011).
23. Romagnoli, E. *et al.* Assessment of serum total and bone alkaline phosphatase measurement in clinical practice. *Clin Chem Lab Med* **36**, 163-8 (1998).

24. Hessle, L. *et al.* Tissue-nonspecific alkaline phosphatase and plasma cell membrane glycoprotein-1 are central antagonistic regulators of bone mineralization. *Proc Natl Acad Sci U S A* **99**, 9445-9 (2002).
25. Zhang, X., Aubin, J.E. & Inman, R.D. Molecular and cellular biology of new bone formation: insights into the ankylosis of ankylosing spondylitis. *Curr Opin Rheumatol* **15**, 387-93 (2003).
26. Bonewald, L. Osteocytes as multifunctional cells. *J Musculoskelet Neuronal Interact* **6**, 331-3 (2006).
27. Jiang, Y., Mehta, C.K., Hsu, T.Y. & Alsulaimani, F.F. Bacteria induce osteoclastogenesis via an osteoblast-independent pathway. *Infect Immun* **70**, 3143-8 (2002).
28. Chambers, T.J. Regulation of the differentiation and function of osteoclasts. *J Pathol* **192**, 4-13 (2000).
29. Roodman, G.D. Advances in bone biology: the osteoclast. *Endocr Rev* **17**, 308-32 (1996).
30. Manolagas, S.C. Birth and death of bone cells: basic regulatory mechanisms and implications for the pathogenesis and treatment of osteoporosis. *Endocr Rev* **21**, 115-37 (2000).
31. Zhao, B. & Ivashkiv, L.B. Negative regulation of osteoclastogenesis and bone resorption by cytokines and transcriptional repressors. *Arthritis Res Ther* **13**, 234 (2011).
32. Diez, J. *et al.* Serum markers of collagen type I metabolism in spontaneously hypertensive rats: relation to myocardial fibrosis. *Circulation* **93**, 1026-32 (1996).
33. Hannon, R.A. & Eastell, R. Biochemical markers of bone turnover and fracture prediction. *J Br Menopause Soc* **9**, 10-5 (2003).
34. Barrere, F., van Blitterswijk, C.A. & de Groot, K. Bone regeneration: molecular and cellular interactions with calcium phosphate ceramics. *Int J Nanomedicine* **1**, 317-32 (2006).
35. Kapinas, K. & Delany, A.M. MicroRNA biogenesis and regulation of bone remodeling. *Arthritis Res Ther* **13**, 220 (2011).
36. Hadjidakis, D.J. & Androulakis, II. Bone remodeling. *Ann N Y Acad Sci* **1092**, 385-96 (2006).
37. Mundy, G.R. & Guise, T.A. Hormonal control of calcium homeostasis. *Clin Chem* **45**, 1347-52 (1999).
38. Pacifici, R. Cytokines, estrogen, and postmenopausal osteoporosis--the second decade. *Endocrinology* **139**, 2659-61 (1998).
39. Lorenzo, J. Interactions between immune and bone cells: new insights with many remaining questions. *J Clin Invest* **106**, 749-52 (2000).
40. Hsu, H. *et al.* Tumor necrosis factor receptor family member RANK mediates osteoclast differentiation and activation induced by osteoprotegerin ligand. *Proc Natl Acad Sci U S A* **96**, 3540-5 (1999).
41. Yasuda, H. *et al.* Osteoclast differentiation factor is a ligand for osteoprotegerin/osteoclastogenesis-inhibitory factor and is identical to TRANCE/RANKL. *Proc Natl Acad Sci U S A* **95**, 3597-602 (1998).
42. Simonet, W.S. *et al.* Osteoprotegerin: a novel secreted protein involved in the regulation of bone density. *Cell* **89**, 309-19 (1997).
43. Bartlett, J.D. Dental Enamel Development: Proteinases and Their Enamel Matrix Substrates. *ISRN Dent* **2013**, 684607 (2013).
44. Thesleff, I. Epithelial-mesenchymal signalling regulating tooth morphogenesis. *J Cell Sci* **116**, 1647-8 (2003).
45. Mitsiadis, T.A. *et al.* Expression of the transcription factors Otlx2, Barx1 and Sox9 during mouse odontogenesis. *Eur J Oral Sci* **106 Suppl 1**, 112-6 (1998).
46. Yamashiro, T., Aberg, T., Levanon, D., Groner, Y. & Thesleff, I. Expression of Runx1, -2 and -3 during tooth, palate and craniofacial bone development. *Mech Dev* **119 Suppl 1**, S107-10 (2002).
47. Hu, J.C., Chun, Y.H., Al Hazzazzi, T. & Simmer, J.P. Enamel formation and amelogenesis imperfecta. *Cells Tissues Organs* **186**, 78-85 (2007).

48. Lagerstrom, M. *et al.* A deletion in the amelogenin gene (AMG) causes X-linked amelogenesis imperfecta (AIH1). *Genomics* **10**, 971-5 (1991).
49. Rajpar, M.H., Harley, K., Laing, C., Davies, R.M. & Dixon, M.J. Mutation of the gene encoding the enamel-specific protein, enamelin, causes autosomal-dominant amelogenesis imperfecta. *Hum Mol Genet* **10**, 1673-7 (2001).
50. Kim, J.W. *et al.* MMP-20 mutation in autosomal recessive pigmented hypomaturation amelogenesis imperfecta. *J Med Genet* **42**, 271-5 (2005).
51. Hart, P.S. *et al.* Mutation in kallikrein 4 causes autosomal recessive hypomaturation amelogenesis imperfecta. *J Med Genet* **41**, 545-9 (2004).
52. Parry, D.A. *et al.* Identification of mutations in SLC24A4, encoding a potassium-dependent sodium/calcium exchanger, as a cause of amelogenesis imperfecta. *Am J Hum Genet* **92**, 307-12 (2013).
53. Poulter, J.A. *et al.* Whole-exome sequencing, without prior linkage, identifies a mutation in LAMB3 as a cause of dominant hypoplastic amelogenesis imperfecta. *Eur J Hum Genet* **22**, 132-5 (2014).
54. Kim, J.W. *et al.* Mutational analysis of candidate genes in 24 amelogenesis imperfecta families. *Eur J Oral Sci* **114 Suppl 1**, 3-12; discussion 39-41, 379 (2006).
55. Kershaw, E.E. & Flier, J.S. Adipose tissue as an endocrine organ. *J Clin Endocrinol Metab* **89**, 2548-56 (2004).
56. Cinti, S. The adipose organ. *Prostaglandins Leukot Essent Fatty Acids* **73**, 9-15 (2005).
57. Galic, S., Oakhill, J.S. & Steinberg, G.R. Adipose tissue as an endocrine organ. *Mol Cell Endocrinol* **316**, 129-39 (2010).
58. Frontini, A. & Cinti, S. Distribution and development of brown adipocytes in the murine and human adipose organ. *Cell Metab* **11**, 253-6 (2010).
59. Lee, P. *et al.* Irisin and FGF21 are cold-induced endocrine activators of brown fat function in humans. *Cell Metab* **19**, 302-9 (2014).
60. Ravussin, Y., Xiao, C., Gavrilova, O. & Reitman, M.L. Effect of intermittent cold exposure on brown fat activation, obesity, and energy homeostasis in mice. *PLoS One* **9**, e85876 (2014).
61. Bonet, M.L., Oliver, P. & Palou, A. Pharmacological and nutritional agents promoting browning of white adipose tissue. *Biochim Biophys Acta* **1831**, 969-85 (2013).
62. Lidell, M.E. *et al.* Evidence for two types of brown adipose tissue in humans. *Nat Med* **19**, 631-4 (2013).
63. Wang, Q.A., Tao, C., Gupta, R.K. & Scherer, P.E. Tracking adipogenesis during white adipose tissue development, expansion and regeneration. *Nat Med* **19**, 1338-44 (2013).
64. Harms, M. & Seale, P. Brown and beige fat: development, function and therapeutic potential. *Nat Med* **19**, 1252-63 (2013).
65. Himms-Hagen, J. *et al.* Multilocular fat cells in WAT of CL-316243-treated rats derive directly from white adipocytes. *Am J Physiol Cell Physiol* **279**, C670-81 (2000).
66. Petrovic, N. *et al.* Chronic peroxisome proliferator-activated receptor gamma (PPARgamma) activation of epididymally derived white adipocyte cultures reveals a population of thermogenically competent, UCP1-containing adipocytes molecularly distinct from classic brown adipocytes. *J Biol Chem* **285**, 7153-64 (2010).
67. Cristancho, A.G. & Lazar, M.A. Forming functional fat: a growing understanding of adipocyte differentiation. *Nat Rev Mol Cell Biol* **12**, 722-34 (2011).
68. Rosen, E.D. & MacDougald, O.A. Adipocyte differentiation from the inside out. *Nat Rev Mol Cell Biol* **7**, 885-96 (2006).
69. Kirtland, J. & Harris, P.M. Changes in adipose tissue of the rat due early undernutrition followed by rehabilitation. 3. Changes in cell replication studied with tritiated thymidine. *Br J Nutr* **43**, 33-43 (1980).
70. Lemonnier, D. Effect of age, sex, and sites on the cellularity of the adipose tissue in mice and rats rendered obese by a high-fat diet. *J Clin Invest* **51**, 2907-15 (1972).

71. Astrup, A., Bulow, J., Madsen, J. & Christensen, N.J. Contribution of BAT and skeletal muscle to thermogenesis induced by ephedrine in man. *Am J Physiol* **248**, E507-15 (1985).
72. Cinti, S. Transdifferentiation properties of adipocytes in the adipose organ. *Am J Physiol Endocrinol Metab* **297**, E977-86 (2009).
73. Wu, J. *et al.* Beige adipocytes are a distinct type of thermogenic fat cell in mouse and human. *Cell* **150**, 366-76 (2012).
74. Green, H. & Meuth, M. An established pre-adipose cell line and its differentiation in culture. *Cell* **3**, 127-33 (1974).
75. Gregoire, F., Todoroff, G., Hauser, N. & Remacle, C. The stroma-vascular fraction of rat inguinal and epididymal adipose tissue and the adipoconversion of fat cell precursors in primary culture. *Biol Cell* **69**, 215-22 (1990).
76. Otto, T.C. & Lane, M.D. Adipose development: from stem cell to adipocyte. *Crit Rev Biochem Mol Biol* **40**, 229-42 (2005).
77. Dispirito, J.R., Fang, B., Wang, F. & Lazar, M.A. Pruning of the adipocyte peroxisome proliferator-activated receptor gamma cistrome by hematopoietic master regulator PU.1. *Mol Cell Biol* **33**, 3354-64 (2013).
78. Cipolletta, D. *et al.* PPAR-gamma is a major driver of the accumulation and phenotype of adipose tissue Treg cells. *Nature* **486**, 549-53 (2012).
79. Tang, Q.Q. *et al.* Sequential phosphorylation of CCAAT enhancer-binding protein beta by MAPK and glycogen synthase kinase 3beta is required for adipogenesis. *Proc Natl Acad Sci U S A* **102**, 9766-71 (2005).
80. Karamanlidis, G., Karamitri, A., Docherty, K., Hazlerigg, D.G. & Lomax, M.A. C/EBPbeta reprograms white 3T3-L1 preadipocytes to a Brown adipocyte pattern of gene expression. *J Biol Chem* **282**, 24660-9 (2007).
81. Sun, L. & Trajkovski, M. MiR-27 orchestrates the transcriptional regulation of brown adipogenesis. *Metabolism* **63**, 272-82 (2014).
82. Liu, W. *et al.* miR-133a regulates adipocyte browning in vivo. *PLoS Genet* **9**, e1003626 (2013).
83. Chen, Y. *et al.* miR-155 regulates differentiation of brown and beige adipocytes via a bistable circuit. *Nat Commun* **4**, 1769 (2013).
84. Hall, K.D. *et al.* Energy balance and its components: implications for body weight regulation. *Am J Clin Nutr* **95**, 989-94 (2012).
85. Badman, M.K. & Flier, J.S. The adipocyte as an active participant in energy balance and metabolism. *Gastroenterology* **132**, 2103-15 (2007).
86. Flier, J.S. & Maratos-Flier, E. Obesity and the hypothalamus: novel peptides for new pathways. *Cell* **92**, 437-40 (1998).
87. Wolfgang, M.J. & Lane, M.D. Control of energy homeostasis: role of enzymes and intermediates of fatty acid metabolism in the central nervous system. *Annu Rev Nutr* **26**, 23-44 (2006).
88. Rosen, E.D. & Spiegelman, B.M. Adipocytes as regulators of energy balance and glucose homeostasis. *Nature* **444**, 847-53 (2006).
89. Zhang, Y. *et al.* Positional cloning of the mouse obese gene and its human homologue. *Nature* **372**, 425-32 (1994).
90. Considine, R.V. *et al.* Serum immunoreactive-leptin concentrations in normal-weight and obese humans. *N Engl J Med* **334**, 292-5 (1996).
91. Friedman, J.M. & Halaas, J.L. Leptin and the regulation of body weight in mammals. *Nature* **395**, 763-70 (1998).
92. Leshan, R.L., Bjornholm, M., Munzberg, H. & Myers, M.G., Jr. Leptin receptor signaling and action in the central nervous system. *Obesity (Silver Spring)* **14 Suppl 5**, 208S-212S (2006).
93. Fruebis, J. *et al.* Proteolytic cleavage product of 30-kDa adipocyte complement-related protein increases fatty acid oxidation in muscle and causes weight loss in mice. *Proc Natl Acad Sci U S A* **98**, 2005-10 (2001).

94. Yamauchi, T. *et al.* The fat-derived hormone adiponectin reverses insulin resistance associated with both lipoatrophy and obesity. *Nat Med* **7**, 941-6 (2001).
95. Berg, A.H., Combs, T.P., Du, X., Brownlee, M. & Scherer, P.E. The adipocyte-secreted protein Acrp30 enhances hepatic insulin action. *Nat Med* **7**, 947-53 (2001).
96. Noguchi, R. *et al.* The selective control of glycolysis, gluconeogenesis and glycogenesis by temporal insulin patterns. *Mol Syst Biol* **9**, 664 (2013).
97. Koch, L. *et al.* Central insulin action regulates peripheral glucose and fat metabolism in mice. *J Clin Invest* **118**, 2132-47 (2008).
98. Saladin, R. *et al.* Transient increase in obese gene expression after food intake or insulin administration. *Nature* **377**, 527-9 (1995).
99. Rentsch, J. & Chiesi, M. Regulation of ob gene mRNA levels in cultured adipocytes. *FEBS Lett* **379**, 55-9 (1996).
100. Petersen, K.F. *et al.* Leptin reverses insulin resistance and hepatic steatosis in patients with severe lipodystrophy. *J Clin Invest* **109**, 1345-50 (2002).
101. Tishinsky, J.M., Robinson, L.E. & Dyck, D.J. Insulin-sensitizing properties of adiponectin. *Biochimie* **94**, 2131-6 (2012).
102. Fasshauer, M. *et al.* Growth hormone is a positive regulator of adiponectin receptor 2 in 3T3-L1 adipocytes. *FEBS Lett* **558**, 27-32 (2004).
103. Dulloo, A.G. & Montani, J.P. Body composition, inflammation and thermogenesis in pathways to obesity and the metabolic syndrome: an overview. *Obes Rev* **13 Suppl 2**, 1-5 (2012).
104. Apovian, C.M. *et al.* Adipose macrophage infiltration is associated with insulin resistance and vascular endothelial dysfunction in obese subjects. *Arterioscler Thromb Vasc Biol* **28**, 1654-9 (2008).
105. Hariri, N. & Thibault, L. High-fat diet-induced obesity in animal models. *Nutr Res Rev* **23**, 270-99 (2010).
106. Greenberg, A.S. & Obin, M.S. Obesity and the role of adipose tissue in inflammation and metabolism. *Am J Clin Nutr* **83**, 461S-465S (2006).
107. Page, A. *et al.* Physical activity patterns in nonobese and obese children assessed using minute-by-minute accelerometry. *Int J Obes (Lond)* **29**, 1070-6 (2005).
108. Hotamisligil, G.S., Arner, P., Caro, J.F., Atkinson, R.L. & Spiegelman, B.M. Increased adipose tissue expression of tumor necrosis factor-alpha in human obesity and insulin resistance. *J Clin Invest* **95**, 2409-15 (1995).
109. Shimomura, I., Hammer, R.E., Ikemoto, S., Brown, M.S. & Goldstein, J.L. Leptin reverses insulin resistance and diabetes mellitus in mice with congenital lipodystrophy. *Nature* **401**, 73-6 (1999).
110. Kadowaki, T. *et al.* Adiponectin and adiponectin receptors in insulin resistance, diabetes, and the metabolic syndrome. *J Clin Invest* **116**, 1784-92 (2006).
111. Cornier, M.A. *et al.* The metabolic syndrome. *Endocr Rev* **29**, 777-822 (2008).
112. Ducy, P. *et al.* Leptin inhibits bone formation through a hypothalamic relay: a central control of bone mass. *Cell* **100**, 197-207 (2000).
113. Tu, Q. *et al.* Adiponectin inhibits osteoclastogenesis and bone resorption via APPL1-mediated suppression of Akt1. *J Biol Chem* **286**, 12542-53 (2011).
114. Breuil, V. *et al.* Oxytocin and bone remodelling: relationships with neuropituitary hormones, bone status and body composition. *Joint Bone Spine* **78**, 611-5 (2011).
115. Coen, G. *et al.* Serum leptin in dialysis renal osteodystrophy. *Am J Kidney Dis* **42**, 1036-42 (2003).
116. Lee, N.K. *et al.* Endocrine regulation of energy metabolism by the skeleton. *Cell* **130**, 456-69 (2007).
117. Ferron, M., Hinoi, E., Karsenty, G. & Ducy, P. Osteocalcin differentially regulates beta cell and adipocyte gene expression and affects the development of metabolic diseases in wild-type mice. *Proc Natl Acad Sci U S A* **105**, 5266-70 (2008).

118. Ferron, M. *et al.* Insulin signaling in osteoblasts integrates bone remodeling and energy metabolism. *Cell* **142**, 296-308 (2010).
119. Hill, H.S. *et al.* Carboxylated and Uncarboxylated Forms of Osteocalcin Directly Modulate the Glucose Transport System and Inflammation in Adipocytes. *Horm Metab Res* (2014).
120. Dobreva, G., Dambacher, J. & Grosschedl, R. SUMO modification of a novel MAR-binding protein, SATB2, modulates immunoglobulin mu gene expression. *Genes Dev* **17**, 3048-61 (2003).
121. Ahn, H.J. *et al.* The expression profile and function of Satb2 in zebrafish embryonic development. *Mol Cells* **30**, 377-82 (2010).
122. Sheehan-Rooney, K., Swartz, M.E., Lovely, C.B., Dixon, M.J. & Eberhart, J.K. Bmp and Shh signaling mediate the expression of satb2 in the pharyngeal arches. *PLoS One* **8**, e59533 (2013).
123. FitzPatrick, D.R. *et al.* Identification of SATB2 as the cleft palate gene on 2q32-q33. *Hum Mol Genet* **12**, 2491-501 (2003).
124. Dobreva, G. *et al.* SATB2 is a multifunctional determinant of craniofacial patterning and osteoblast differentiation. *Cell* **125**, 971-86 (2006).
125. Huang, Y. *et al.* Expression of transcription factor Satb2 in adult mouse brain. *Anat Rec (Hoboken)* **296**, 452-61 (2013).
126. Magnusson, K. *et al.* SATB2 in combination with cytokeratin 20 identifies over 95% of all colorectal carcinomas. *Am J Surg Pathol* **35**, 937-48 (2011).
127. Zhao, X. *et al.* The role of SATB2 in skeletogenesis and human disease. *Cytokine Growth Factor Rev* **25**, 35-44 (2014).
128. Dragomir, A., de Wit, M., Johansson, C., Uhlen, M. & Ponten, F. The role of SATB2 as a diagnostic marker for tumors of colorectal origin: Results of a pathology-based clinical prospective study. *Am J Clin Pathol* **141**, 630-8 (2014).
129. Han, K., Dou, F.M., Zhang, L.J. & Zhu, B.P. [Compliance on hand-hygiene among healthcare providers working at secondary and tertiary general hospitals in Chengdu]. *Zhonghua Liu Xing Bing Xue Za Zhi* **32**, 1139-42 (2011).
130. Wang, S. *et al.* Down-regulated expression of SATB2 is associated with metastasis and poor prognosis in colorectal cancer. *J Pathol* **219**, 114-22 (2009).
131. Hassan, M.Q. *et al.* A network connecting Runx2, SATB2, and the miR-23a~27a~24-2 cluster regulates the osteoblast differentiation program. *Proc Natl Acad Sci U S A* **107**, 19879-84 (2010).
132. Wei, J. *et al.* miR-34s inhibit osteoblast proliferation and differentiation in the mouse by targeting SATB2. *J Cell Biol* **197**, 509-21 (2012).
133. Ellies, D.L. & Krumlauf, R. Bone formation: The nuclear matrix reloaded. *Cell* **125**, 840-2 (2006).
134. Britanova, O. *et al.* Satb2 haploinsufficiency phenocopies 2q32-q33 deletions, whereas loss suggests a fundamental role in the coordination of jaw development. *Am J Hum Genet* **79**, 668-78 (2006).
135. Leoyklang, P. *et al.* Heterozygous nonsense mutation SATB2 associated with cleft palate, osteoporosis, and cognitive defects. *Hum Mutat* **28**, 732-8 (2007).
136. Rosenfeld, J.A. *et al.* Small deletions of SATB2 cause some of the clinical features of the 2q33.1 microdeletion syndrome. *PLoS One* **4**, e6568 (2009).
137. Augustin, M. *et al.* Efficient and fast targeted production of murine models based on ENU mutagenesis. *Mamm Genome* **16**, 405-13 (2005).
138. Artavanis-Tsakonas, S., Rand, M.D. & Lake, R.J. Notch signaling: cell fate control and signal integration in development. *Science* **284**, 770-6 (1999).
139. Andersson, E.R., Sandberg, R. & Lendahl, U. Notch signaling: simplicity in design, versatility in function. *Development* **138**, 3593-612 (2011).

140. Aster, J.C., Pear, W.S. & Blacklow, S.C. Notch signaling in leukemia. *Annu Rev Pathol* **3**, 587-613 (2008).
141. Penton, A.L., Leonard, L.D. & Spinner, N.B. Notch signaling in human development and disease. *Semin Cell Dev Biol* **23**, 450-7 (2012).
142. Fukuda, D. *et al.* Notch ligand delta-like 4 blockade attenuates atherosclerosis and metabolic disorders. *Proc Natl Acad Sci U S A* **109**, E1868-77 (2012).
143. Roh, M.H. & Margolis, B. Composition and function of PDZ protein complexes during cell polarization. *Am J Physiol Renal Physiol* **285**, F377-87 (2003).
144. Kamoun-Goldrat, A.S. & Le Merrer, M.F. Animal models of osteogenesis imperfecta and related syndromes. *J Bone Miner Metab* **25**, 211-8 (2007).
145. Katz, S. & Weinerman, S. Osteoporosis and gastrointestinal disease. *Gastroenterol Hepatol (N Y)* **6**, 506-17 (2010).
146. Hrabe de Angelis, M.H. *et al.* Genome-wide, large-scale production of mutant mice by ENU mutagenesis. *Nat Genet* **25**, 444-7 (2000).
147. Nicklas, W. *et al.* Recommendations for the health monitoring of rodent and rabbit colonies in breeding and experimental units. *Lab Anim* **36**, 20-42 (2002).
148. Spinsanti, G. *et al.* Selection of reference genes for quantitative RT-PCR studies in striped dolphin (Stenella coeruleoalba) skin biopsies. *BMC Mol Biol* **7**, 32 (2006).
149. Pfaffl, M.W. A new mathematical model for relative quantification in real-time RT-PCR. *Nucleic Acids Res* **29**, e45 (2001).
150. Fuchs, H. *et al.* Phenotypic characterization of mouse models for bone-related diseases in the German Mouse Clinic. *J Musculoskelet Neuronal Interact* **8**, 13-4 (2008).
151. Fuchs, H., Schughart, K., Wolf, E., Balling, R. & Hrabe de Angelis, M. Screening for dysmorphological abnormalities--a powerful tool to isolate new mouse mutants. *Mamm Genome* **11**, 528-30 (2000).
152. Fuchs, H. *et al.* Mouse phenotyping. *Methods* **53**, 120-35 (2011).
153. Rathkolb, B. *et al.* The clinical-chemical screen in the Munich ENU Mouse Mutagenesis Project: screening for clinically relevant phenotypes. *Mamm Genome* **11**, 543-6 (2000).
154. Galgani, J. & Ravussin, E. Energy metabolism, fuel selection and body weight regulation. *Int J Obes (Lond)* **32 Suppl 7**, S109-19 (2008).
155. Patrick, C.E. & Nachiket, A.N. Indirect calorimetry in laboratory mice and rats: principles, practical considerations, interpretation and perspectives. *Am J Physiol Regul Integr Comp Physiol* **303**, 459-476 (2012).
156. Haugen, H.A., Chan, L.N. & Li, F. Indirect calorimetry: a practical guide for clinicians. *Nutr Clin Pract* **22**, 377-88 (2007).
157. Gailus-Durner, V. *et al.* Systemic first-line phenotyping. *Methods Mol Biol* **530**, 463-509 (2009).
158. Neff, F. *et al.* Rapamycin extends murine lifespan but has limited effects on aging. *J Clin Invest* **123**, 3272-91 (2013).
159. Halldorsdottir, S., Carmody, J., Boozer, C.N., Leduc, C.A. & Leibel, R.L. Reproducibility and accuracy of body composition assessments in mice by dual energy x-ray absorptiometry and time domain nuclear magnetic resonance. *Int J Body Compos Res* **7**, 147-154 (2009).
160. Rathkolb, B. *et al.* Large-scale N-ethyl-N-nitrosourea mutagenesis of mice--from phenotypes to genes. *Exp Physiol* **85**, 635-44 (2000).
161. Ritchie, M.E., Dunning, M.J., Smith, M.L., Shi, W. & Lynch, A.G. BeadArray expression analysis using bioconductor. *PLoS Comput Biol* **7**, e1002276 (2011).
162. Rainer, J., Sanchez-Cabo, F., Stocker, G., Sturn, A. & Trajanoski, Z. CARMAweb: comprehensive R- and bioconductor-based web service for microarray data analysis. *Nucleic Acids Res* **34**, W498-503 (2006).
163. Benjamini, Y., Hochberg, Y. Controlling the False Discovery Rate: A Practical and Powerful Approach to Multiple Testing. (2005).

164. Ashburner, M. *et al.* Gene ontology: tool for the unification of biology. The Gene Ontology Consortium. *Nat Genet* **25**, 25-9 (2000).
165. Kanehisa, M., Goto, S., Sato, Y., Furumichi, M. & Tanabe, M. KEGG for integration and interpretation of large-scale molecular data sets. *Nucleic Acids Res* **40**, D109-14 (2012).
166. Shigemizu, D. *et al.* A practical method to detect SNVs and indels from whole genome and exome sequencing data. *Sci Rep* **3**, 2161 (2013).
167. Aigner, B. *et al.* Generation of ENU-induced mouse mutants with hypocholesterolemia: novel tools for dissecting plasma lipoprotein homeostasis. *Lipids* **42**, 731-7 (2007).
168. Martins, A.M. *et al.* The role of lipase and alpha-amylase in the degradation of starch/poly(epsilon-caprolactone) fiber meshes and the osteogenic differentiation of cultured marrow stromal cells. *Tissue Eng Part A* **15**, 295-305 (2009).
169. Wlazlo, N. *et al.* Iron metabolism is associated with adipocyte insulin resistance and plasma adiponectin: the Cohort on Diabetes and Atherosclerosis Maastricht (CODAM) study. *Diabetes Care* **36**, 309-15 (2013).
170. Raisz, L.G. Physiology and pathophysiology of bone remodeling. *Clin Chem* **45**, 1353-8 (1999).
171. Vandyke, K. *et al.* The tyrosine kinase inhibitor dasatinib dysregulates bone remodeling through inhibition of osteoclasts in vivo. *J Bone Miner Res* **25**, 1759-70 (2010).
172. Zhang, C. *et al.* Osteoblast-specific transcription factor Osterix increases vitamin D receptor gene expression in osteoblasts. *PLoS One* **6**, e26504 (2011).
173. Rolfe, D.F. & Brown, G.C. Cellular energy utilization and molecular origin of standard metabolic rate in mammals. *Physiol Rev* **77**, 731-58 (1997).
174. Wan, M. *et al.* Loss of Akt1 in mice increases energy expenditure and protects against diet-induced obesity. *Mol Cell Biol* **32**, 96-106 (2012).
175. Butler, A.A. & Kozak, L.P. A recurring problem with the analysis of energy expenditure in genetic models expressing lean and obese phenotypes. *Diabetes* **59**, 323-9 (2010).
176. Klaman, L.D. *et al.* Increased energy expenditure, decreased adiposity, and tissue-specific insulin sensitivity in protein-tyrosine phosphatase 1B-deficient mice. *Mol Cell Biol* **20**, 5479-89 (2000).
177. Barbatelli, G. *et al.* The emergence of cold-induced brown adipocytes in mouse white fat depots is determined predominantly by white to brown adipocyte transdifferentiation. *Am J Physiol Endocrinol Metab* **298**, E1244-53 (2010).
178. Yamauchi, T. *et al.* Globular adiponectin protected ob/ob mice from diabetes and ApoE-deficient mice from atherosclerosis. *J Biol Chem* **278**, 2461-8 (2003).
179. Nawrocki, A.R. *et al.* Mice lacking adiponectin show decreased hepatic insulin sensitivity and reduced responsiveness to peroxisome proliferator-activated receptor gamma agonists. *J Biol Chem* **281**, 2654-60 (2006).
180. Ryan, A.S. *et al.* Plasma adiponectin and leptin levels, body composition, and glucose utilization in adult women with wide ranges of age and obesity. *Diabetes Care* **26**, 2383-8 (2003).
181. Minami, A. *et al.* Increased insulin sensitivity and hypoinsulinemia in APS knockout mice. *Diabetes* **52**, 2657-65 (2003).
182. Teppner, I., Becker, S., de Angelis, M.H., Gossler, A. & Beckers, J. Compartmentalised expression of Delta-like 1 in epithelial somites is required for the formation of intervertebral joints. *BMC Dev Biol* **7**, 68 (2007).
183. Rubio-Aliaga, I. *et al.* Dll1 haploinsufficiency in adult mice leads to a complex phenotype affecting metabolic and immunological processes. *PLoS One* **4**, e6054 (2009).
184. Jensen, J. *et al.* Control of endodermal endocrine development by Hes-1. *Nat Genet* **24**, 36-44 (2000).
185. Apelqvist, A. *et al.* Notch signalling controls pancreatic cell differentiation. *Nature* **400**, 877-81 (1999).

186. Fitch, D.D. Oxygen consumption in the prosobranch snail Viviparus contectoides (Mollusca: Gastropoda). I. Effects of weight and activity. *Comp Biochem Physiol A Comp Physiol* **51**, 815-20 (1975).
187. Allison, D.B., Paultre, F., Maggio, C., Mezzitis, N. & Pi-Sunyer, F.X. The use of areas under curves in diabetes research. *Diabetes Care* **18**, 245-50 (1995).
188. Andrikopoulos, S., Blair, A.R., Deluca, N., Fam, B.C. & Proietto, J. Evaluating the glucose tolerance test in mice. *Am J Physiol Endocrinol Metab* **295**, E1323-32 (2008).
189. Fowler, S.C., Zarcone, T.J., Chen, R., Taylor, M.D. & Wright, D.E. Low grip strength, impaired tongue force and hyperactivity induced by overexpression of neurotrophin-3 in mouse skeletal muscle. *Int J Dev Neurosci* **20**, 303-8 (2002).
190. Chugh, K., Goyal, S., Shankar, V. & Chugh, S.N. Thyroid function tests in metabolic syndrome. *Indian J Endocrinol Metab* **16**, 958-61 (2012).
191. Fisher, D.A. Physiological variations in thyroid hormones: physiological and pathophysiological considerations. *Clin Chem* **42**, 135-9 (1996).
192. Zhang, X.Y., Zhang, Q. & Wang, D.H. Litter size variation in hypothalamic gene expression determines adult metabolic phenotype in Brandt's voles (Lasiopodomys brandtii). *PLoS One* **6**, e19913 (2011).
193. Johannsen, D.L. *et al.* Effect of short-term thyroxine administration on energy metabolism and mitochondrial efficiency in humans. *PLoS One* **7**, e40837 (2012).
194. Dauphinee, S.M. *et al.* Characterization of two ENU-induced mutations affecting mouse skeletal morphology. *G3 (Bethesda)* **3**, 1753-8 (2013).
195. Caruana, G. *et al.* Genome-wide ENU mutagenesis in combination with high density SNP analysis and exome sequencing provides rapid identification of novel mouse models of developmental disease. *PLoS One* **8**, e55429 (2013).
196. Wang, Y., Zheng, Y., Nishina, P.M. & Naggert, J.K. A new mouse model of metabolic syndrome and associated complications. *J Endocrinol* **202**, 17-28 (2009).
197. Sabrautzki, S. *et al.* New mouse models for metabolic bone diseases generated by genome-wide ENU mutagenesis. *Mamm Genome* **23**, 416-30 (2012).
198. Hay, R.T. SUMO: a history of modification. *Mol Cell* **18**, 1-12 (2005).
199. Fossmark, R. *et al.* Decreased bone mineral density and reduced bone quality in H(+) /K(+) ATPase beta-subunit deficient mice. *J Cell Biochem* **113**, 141-7 (2012).
200. Hoozemans, M.J., Koppes, L.L., Twisk, J.W. & van Dieen, J.H. Lumbar bone mass predicts low back pain in males. *Spine (Phila Pa 1976)* **37**, 1579-85 (2012).
201. Deng, H.W., Xu, F.H., Davies, K.M., Heaney, R. & Recker, R.R. Differences in bone mineral density, bone mineral content, and bone areal size in fracturing and non-fracturing women, and their interrelationships at the spine and hip. *J Bone Miner Metab* **20**, 358-66 (2002).
202. Tang, C.H. *et al.* Attenuation of bone mass and increase of osteoclast formation in decoy receptor 3 transgenic mice. *J Biol Chem* **282**, 2346-54 (2007).
203. Warren, M.P. *et al.* Lack of bone accretion and amenorrhea: evidence for a relative osteopenia in weight-bearing bones. *J Clin Endocrinol Metab* **72**, 847-53 (1991).
204. Dixon, W.G. *et al.* Low grip strength is associated with bone mineral density and vertebral fracture in women. *Rheumatology (Oxford)* **44**, 642-6 (2005).
205. Windahl, S.H. *et al.* Reduced bone mass and muscle strength in male 5alpha-reductase type 1 inactivated mice. *PLoS One* **6**, e21402 (2011).
206. Golub, E.E., Boesze-Battaglia, K. The role of alkaline phosphatase in mineralization. *Curr Opin Orthop* **18**, 444-448 (2007).
207. Azinge, E.C. & Bolarin, D.M. Osteocalcin and bone-specific alkaline phosphatase in sickle cell haemoglobinopathies. *Niger J Physiol Sci* **21**, 21-5 (2006).
208. Menahan, L.A., Sobocinski, K.A. & Austin, B.P. The origin of plasma alkaline phosphatase activity in mice and rats. *Comp Biochem Physiol B* **79**, 279-83 (1984).

209. Noma, K. *et al.* Roles of rho-associated kinase and oxidative stress in the pathogenesis of aortic stiffness. *J Am Coll Cardiol* **49**, 698-705 (2007).
210. Shioi, A. *et al.* Induction of bone-type alkaline phosphatase in human vascular smooth muscle cells: roles of tumor necrosis factor-alpha and oncostatin M derived from macrophages. *Circ Res* **91**, 9-16 (2002).
211. Sabrautzki, S. *et al.* An ENU mutagenesis-derived mouse model with a dominant Jak1 mutation resembling phenotypes of systemic autoimmune disease. *Am J Pathol* **183**, 352-68 (2013).
212. Szymczak, J., Bohdanowicz-Pawlak, A., Waszczuk, E. & Jakubowska, J. Low bone mineral density in adult patients with coeliac disease. *Endokrynol Pol* **63**, 270-6 (2012).
213. Turan, S. *et al.* Serum alkaline phosphatase levels in healthy children and evaluation of alkaline phosphatase z-scores in different types of rickets. *J Clin Res Pediatr Endocrinol* **3**, 7-11 (2011).
214. Peng, Z., Li, X., Makela, S., Vaananen, H.K. & Poutanen, M. Skeletal changes in transgenic male mice expressing human cytochrome p450 aromatase. *J Bone Miner Res* **19**, 1320-8 (2004).
215. Pashuck, T.D. *et al.* Murine model for cystic fibrosis bone disease demonstrates osteopenia and sex-related differences in bone formation. *Pediatr Res* **65**, 311-6 (2009).
216. Turner, R.T., Riggs, B.L. & Spelsberg, T.C. Skeletal effects of estrogen. *Endocr Rev* **15**, 275-300 (1994).
217. Felson, D.T. *et al.* The effect of postmenopausal estrogen therapy on bone density in elderly women. *N Engl J Med* **329**, 1141-6 (1993).
218. Fish, J.L. *et al.* Satb2, modularity, and the evolvability of the vertebrate jaw. *Evol Dev* **13**, 549-64 (2011).
219. Bonilla-Claudio, M. *et al.* Bmp signaling regulates a dose-dependent transcriptional program to control facial skeletal development. *Development* **139**, 709-19 (2012).
220. Van Buggenhout, G. *et al.* The del(2)(q32.2q33) deletion syndrome defined by clinical and molecular characterization of four patients. *Eur J Med Genet* **48**, 276-89 (2005).
221. Rainger, J.K. *et al.* Disruption of SATB2 or its long-range cis-regulation by SOX9 causes a syndromic form of Pierre Robin sequence. *Hum Mol Genet* **23**, 2569-79 (2014).
222. Docker, D. *et al.* Further delineation of the SATB2 phenotype. *Eur J Hum Genet* (2013).
223. Vieira, A.R. *et al.* Medical sequencing of candidate genes for nonsyndromic cleft lip and palate. *PLoS Genet* **1**, e64 (2005).
224. Dai, X.M., Zong, X.H., Akhter, M.P. & Stanley, E.R. Osteoclast deficiency results in disorganized matrix, reduced mineralization, and abnormal osteoblast behavior in developing bone. *J Bone Miner Res* **19**, 1441-51 (2004).
225. Wu, X.B. *et al.* Impaired osteoblastic differentiation, reduced bone formation, and severe osteoporosis in noggin-overexpressing mice. *J Clin Invest* **112**, 924-34 (2003).
226. Eleftheriadis, T. *et al.* Plasma serotonin and markers of bone formation and bone resorption in hemodialysis patients. *Iran J Kidney Dis* **7**, 36-41 (2013).
227. Kanazawa, I., Yamaguchi, T., Yamauchi, M. & Sugimoto, T. Rosuvastatin increased serum osteocalcin levels independent of its serum cholesterol-lowering effect in patients with type 2 diabetes and hypercholesterolemia. *Intern Med* **48**, 1869-73 (2009).
228. Enomoto, H. *et al.* Induction of osteoclast differentiation by Runx2 through receptor activator of nuclear factor-kappa B ligand (RANKL) and osteoprotegerin regulation and partial rescue of osteoclastogenesis in Runx2-/- mice by RANKL transgene. *J Biol Chem* **278**, 23971-7 (2003).
229. Zhou, X. *et al.* Multiple functions of Osterix are required for bone growth and homeostasis in postnatal mice. *Proc Natl Acad Sci U S A* **107**, 12919-24 (2010).
230. Cao, H. *et al.* Activating transcription factor 4 regulates osteoclast differentiation in mice. *J Clin Invest* **120**, 2755-66 (2010).

231. Martin, T.J. & Sims, N.A. Osteoclast-derived activity in the coupling of bone formation to resorption. *Trends Mol Med* **11**, 76-81 (2005).

232. Lee, S.H. *et al.* v-ATPase V0 subunit d2-deficient mice exhibit impaired osteoclast fusion and increased bone formation. *Nat Med* **12**, 1403-9 (2006).

233. Katsumata, S., Katsumata-Tsuboi, R., Uehara, M. & Suzuki, K. Severe iron deficiency decreases both bone formation and bone resorption in rats. *J Nutr* **139**, 238-43 (2009).

234. Wright, I. *et al.* Bone remodelling is reduced by recovery from iron-deficiency anaemia in premenopausal women. *J Physiol Biochem* **69**, 889-96 (2013).

235. Toxqui, L. *et al.* Low iron status as a factor of increased bone resorption and effects of an iron and vitamin D-fortified skimmed milk on bone remodelling in young Spanish women. *Eur J Nutr* **53**, 441-8 (2014).

236. Katsumata, S., Tsuboi, R., Uehara, M. & Suzuki, K. Dietary iron deficiency decreases serum osteocalcin concentration and bone mineral density in rats. *Biosci Biotechnol Biochem* **70**, 2547-50 (2006).

237. D'Amelio, P. *et al.* Role of iron metabolism and oxidative damage in postmenopausal bone loss. *Bone* **43**, 1010-5 (2008).

238. Kim, B.J., Lee, S.H., Koh, J.M. & Kim, G.S. The association between higher serum ferritin level and lower bone mineral density is prominent in women >/=45 years of age (KNHANES 2008-2010). *Osteoporos Int* **24**, 2627-37 (2013).

239. Ishii, K.A. *et al.* Coordination of PGC-1beta and iron uptake in mitochondrial biogenesis and osteoclast activation. *Nat Med* **15**, 259-66 (2009).

240. Jian, J., Pelle, E. & Huang, X. Iron and menopause: does increased iron affect the health of postmenopausal women? *Antioxid Redox Signal* **11**, 2939-43 (2009).

241. Moinichen, C.B., Lyngstadaas, S.P. & Risnes, S. Morphological characteristics of mouse incisor enamel. *J Anat* **189 (Pt 2)**, 325-33 (1996).

242. Chen, H.C. *et al.* MicroRNA and messenger RNA analyses of mesenchymal stem cells derived from teeth and the Wharton jelly of umbilical cord. *Stem Cells Dev* **21**, 911-22 (2012).

243. Huang, B. *et al.* Distribution of SIBLING proteins in the organic and inorganic phases of rat dentin and bone. *Eur J Oral Sci* **116**, 104-12 (2008).

244. Souza, M.A., Soares Junior, L.A., Santos, M.A. & Vaisbich, M.H. Dental abnormalities and oral health in patients with Hypophosphatemic rickets. *Clinics (Sao Paulo)* **65**, 1023-6 (2010).

245. Scaramuzzo, L. *et al.* Orthopaedic and dental abnormalities in osteogenesis imperfecta: a review of the literature. *J Biol Regul Homeost Agents* **25**, 313-21 (2011).

246. Majorana, A. *et al.* Dentinogenesis imperfecta in children with osteogenesis imperfecta: a clinical and ultrastructural study. *Int J Paediatr Dent* **20**, 112-8 (2010).

247. Opsahl Vital, S. *et al.* Tooth dentin defects reflect genetic disorders affecting bone mineralization. *Bone* **50**, 989-97 (2012).

248. Lopez Franco, G.E., Huang, A., Pleshko Camacho, N. & Blank, R.D. Dental phenotype of the col1a2(oim) mutation: DI is present in both homozygotes and heterozygotes. *Bone* **36**, 1039-46 (2005).

249. Ye, L., Zhang, S., Ke, H., Bonewald, L.F. & Feng, J.Q. Periodontal breakdown in the Dmp1 null mouse model of hypophosphatemic rickets. *J Dent Res* **87**, 624-9 (2008).

250. Arai, K., Soga, T., Ohata, H., Otagiri, A. & Shibasaki, T. Effects of food restriction on peroxisome proliferator-activated receptor-gamma and glucocorticoid receptor signaling in adipose tissues of normal rats. *Metabolism* **53**, 28-36 (2004).

251. Miyazaki, S. *et al.* Effect of exercise training on adipocyte-size-dependent expression of leptin and adiponectin. *Life Sci* **86**, 691-8 (2010).

252. Miller, W.H., Jr. & Faust, I.M. Alterations in rat adipose tissue morphology induced by a low-temperature environment. *Am J Physiol* **242**, E93-6 (1982).

253. Seale, P. *et al.* PRDM16 controls a brown fat/skeletal muscle switch. *Nature* **454**, 961-7 (2008).

254. Ussar, S. *et al.* ASC-1, PAT2, and P2RX5 are cell surface markers for white, beige, and brown adipocytes. *Sci Transl Med* **6**, 247ra103 (2014).
255. Kajimura, S. & Saito, M. A new era in brown adipose tissue biology: molecular control of brown fat development and energy homeostasis. *Annu Rev Physiol* **76**, 225-49 (2014).
256. Puigserver, P. *et al.* A cold-inducible coactivator of nuclear receptors linked to adaptive thermogenesis. *Cell* **92**, 829-39 (1998).
257. Bostrom, P. *et al.* A PGC1-alpha-dependent myokine that drives brown-fat-like development of white fat and thermogenesis. *Nature* **481**, 463-8 (2012).
258. Dempersmier, J. *et al.* Cold-Inducible Zfp516 Activates UCP1 Transcription to Promote Browning of White Fat and Development of Brown Fat. *Mol Cell* **57**, 235-46 (2015).
259. Okada, Y., Sakaue, H., Nagare, T. & Kasuga, M. Diet-induced up-regulation of gene expression in adipocytes without changes in DNA methylation. *Kobe J Med Sci* **54**, E241-9 (2009).
260. Musri, M.M., Corominola, H., Casamitjana, R., Gomis, R. & Parrizas, M. Histone H3 lysine 4 dimethylation signals the transcriptional competence of the adiponectin promoter in preadipocytes. *J Biol Chem* **281**, 17180-8 (2006).
261. Sakamoto, H. *et al.* Sequential changes in genome-wide DNA methylation status during adipocyte differentiation. *Biochem Biophys Res Commun* **366**, 360-6 (2008).
262. Elias, I. *et al.* Adipose tissue overexpression of vascular endothelial growth factor protects against diet-induced obesity and insulin resistance. *Diabetes* **61**, 1801-13 (2012).
263. Mossenbock, K. *et al.* Browning of white adipose tissue uncouples glucose uptake from insulin signaling. *PLoS One* **9**, e110428 (2014).
264. Muller, G., Ertl, J., Gerl, M. & Preibisch, G. Leptin impairs metabolic actions of insulin in isolated rat adipocytes. *J Biol Chem* **272**, 10585-93 (1997).
265. White, M.F. IRS proteins and the common path to diabetes. *Am J Physiol Endocrinol Metab* **283**, E413-22 (2002).
266. Hennige, A.M. *et al.* Upregulation of insulin receptor substrate-2 in pancreatic beta cells prevents diabetes. *J Clin Invest* **112**, 1521-32 (2003).
267. Awazawa, M. *et al.* Adiponectin enhances insulin sensitivity by increasing hepatic IRS-2 expression via a macrophage-derived IL-6-dependent pathway. *Cell Metab* **13**, 401-12 (2011).
268. Togashi, Y. *et al.* beta-Cell proliferation after a partial pancreatectomy is independent of IRS-2 in mice. *Endocrinology* **155**, 1643-52 (2014).
269. Lau, P., Fitzsimmons, R.L., Pearen, M.A., Watt, M.J. & Muscat, G.E. Homozygous staggerer (sg/sg) mice display improved insulin sensitivity and enhanced glucose uptake in skeletal muscle. *Diabetologia* **54**, 1169-80 (2011).
270. Orava, J. *et al.* Different metabolic responses of human brown adipose tissue to activation by cold and insulin. *Cell Metab* **14**, 272-9 (2011).
271. Seale, P. *et al.* Prdm16 determines the thermogenic program of subcutaneous white adipose tissue in mice. *J Clin Invest* **121**, 96-105 (2011).
272. Garofalo, R.S. *et al.* Severe diabetes, age-dependent loss of adipose tissue, and mild growth deficiency in mice lacking Akt2/PKB beta. *J Clin Invest* **112**, 197-208 (2003).
273. Davis, R.J. Signal transduction by the JNK group of MAP kinases. *Cell* **103**, 239-52 (2000).
274. Tuncman, G. *et al.* Functional in vivo interactions between JNK1 and JNK2 isoforms in obesity and insulin resistance. *Proc Natl Acad Sci U S A* **103**, 10741-6 (2006).
275. Aguirre, V., Uchida, T., Yenush, L., Davis, R. & White, M.F. The c-Jun NH(2)-terminal kinase promotes insulin resistance during association with insulin receptor substrate-1 and phosphorylation of Ser(307). *J Biol Chem* **275**, 9047-54 (2000).
276. Hirosumi, J. *et al.* A central role for JNK in obesity and insulin resistance. *Nature* **420**, 333-6 (2002).
277. Kubota, N. *et al.* Dynamic functional relay between insulin receptor substrate 1 and 2 in hepatic insulin signaling during fasting and feeding. *Cell Metab* **8**, 49-64 (2008).

278. Braun, T.P. *et al.* Regulation of lean mass, bone mass, and exercise tolerance by the central melanocortin system. *PLoS One* **7**, e42183 (2012).
279. Corina Buta, C.V., Didona Ungureanu, Voichita Mogos, Dumitru D. Branisteanu. Lean body mass and leptin, but not fat mass are independent predictors of bone mass in postmenopausal women. *Revista Romana de Medicina de Laborator* **20**, 9 (2012).
280. Pannemans, D.L. & Westerterp, K.R. Energy expenditure, physical activity and basal metabolic rate of elderly subjects. *Br J Nutr* **73**, 571-81 (1995).
281. White, C.R. & Seymour, R.S. Mammalian basal metabolic rate is proportional to body mass2/3. *Proc Natl Acad Sci U S A* **100**, 4046-9 (2003).
282. Speakman, J.R. Measuring energy metabolism in the mouse - theoretical, practical, and analytical considerations. *Front Physiol* **4**, 34 (2013).
283. Jiao, Y. *et al.* Mex3c mutation reduces adiposity and increases energy expenditure. *Mol Cell Biol* **32**, 4350-62 (2012).
284. Turley, K.R., Bland, J.R. & Evans, W.J. Effects of different doses of caffeine on exercise responses in young children. *Med Sci Sports Exerc* **40**, 871-8 (2008).
285. Devalaraja-Narashimha, K. & Padanilam, B.J. PARP1 deficiency exacerbates diet-induced obesity in mice. *J Endocrinol* **205**, 243-52 (2010).
286. Zengin, A. *et al.* Neuropeptide Y mediates the short-term hypometabolic effect of estrogen deficiency in mice. *Int J Obes (Lond)* **37**, 390-8 (2013).
287. Arch, J.R., Hislop, D., Wang, S.J. & Speakman, J.R. Some mathematical and technical issues in the measurement and interpretation of open-circuit indirect calorimetry in small animals. *Int J Obes (Lond)* **30**, 1322-31 (2006).
288. Even, P.C. & Nadkarni, N.A. Indirect calorimetry in laboratory mice and rats: principles, practical considerations, interpretation and perspectives. *Am J Physiol Regul Integr Comp Physiol* **303**, R459-76 (2012).
289. Liu, S. *et al.* SRA Gene Knockout Protects against Diet-induced Obesity and Improves Glucose Tolerance. *J Biol Chem* **289**, 13000-9 (2014).
290. Muller, T.D. *et al.* p62 links beta-adrenergic input to mitochondrial function and thermogenesis. *J Clin Invest* **123**, 469-78 (2013).
291. McMurray, F. *et al.* Adult onset global loss of the fto gene alters body composition and metabolism in the mouse. *PLoS Genet* **9**, e1003166 (2013).
292. Tschop, M.H. *et al.* A guide to analysis of mouse energy metabolism. *Nat Methods* **9**, 57-63 (2012).
293. Kato, H. *et al.* Mechanism of amelioration of insulin resistance by beta3-adrenoceptor agonist AJ-9677 in the KK-Ay/Ta diabetic obese mouse model. *Diabetes* **50**, 113-22 (2001).
294. Feldmann, H.M., Golozoubova, V., Cannon, B. & Nedergaard, J. UCP1 ablation induces obesity and abolishes diet-induced thermogenesis in mice exempt from thermal stress by living at thermoneutrality. *Cell Metab* **9**, 203-9 (2009).
295. Evans, B.A., Agar, L. & Summers, R.J. The role of the sympathetic nervous system in the regulation of leptin synthesis in C57BL/6 mice. *FEBS Lett* **444**, 149-54 (1999).
296. Dulloo, A.G. Translational issues in targeting brown adipose tissue thermogenesis for human obesity management. *Ann N Y Acad Sci* **1302**, 1-10 (2013).
297. Hrabe de Angelis, M., McIntyre, J., 2nd & Gossler, A. Maintenance of somite borders in mice requires the Delta homologue Dll1. *Nature* **386**, 717-21 (1997).
298. Przemeck, G.K., Heinzmann, U., Beckers, J. & Hrabe de Angelis, M. Node and midline defects are associated with left-right development in Delta1 mutant embryos. *Development* **130**, 3-13 (2003).
299. Grandbarbe, L. *et al.* Delta-Notch signaling controls the generation of neurons/glia from neural stem cells in a stepwise process. *Development* **130**, 1391-402 (2003).
300. Marklund, U. *et al.* Domain-specific control of neurogenesis achieved through patterned regulation of Notch ligand expression. *Development* **137**, 437-45 (2010).

301. Rubio-Aliaga, I. *et al.* A genetic screen for modifiers of the delta1-dependent notch signaling function in the mouse. *Genetics* **175**, 1451-63 (2007).
302. Nobta, M. *et al.* Critical regulation of bone morphogenetic protein-induced osteoblastic differentiation by Delta1/Jagged1-activated Notch1 signaling. *J Biol Chem* **280**, 15842-8 (2005).
303. Bai, S. *et al.* NOTCH1 regulates osteoclastogenesis directly in osteoclast precursors and indirectly via osteoblast lineage cells. *J Biol Chem* **283**, 6509-18 (2008).
304. Engin, F. *et al.* Dimorphic effects of Notch signaling in bone homeostasis. *Nat Med* **14**, 299-305 (2008).
305. Hilton, M.J. *et al.* Notch signaling maintains bone marrow mesenchymal progenitors by suppressing osteoblast differentiation. *Nat Med* **14**, 306-14 (2008).
306. Pfister, S. *et al.* Interaction of the MAGUK family member Acvrinp1 and the cytoplasmic domain of the Notch ligand Delta1. *J Mol Biol* **333**, 229-35 (2003).
307. Wright, G.J., Leslie, J.D., Ariza-McNaughton, L. & Lewis, J. Delta proteins and MAGI proteins: an interaction of Notch ligands with intracellular scaffolding molecules and its significance for zebrafish development. *Development* **131**, 5659-69 (2004).
308. Mizuhara, E. *et al.* MAGI1 recruits Dll1 to cadherin-based adherens junctions and stabilizes it on the cell surface. *J Biol Chem* **280**, 26499-507 (2005).
309. Estrach, S., Legg, J. & Watt, F.M. Syntenin mediates Delta1-induced cohesiveness of epidermal stem cells in culture. *J Cell Sci* **120**, 2944-52 (2007).
310. Fanning, A.S. & Anderson, J.M. PDZ domains: fundamental building blocks in the organization of protein complexes at the plasma membrane. *J Clin Invest* **103**, 767-72 (1999).

IV. Acknowledgements

I would like to express my special appreciation to Prof. Dr. Martin Hrabé de Angelis, whose support and supervision made my doctoral thesis work possible. His active interested in my progress has always resulted in great advice.

I am likewise extremely indebted to Dr. Sibylle Sabrautzki and Dr. Gerhard Przemeck; not only for their valuable advice, constructive criticism and weekly discussion, but also academically, with their patience along the rough road through to the completion of this thesis. Thanks also to Dr. Michael Rosemann for providing advice on my project.

My thanks go to Silvia Crowley, Sandra Hoffmann, Andreas Mayer and Gerlinde Bergter for the exceptional teamwork; and to Dr. David Cavanna, Daniel Gradinger, Nina Schieven and Michael Schulz for supporting me with the lab work. Special thanks go to Dr. Peter Huypens, Dr. Christian Cohrs, Dr. Julia Calzada-Wack, Dr. Wolfgang Hans and Dr. Feng Zhao; I will always have fond memories of working and discussion with you.

Dozens of people have helped me immensely with my thesis work. I would like to give a heartfelt thanks to Dr. Marion Horsch, Dr. Helmut Fuchs, Dr. Jan Rozman, Dr. Susanne Neschen, Dr. Cornelia Prehn, Dr. Lore Becker, Dr. Birgit Rathkolb and the friendly members of their group who provided me with excellent support and insight into their special laboratory techniques. I thank Steffen Sass for his help in bioinformatics analysis.

I would like to acknowledge Dr. Rui-Wang Sattler for her great help in areas of my life. Many thanks also go to Dr. Peter Huypens and Robert Jacobs for proof-reading my text.

I am particularly grateful to my wife, Xiaomin, for her considerable support, encouragement and sacrifice. And finally, I am indebted to my parents, grandparents and other family members for their tremendous support throughout my journey to this point, which has motivated me to excel.

V. Affirmation

Ich erkläre hiermit an Eides statt, dass ich vorliegende Arbeit selbstständig, ohne unzulässige fremde Hilfe und ausschließlich mit den angegebenen Quellen und Hilfsmitteln angefertigt habe.

Die verwendeten Literaturquellen sind im Literaturverzeichnis (References) vollständig zitiert.

Diese Arbeit hat in dieser oder ähnlicher Form noch keiner anderen Prüfungsbehörde vorgelegen.

München, den 16.03.2015 Shen Chi